ACTIVE REFLECTION ABSORPTION FOR A THREE DIMENSIONAL MULTIDIRECTIONAL WAVE GENERATOR

A Dissertation

by

OSCAR CRUZ CASTRO

Submitted to the Office of Graduate Studies of
Texas A&M University
in partial fulfillment of the requirements for the degree of

DOCTOR OF PHILOSOPHY

August 2009

Major Subject: Ocean Engineering

ACTIVE REFLECTION ABSORPTION FOR A THREE DIMENSIONAL MULTIDIRECTIONAL WAVE GENERATOR

A Dissertation

by

OSCAR CRUZ CASTRO

Submitted to the Office of Graduate Studies of
Texas A&M University
in partial fulfillment of the requirements for the degree of

DOCTOR OF PHILOSOPHY

Approved by:

Chair of Committee,	Billy L. Edge
Committee Members,	Patrick J. Lynett
	Jose Silva-Martinez
	Robert E. Randall
Head of Department,	David V. Rosowsky

August 2009

Major Subject: Ocean Engineering

ABSTRACT

Active Reflection Absorption for a Three Dimensional

Multidirectional Wave Generator. (August 2009)

Oscar Cruz Castro, B.S., Instituto Politécnico Nacional, México;

M.S., Texas A&M University

Chair of Advisory Committee: Dr. Billy L. Edge

In order to implement an accurate system that allows for absorption of reflected waves impinging to a wave maker (Active Reflection Absorption), it was required to apply a method to estimate properly the direction of arrival of the waves that does it in the fastest way possible. Our wavemaker control system has been prepared to handle an algorithm provided by Bosch-Rexroth where the wave angle estimation is practically locked to a very narrow frequency band (spatial gain-mixer). The system was evaluated with physical tests in a 3D wave basin for different conditions of reflected waves arriving with an angle to the wavemaker front, and acceptable performance has been found for the 3D ARA mode. However, for certain conditions over-compensation or sub-compensation can develop resulting in a poor absorption. This is mainly related to not being able to determine accurately the direction from which the reflected waves travel towards the wavemaker.

The present work employed concepts found in the areas of antenna array signal processing and signal propagation, which were applied to this problem. This approach

coupled naturally with our wavemaker system since it was prepared with 48 gages that can be employed in an array antenna fashion. A program was codified from an algorithm found in literature to calculate the Direction of Arrival (DOA) of the reflected waves. The focus for the testing of this program was with regular waves.

The tests were conducted to validate the program with different angles of incidence and show that for regular waves the program was able to detect accurately the DOA of these in as few as 5 snapshots, with a minimum of 7 gages used as the antenna input. With data obtained directly from the control system of our wavemaker using regular waves, the program was able to determine the DOA. The computational burden of the algorithm is not significant in the case of regular waves. A modification of the program is required to analyze the DOA of reflected irregular waves, which could increase the computational burden. Actual implementation of this program to our control system depends on cooperation with Bosch-Rexroth.

DEDICATION

I am most of all grateful to God for allowing me to reach the culmination of several years of study and work. I have put all my endeavors in His hands and this was no exception.

This dissertation is the product of the love, patience and understanding of my family, and their faith in me. I would like to equally dedicate this work to my wife Carmen, my little boy Oscar, my parents Jesus and Ofelia, and my brother Edgar, who have always stood on my side providing the values and motivation to accomplish my goals. Thanks for loving me so much.

ACKNOWLEDGEMENTS

I would like to express my gratitude to my committee chair, Dr. Billy L. Edge, because he has been an example of leadership and hard work. Without his support, valuable insights in how to approach this research, guidance at the time of selecting this topic, and moreover his friendship, this research would have never been possible. I also want to thank my committee members, Dr. Robert E. Randall, Dr. Patrick J. Lynett, and Dr. Jose Silva-Martinez, for their guidance, time, and support throughout the course of this research.

Special acknowledgements are in order for two institutions in my home country (México). First the Consejo Nacional de Ciencia y Tecnología (CONACYT); which granted me a scholarship that allowed me to complete my studies at Texas A&M. The other institution is the Instituto Politécnico Nacional (IPN), where I am currently a professor, for allowing me to come to study at Texas A&M. Their support is indeed appreciated. My deepest gratitude is also extended to my country México and its people.

Thanks also go to my dear friends John Reed (Laboratory Technician), Po Hung Yeh (Ph.D.), and Hyun Young Park (Ph.D.), for sharing their knowledge and experience with me, making my time at the Ocean Engineering Program and the Haynes Coastal Engineering Laboratory one of the most wonderful experiences while at Texas A&M University.

Finally, thanks to my whole family for their encouragement, support, patience and love.

TABLE OF CONTENTS

CHAPTER Page

CHAPTER Page

LIST OF FIGURES

FIGURE Page

FIGURE Page

FIGURE Page

LIST OF TABLES

TABLE Page

.

CHAPTER I

INTRODUCTION

1.1 Background

The topic presented in this dissertation was conceived from working as Ph.D. student in several projects at the Haynes Costal Engineering Laboratory at Texas A&M University (TAMU). The motivation of studying the Active Reflection Absorption (ARA) system of our Three Dimensional Multidirectional Wave Generator came in late 2005. Originally, the topic was recommended by Dr. Billy L. Edge, Director of the Haynes Coastal Engineering Laboratory. At that time we realized that performance of the ARA for our wavemaker was not as expected. Experiments designed to measure the reflection coefficient of the wavemaker during generation of waves, indicated that ARA followed theory but it was limited to work effectively to a narrow frequency band.

Then, after the laboratory engaged in their first projects for the private industry, it became evident that the original ARA system, implemented by Bosch-Rexroth in early 2005, needed a tune up and ultimately it needed to be modified in order to improve it. As mentioned above its performance was limited and was not usable for certain conditions (especially at high frequencies 2 Hz and higher). To understand better the importance of ARA for a wavemaker let us explain their relationship in the next section.

This dissertation follows the style of Coastal Engineering.

1.1.1 Active Reflection Absorption for Wavemakers

Wavemakers have become standard equipment for coastal engineering laboratories, and towing tanks around the world. The main purpose of this kind of equipment is to simulate as close as possible real-sea state conditions under a controlled environment. Through its use and the application of physical modeling it is possible to help coastal engineering researchers and designers to determine the economic, safety and reliability aspects, for different coastal structures as breakwaters, jetties, ports, ship channels, and sediment transport along the coast, among many applications. The technology involved in wavemaker development has changed dramatically in the last ten to fifteen years. These changes have allowed for this equipment to be used in a constant basis with control systems for simultaneous generation and absorption of waves, both on flume wavemakers and on multidirectional wavemakers.

These kinds of wavemakers are classified as absorbing wavemakers or Active Reflection Absorption (ARA) systems, because they act as a moving boundary controlled to absorb waves (Schaffer, 2001). This is especially important in hydraulic testing as there are waves reflected from physical models and structures inside a basin, as well as from the basin's boundaries. As a consequence, waves gradually reflected back to the wave generator increase disturbances and reduce the accuracy of experiments and its duration.

Use of an ARA system becomes evident when the paddles of a wavemaker are placed in a line in a relatively wide basin for multidirectional wave tests (such as the

TAMU wave generator), because this situation presents the following issues: an experiment area with a uniform wave field (including oblique waves) is limited, and reflected waves from a model and/or a wave basin cannot be absorbed properly (Ito et al., 1996). In general most of the ARA systems are based on linear wavemaker theory and linear control, which allow us, by using the superposition principle, to treat ARA independently from wave generation (Schaffer and Klopman, 2000).

Therefore, ARA systems can be used to generate waves, and at the same time avoid their re-reflection. Such systems can be used also as pure wave absorbers instead of passive absorbers (Schaffer and Klopman, 2000). Some of the advantages of using an active reflection absorption system are described by Schaffer and Klopman (2000), and Schaffer (2001). Among them arise:

1. Spurious re-reflection of outgoing waves is largely avoided, especially in situations with large reflections.
2. Suppression of wave flume resonance. Typically absorption by the wave generator is much better at low frequencies than that of passive absorbers.
3. Resonant oscillations in the facility can be prevented, which allows to extend the maximum test duration.
4. The flume or basin stilling time between tests is substantially reduced by quickly removing the slowly damped low-frequency oscillations.

The next section presents a brief summary of ARA development as well as its classification, and mentions the most representative works on this field.

1.1.2 Summary of ARA Development

Basically, the theory related to wave absorption using a wavemaker can be classified according to literature in three categories: 2D ARA, Quasi-3D ARA and Fully-3D ARA (Schaffer and Klopman, 2000). Significant success in the implementation of wave absorption is mostly reported and tested using flume wavemakers (2D-waves, 2D ARA), e.g. Milgram (1970), Salter (1981), Christensen and Frigaard (1994), and Schaffer et al. (1994), where the practical experiment results show good agreement with theory. 2D ARA was developed initially to try to absorb waves at the end of a flume using the superposition principle and by solving the linear operation of two physical quantities that have a linear relation; this is paddle position and water surface elevation signals (Milgram, 1970).

3D ARA for multidirectional wavemakers is still under development. It has been divided according to the type of control system and feedback used in, Quasi-3D ARA and Fully-3D ARA. Quasi-3D ARA can be described in general as a set of independent wave paddles (flume wave makers) working together in parallel, using 2D ARA (1D filters) to create a multidirectional wavemaker with wave absorption capability. Therefore, no information on directionality of reflected waves is available for the system, since it only takes into account a representative frequency and a priori angle of incidence of reflected waves (usually zero degrees), instead of recognizing that waves have dominant frequency and directional dispersion (Ito et al., 1996).

The situation mentioned above greatly reduces wavemaker absorptivity. Information about Quasi-3D ARA is limited and only qualitative data is provided, e.g. Salter (1984), Hirakuchi et al. (1992). Nevertheless important progress in considerable damping of the reflected waves is achieved compared to not using anything at all in a multidirectional wavemaker. Also the use of electronic analog filters, for the ARA loop, support these approaches.

On the other hand, Fully-3D ARA systems should be able to discriminate the wave angle at which the reflected wave approaches the wavemaker. For this purpose the coupling of feedback signals is required (multiple input single output) to acquire directional sensitivity. There is no homogeneity in the ideas presented in literature to accomplish this, although the concepts involved have been clarified in recent years. The Fully-3D ARA classification has limited physical experiments, and in consequence almost no results have been reported, or they have been reported with limited data, e.g. Klopman et al. (1996, 2001), or qualitatively, e.g. Ito et al. (1996). Results for this classification have been reported mostly for numerical simulations, e.g. Schaffer and Skourup (1996), Schaffer and Klopman (2000), Schaffer et al. (2000) and Schaffer (2001), where also qualitative results in physical arrangements are reported. For these latest approximations of Fully-3D ARA, the use of digital filters has been an improvement over previous analog filters, allowing better flexibility in the tune up of these systems. Consequently, a generalized method is needed that can improve the active reflection absorption system (ARA), for any 3D multidirectional wavemaker in a practical and functional way. The next section describes the problem at hand.

1.2 Problem Description

Development of ARA for multidirectional wavemakers (3D-waves) in two dimensions is achieved by extension of the theory applied to flume wavemakers. However, this is not the case for the absorption of three dimensional waves with a multidirectional wavemaker. There have been efforts to extend the principles of wave absorption theory from two dimensions to three dimensions, and they have succeeded theoretically.

On the other hand these principles for wave absorption only take into account one orthogonal wave direction (2D ARA, 0 degree angle) which greatly reduces the wave maker's absorptivity for 3D waves (Quasi-3D ARA), especially with oblique incident angle of the reflected waves. Here the problem is that the system overreacts for oblique waves, creating spurious waves, this is due to the fact that oblique waves require a smaller paddle stroke to be generated, and of course to be absorbed. Although several attempts have been made to implement the theory to a real system, this is still under development due to problems related to control stability, time delay in the signal communication, and mainly because the lack of ability to determine the angle at which the reflected waves impinge towards the wavemaker, which greatly decreases ARA performance as mentioned above.

This is the case of the ARA system, for the three dimensional multidirectional wave generator located at the Haynes Coastal Engineering Laboratory at Texas A&M University. This wavemaker (48 paddles) has been prepared for absorption of waves by

using a hydrodynamic feedback provided by water surface elevation gauges integrated in the paddle front. The feedback signals gathered from up to three paddles are coupled into an ARA loop (based on linear full spectrum wave theory, long wave filters and short wave filters) to provide some directional sensitivity (spatial gain mixer), and therefore calculate a corrected displacement to compensate, by virtue of the superposition principle, reflected waves traveling to the paddle (this is done in a matter of milliseconds, to avoid phase shift in the correction signal). The system, besides depending on the ARA algorithm also relies on proper frequency response control through tuned filtering of the system response.

Here the problems mentioned above, related to control stability and time delay, were handled properly by the manufacturer (Bosch-Rexroth, 2004) by tuning up the 1D filters, available in the control ARA loop software of the wavemaker. Therefore they do not have major contribution for the 3D ARA mode. For the 2D ARA mode, instability problems appear which avoid its use during physical testing. On the other hand, limited performance is achieved only in a narrow frequency band for 3D ARA mode (0.8-0.85 Hz) where the spatial gain mixer is able to perform accurately. More precisely, at lower frequencies the angle is underestimated, creating a small motion compensation of the paddle that creates a poor absorption performance. Similarly, for higher frequencies the angle is overestimated, and motion compensation of the paddle is excessive, evolving in a reduced absorption performance again. Despite the problems mentioned above this arrangement can be regard as a preliminary approximation for a Fully-3D ARA working system in a real basin.

However we have focused our attention to one of the most elusive problems in wave absorption theory mentioned above, that when solved, will improve any approximation of a 3D ARA system. **The problem is to elucidate how to calculate the direction of arrival (DOA) of reflected waves impinging to the wave maker's front in real time**. Being able to calculate this angle allows us to apply the proper compensation to the paddle displacement, avoiding overreaction or under reaction of the system, and in consequence considerable improvement of any 3D ARA system can be achieved, with a simple implementation.

1.3 Objective, Hypothesis and Scope

In order to advance the understanding of 3D ARA systems and improve its application for physical modeling, this research sought to provide a method that focused on the DOA of the reflected waves impinging to a multidirectional wavemaker, which allows the improvement of any Fully-3D ARA system in a real basin.

In consequence, the main objective of this research is **to provide and adapt a method to estimate the direction of arrival of the reflected waves arriving to the wave maker's front in real time.** Therefore one hypothesis of this research is that **by being able to calculate the angle of arrival of the reflected waves in real time the 3D ARA system at hand can be improved.** The rationale is that theory says that the displacement correction calculated at the paddle front only needs to be reduced by a factor of $\cos\theta$, where θ is the DOA of the reflected wave in real time. Here errors in the

estimation of the angle θ can be expected. However, if the angle θ calculated including its error comes closer to the real angle than that achieved with the spatial gain mixer then we can expect a better compensation, and in consequence improvement of any 3D ARA system.

With the main objective stated, two particular objectives emerge. The first one is to evaluate stability of the ARA system at hand, as originally provided by Bosch-Rexroth. The purpose here is allowing an overall evaluation of the ARA system. The second one is to indicate how to implement an algorithm that has been found to work adequately to calculate the DOA of the reflected waves, to our ARA loop.

Summarizing, the main objective, and particular objectives of this research will be accomplished with the following goals in mind:

1. Measurement and evaluation of the control ARA loop conditions as well as analysis of the response of the system available as implemented by Bosch-Rexroth.
2. Improvement of the 1D-filters in the control ARA loop to improve stability of the system for 3D ARA mode.
3. Measurement of the coefficient of absorption of the system (ARA loop) with physical tests, for orthogonal and oblique regular waves impinging to the wave maker, to allow comparison of the results with theory.
4. Codification of the algorithm to calculate DOA of the reflected waves using Matlab™, and analysis of its performance with data recorded in the wave

basin, using a linear array of wave gages to measure regular and irregular waves.

5. Implementation of program for the DOA algorithm in the ARA loop using Simulink™, and evaluation of its performance with data provided by real measurements from the control ARA loop of the wave maker.
6. Develop tests based on different wave conditions for oblique regular and oblique irregular waves impinging to the wave generator, to allow comparison of the results obtained with the corresponding output of the ARA loop working with the spatial gain mixer and then with the DOA algorithm implemented in Matlab™ and Simulink™.

1.4 Limitations and Delimitations

The work presented here contemplates the following assumptions, limitations and delimitations, during the course of this research. We already have an approximation of a 3D ARA loop (developed by Bosch-Rexroth) which theoretical basis is well established, and it is based on linear full spectrum wave theory (based on superposition of many sinusoidal command signals to produce regular and irregular waves for both oblique and orthogonal waves), long wave filters and short wave filters (for tune up of the ARA system).

The ARA system at hand is able to switch from 2D ARA mode to 3D ARA mode, through the software provided. However we are bounded to the setup of this ARA so no changes can be introduced to the ARA loop, other than tune up of the filters and the distribution of the signals coming from center, right and left paddles (a percentage of the correction signal is taken from each paddle, so when they are added a total of a 100% for the center paddle is obtained, this is the spatial gain mixer).

There are more considerations to take into account at the time of implementing a 3D ARA system. For example, evanescent waves, which are created due to the mismatch of the horizontal velocity of the progressive wave, and the shape of the wave board. These evanescent waves are not taken into consideration in our current system. Although they may have considerable influence in the 3D ARA performance, especially at high frequencies, they are not a concern for this research at the frequencies tested, and in general for the working frequencies usually employed in shallow water basins e.g. $kh < 2$ (Ito et al., 1996).

1.5 Dissertation Overview

This dissertation is arranged in five chapters. The content of each chapter is summarized below.

Chapter I introduces the problem with its description and justification, gives a brief summary of the theory available for ARA, and establishes the hypothesis, objectives, goals and scope of this research.

Chapter II presents the Theoretical Background that is used during this research, paying special attention to concepts to evaluate ARA performance, and for estimation of the DOA of the reflected waves. Emphasis is made in the approach found in literature to obtain a 3D ARA system, and how by applying together, a 2D ARA approach and a method to estimate the DOA in real time we can achieve a Fully-3D ARA system.

Chapter III introduces the methods and procedures employed during this research. The methods and procedures are explained in detail and presented in a sequentially order similar to that used during the course of this research.

Chapter IV presents the Analysis of Results, with a discussion and interpretation of these.

Chapter V provides the Summary and Conclusions of this research, the importance of the findings are discussed and topics for future research are suggested.

CHAPTER II

THEORETICAL BRACKGROUND

2.1 Introduction

The concepts involved in the development of any ARA system are based on knowledge related to wavemaker theory (for 2D and 3D wave generation) and its extension to wave absorption. Therefore, this chapter will start with the theoretical development for general purposes of a 3D wavemaker which originally was developed in 2D by Havelock (1929). This is required to explain the basis of the ARA loop at hand, the validity of the superposition principle (for ARA use), and how through this theory the transfer function for any type of wave maker is obtained, focusing in this case to the TAMU wave generator which is a piston type.

The establishment of the theory provided from the literature reviewed to obtain a 3D ARA system is presented here, pointing out how these concepts evolved from a 2D ARA approach. It will be explained how just by focusing on the calculation of the DOA of the reflected waves and combining it with a 2D ARA approach, a Fully-3D ARA system can be achieved. From the theory presented it is possible to establish the parameters to measure the re-reflection coefficient of a wavemaker both theoretically and physically. Here also the algorithm used on the development of the ARA loop provided by Bosch-Rexroth will be presented and how the theory for 3D ARA and 2D ARA was implemented here.

After acquiring an overview of how to develop an ARA system, and how to evaluate it theoretically, it will be presented a method found in the area of antenna array signal processing, specifically a method focused on carrying out space-time processing of data sampled at an array of sensors (in this case the wave gages attached to the front of each paddle of the wavemaker), to calculate the DOA of the reflected wave. Finally it will be discussed how such method can be implemented in a system like the one available at TAMU.

2.2 General Wavemaker Theory

Development of wavemaker theory for generation of waves is well known and it is closely related with dynamic wave absorption theory. Its origins remount to 1929 when Havelock developed his wave maker theory in 2D. From that time up to now, using a similar approach to solve the boundary value problem for wave generation has allowed its application to 3D wavemakers. Many tests with wavemakers using these extensions have been carried, and always reflection coming back to the wavemaker has been a concern. The following is a brief explanation of the boundary value problem that allow us to estimate the wave conditions using the 3D linear fully dispersive wavemaker theory (Madsen, 1974, see also Dean and Dalrymple, 1984, and Dalrymple, 1989) to obtain the transfer function for a piston type wave maker following this theory.

2.2.1 Three Dimensional Wave Maker Theory (Snake Wavemaker)

It has been known for a long time that the best way to generate 3D waves in a 3D-wave basin is by using a segmented wavemaker, where depending on its motion; waves from different directions can be generated. Here refer to Fig. 1, where a definition sketch is shown indicating the wave number vector (***k***), wave length (L), in the direction of propagation of the wave, and their components along x (k_x, L_x) and y (k_y, L_y) coordinates, where the x-y plane represents the still water surface, and the coordinate z runs along the vertical axis. Let us assume an irrotational and incompressible fluid, for which a velocity potential exist ϕ, and therefore must satisfy the continuity equation Eq. (1), or in more general terms, the divergence of the gradient for the velocity potential, also known as the Laplace equation, that may be written as indicated in Eq. (2).

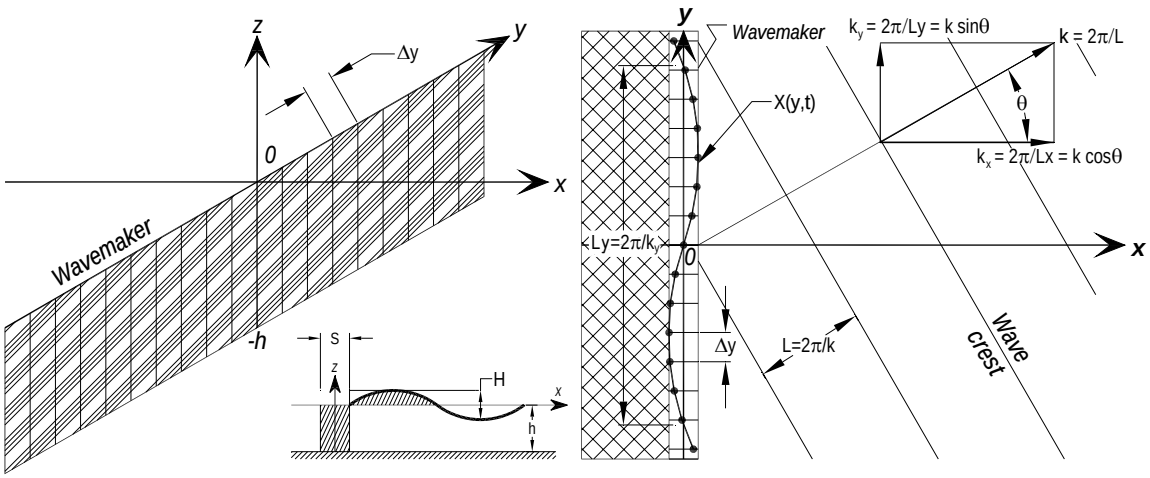

Fig. 1. Definition Sketch. Coordinate System for a 3D-Piston Type Wavemaker, Including its Vertical and Horizontal Cross-Sections

$$\nabla \cdot \mathbf{u} = \frac{\partial \mathrm{u}}{\partial \mathrm{x}} + \frac{\partial \mathrm{v}}{\partial \mathrm{y}} + \frac{\partial \mathrm{w}}{\partial \mathrm{z}} = 0 \tag{1}$$

$$\nabla^2 \phi = \frac{\partial^2 \phi}{\partial \mathrm{x}^2} + \frac{\partial^2 \phi}{\partial \mathrm{y}^2} + \frac{\partial^2 \phi}{\partial \mathrm{z}^2} = 0 \quad \text{in} \quad \begin{cases} 0 < x \leq \infty \\ -\infty < y < \infty \\ -h < z < 0 \end{cases} \tag{2}$$

Here u, v and w are velocity components of the fluid in x, y and z coordinates respectively. For simplicity assume an infinitely long wavemaker along the y-axis, generating waves in the x-y plane. In order to solve Eq. (2) the following linearized B.C's must be satisfied.

$$\left.\begin{aligned} & w = -\frac{\partial \phi}{\partial z} = 0 \quad on\ z = -h, \quad bottom\ B.C\ for\ horizontal\ bottom \\ & \eta = \frac{1}{g}\frac{\partial \phi}{\partial t} \quad on\ z = 0, \quad dynamic\ free\ surface\ B.C \\ & -\frac{\partial \phi}{\partial z} = \frac{\partial \eta}{\partial t} \quad on\ z = 0, \quad kynematic\ free\ surface\ B.C \\ & u(y,z,t) = U(z) \cdot \cos(k_y - \omega t) = -\frac{\partial \phi}{\partial x}\Big|_{x=0} \\ & on\ x = 0, \quad lateral\ wavemaker\ B.C\ due\ to\ motion\ of\ wavemaker \end{aligned}\right\} \tag{3}$$

Here *t, g* and *h* denote time, acceleration of gravity, and water depth, respectively. Using separation of variables to solve the above boundary value problem it can be demonstrated that the following solution Eq. (4) satisfies the bottom B.C, and provides a propagating wave in the *x-y* plane.

$$\left.\begin{aligned} & \phi = A_p \cdot cosh[k(h+z)] \cdot \sin(k_x x + k_y y - \omega t) \\ & + \sum_{n=1}^{\infty} C_n \cdot cos[ks_n(h+z)] \cdot e^{\left[-\sqrt{ks_n^2 + k_y^2}\, x\right]} \cdot \cos(k_y y - \omega t) \end{aligned}\right\} \tag{4}$$

$$where\ the\ following\ restriction\ applies: k \geq k_y$$

Combining the solution above with the dynamic and kinematic free surface B.C., it is obtained the dispersion relationship for progressive waves Eq. (5), and also the same relationship for the evanescent waves Eq. (6). Evanescent waves are produced by the mismatch of the paddle's shape and the velocity structure of the progressive wave, and decay exponentially at a distance from the wavemaker (2 to 3 times the water depth).

$$\omega^2 = gk \cdot \tanh(\boldsymbol{k}h) \tag{5}$$

$$\omega^2 = -g \cdot ks_n \cdot \tan(\boldsymbol{ks_n} \cdot h) \tag{6}$$

Here ω is the progressive wave frequency, $\boldsymbol{ks_n}$ is the evanescent wave number (a complex number), $\boldsymbol{k}$ is the progressive wave number, whose components are k_x and k_y can be expressed as indicated in Eq. (8) and Eq. (9); L is the wave length in meters, and T is the wave period in seconds, ω and $\boldsymbol{k}$ can be expressed also as indicated in Eq. (7).

$$\omega = \frac{2\pi}{T}, \qquad k = \frac{2\pi}{L} \tag{7}$$

$$k_x = \frac{2\pi}{L_x} = k \cdot cos\theta = \sqrt{k^2 - k_y^2} \tag{8}$$

$$k_y = \frac{2\pi}{L_y} = k \cdot sin\theta = \sqrt{k^2 - k_x^2} \tag{9}$$

Applying the B.C. at the wavemaker at x = 0, Eq. (10) is obtained. From this equation again for simplicity only the propagating mode is taken and using the orthogonal properties of {cosh[$k(h+z)$], and cos[$ks_n(h+z)$]} and integrating over depth (from $-h$ to 0) we can estimate the value of A_p as indicated in Eq. (11).

$$\left.\begin{aligned} U(z)\cdot\cos\left(k_y-\omega t\right) &= -\left.\frac{\partial\emptyset}{\partial x}\right|_{x=0} \\ U(z) &= -A_p\cdot k_x\cdot\cosh[k(h+z)] \\ &+\sum_{n=1}^{\infty} C_n\cdot cos[ks_n(h+z)]\cdot\sqrt{ks_n^2+k_y^2} \end{aligned}\right\} \quad (10)$$

$$A_p = -\frac{\int_{-h}^{0} U(z)\cdot\cosh[k(h+z)]\cdot dz}{k_x\int_{-h}^{0} cosh^2[k(h+z)]\cdot dz} \quad (11)$$

Here *U(z)* is defined as indicated in Eq. (12), although it can be defined for any type of wavemaker, for this case it follows:

$$\left.\begin{aligned} &U(z)=\frac{S(z)}{2}\cdot\omega\ ,where\ \ S(z)=S=stroke\ piston\ type\ wavemaker \\ &therefore \\ &U(z)=\frac{S}{2}\cdot\omega \end{aligned}\right\} \quad (12)$$

Solving Eq. (11), by employing Eq. (8) and Eq. (12) the solution for A_p is obtained as indicated by Eq. (13).

$$A_p = -\frac{2\cdot S\cdot\omega\cdot\sinh(kh)}{k[\sinh(2kh)+2kh]}\cdot[\cos(\theta)]^{-1} \quad (13)$$

On the other hand, in order to find the transfer function for a piston type wavemaker (ratio of wave height *"H"* to stroke *"S"*) it is needed to evaluate the wave height using the dynamic free surface B.C, and equating this with the solution for a progressive wave far from the wavemaker, where evanescent waves are not present, as indicated in Eq. (14). From this equation a transfer function Eq. (15) is obtained (also

known as the Biésel transfer function) by substituting Eq. (5) and Eq. (13) and solving for the ratio "*H/S*". Here Eq. (15) differentiates from the 2D case only by the $(\cos\theta)^{-1}$. Eq. (16) shows the transfer function solved for the stroke of the wavemaker (*"S"*).

$$\left.\begin{aligned}\eta = \frac{1}{g}\frac{\partial\phi}{\partial t}\Big|_{z=0} &= -\frac{A_p}{g}\cdot\omega\cdot\cosh(kh)\cdot\cos(k_x x + k_y y - \omega t)\\ &= \frac{H}{2}\cdot\cos\left(k_x x + k_y y - \omega t\right)\ for\ x \gg h\end{aligned}\right\} \tag{14}$$

$$\frac{H}{S} = \frac{4\cdot sinh^2(kh)}{2kh + \sinh(2kh)}\cdot(cos\theta)^{-1} \tag{15}$$

$$S = \frac{H\cdot[2kh + \sinh(2kh)]}{4\cdot sinh^2(kh)}\cdot cos\theta \tag{16}$$

It is important to notice that the stroke is effectively reduced by the "cosθ" factor, when generating waves at an angle, which is a well known fact when using the snake wave principle. A similar situation will occur when establishing the ARA theory, where because wave absorption is considered as the reverse process of wave generation (reversing time) not a full compensation needs to be applied but a reduced one by the "cosθ" factor.

Finally, in order to generate a realistic wave environment it is necessary to superimpose numerous wave motions. This is possible due to the linearity of the problem as it was indicated above. The previous derivation will be employed with a complex notation in the next section, and it will be extended to evanescent waves also, in order to study the general theory involved for developing ARA.

2.3 Three Dimensional ARA Theory

The theory presented for 3D ARA evolved from development of 2D ARA for flume wavemakers, with different types of feedback, including gages located at certain distance from the wavemakers paddles, e.g. Christensen and Frigaard (1994), with the wave gages attached to the paddle front, e. g. Hirakuchi et al. (1992), Schaffer et al. (1994), and Schaffer and Hyllested (1999), using force transducers in the paddle back, e.g. Salter (1981), or wave gages attached relatively close to the paddle front in a termination at the end of a flume, e.g. Milgram (1970). All of these approaches were applied to different types of wavemakers (piston type, hinged type, etc), and latter extended to 3D in quasi and fully 3D ARA (see Chapter I for classifications).

The analysis will start with the general theory used to develop a 3D ARA system, where the hydrodynamic feedback is provided by water surface elevation gages integrated in the paddle front. The theory presented here is found to be followed in general terms by most of the literature reviewed e.g. Hirakuchi et al. (1992), Ito et al. (1996), and it is consistent with that developed by Schaffer and Skourup (1996), Steenberg and Schaffer (2000), and Schaffer (2001).

Let us write the solution to the boundary value problem specified in Eq. (3) in complex notation for 3D (ϕ), Eq. (17), including evanescent modes, as well as water surface elevation (η), Eq. (18), and the paddle position (X_0), Eq. (19), for each wave component, which will be employed later, as follows.

$$\phi = \frac{1}{2}\left\{\frac{igX_a}{\omega}\cdot\sum_{j=0}^{\infty} e_j \cdot \frac{cosh\left[k_j(h+z)\right]}{\cosh\left(k_j h\right)}\cdot e^{i\left(\omega t - k_{xj}\cdot x - k_y\cdot y\right)} + c.c.\right\} \tag{17}$$

$$\eta = \frac{1}{2}\left\{X_a \cdot \sum_{j=0}^{\infty} e_j \cdot e^{i\left(\omega t - k_{xj}\cdot x - k_y\cdot y\right)} + c.c.\right\} \tag{18}$$

$$X_0 = \frac{1}{2}\left\{-i\cdot X_a \cdot e^{i\left(i\omega - k_y\cdot y\right)} + c.c.\right\} \tag{19}$$

X_a is the paddle amplitude at still water level, e_j is the frequency-directional transfer function related to the Biésel transfer function, c.c. denotes the complex conjugate of the preceding terms, and the rest of the terms maintain the definitions given before. Here we will redefine our notation for the wave number vector (***k***) with a more general form that covers progressive and evanescent wave numbers. Let us define $\boldsymbol{k_j}$ as the wave number vectors for progressive and evanescent waves, whose components are given by k_{xj} in the x-direction and k_y in the y-direction, furthermore we also define $k_{xj}^2 = k_j^2 - k_y^2$. For $j = 0$, $\boldsymbol{k_j}$ becomes $\boldsymbol{k_0} = \boldsymbol{k}$, and k_{xj} becomes $k_{x0} = k_x$, which was the original notation for the progressive wave number vector, and its x-direction component. For $j \geq 1$, the evanescent wave numbers are obtained, which are complex numbers, determined by solving Eq. (5) and Eq. (6).

Once defined the solutions for the boundary value problem for a wavemaker, it is necessary to start defining the equations involved in the study of ARA in 3D. Let's start by defining the components of this analysis by looking at a sketch in 2D presented in Fig. 2, where different waves are assumed to be present at once. Here it can be observed

waves representing the total elevation measured right in front of the paddle η_0, the total incident wave η_I, the reflected wave η_R, and the re-reflected wave η_{RR}, and also the paddle position X_0, where the subscripts are self explanatory. These waves and paddle position are related to the their respective complex amplitudes, $A_0, A_I, A_R, A_{RR},$ and X_a, through a 2D Fourier transform that goes from the time-space domain (t, y) to the frequency-wave number domain (ω, k_y) and vice versa.

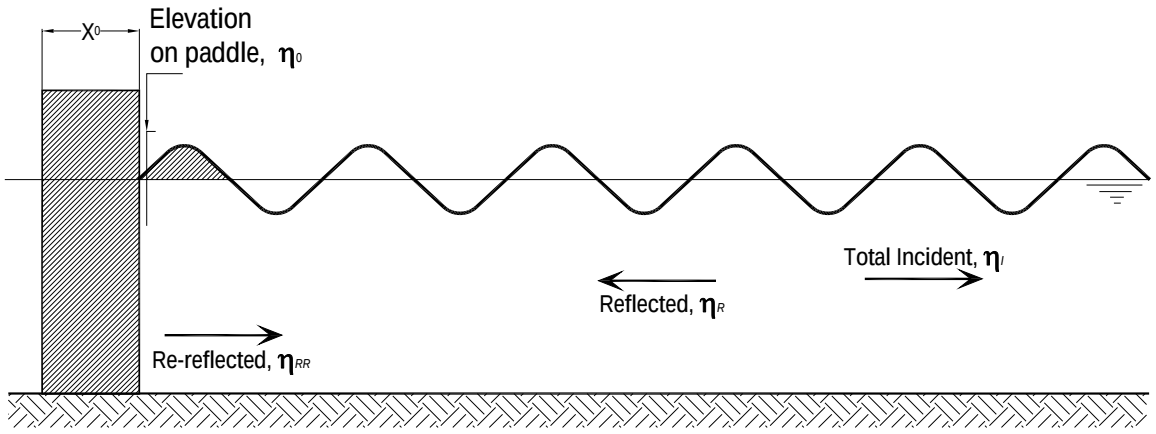

Fig. 2. Cross Section for a 2D-Piston Type Wavemaker, Showing Wave Components Considered in 2D and 3D ARA Theory

From Fig. 2, let us assume full re-reflection from the wave paddle when this one is at rest at x = 0 (mean position), where all the elevations and equivalent amplitudes mentioned above are taken at this point, therefore the following equations derived from Eq. (18) and Eq. (19) apply.

$$\eta_I = \frac{1}{2}\left\{A_I \cdot e^{i(\omega t - k_{xj} \cdot x - k_y \cdot y)} + c.c.\right\} \tag{20}$$

$$\eta_0 = \frac{1}{2}\left\{A_0 \cdot e^{i(\omega t - k_y \cdot y)} + c.c.\right\} \tag{21}$$

$$X = \frac{1}{2}\{X_a \cdot e^{i(i\omega - k_y \cdot y)} + c.c.\} \tag{22}$$

where

$$A_I = i \cdot X_a \cdot e_0 + A_R \tag{23}$$

$$A_0 = i \cdot X_a \cdot \left[e_0 + \sum_{j=1}^{\infty} e_j\right] + A_R + A_{RR} \tag{24}$$

$$A_R = A_{RR} \tag{25}$$

In Eq. (24) use has been made of the following expansion with the purpose to identify the evanescent modes: $\sum_{j=0}^{\infty} e_j = e_0 + \sum_{j=1}^{\infty} e_j$, which are present together with reflected and re-reflected waves at the paddle front. Also notice the use of "i" the imaginary unit that represents a 90^o phase shift, due to the reflection consideration at the paddle front and the reflective side. Let us furthermore eliminate A_R, and A_{RR} , considering full absorption, using Eq. (23) to Eq. (25) in order to obtain X_a as follows:

$$X_a = (2A_I - A_0) \cdot F \tag{26}$$

where

$$F = -\frac{i}{e_0 - \sum_{j=1}^{\infty} e_j} = \frac{1}{i \cdot \left[e_0 - \sum_{j=1}^{\infty} e_j\right]} \tag{27}$$

Eq. (27) corresponds to a transfer function that is based on a frequency-direction basis that will control the simultaneous generation and absorption of the system. In other words this equation represents in 3D a frequency-direction dependent ratio of the complex amplitude of the piston wavemaker, X_a, to the complex amplitude of the water

surface elevation right in front of the paddle at x = 0, A_0, for no reflected waves. In Eq. (27) it needs to be pointed out that in practice, the servo loop of the ARA and communication of the system introduce a delay, which needs to be taken into account in the design of a 2D recursive filter, which is one way to implement Eq. (27) in the time-space domain. Also this transfer function needs to be matched by the recursive filter in a frequency band that is useful for physical tests and performance of the wavemaker components, which becomes difficult in 3D. Here it is neglected the delay mentioned above for simplicity of the derivation. In order to complete the theory for 3D ARA let us define e_j as follows:

$$e_j = \frac{k_j}{k_{xj}} \cdot c_j = \frac{1}{\cos(\theta)} \cdot c_j \tag{28}$$

and

$$c_j = \frac{4 \cdot sinh^2(k_j h)}{2k_j h + \sinh(2k_j h)} \tag{29}$$

Here it can be seen that the directional dependence comes through e_j, mainly for $j = 0$, and to a smaller degree for $j \geq 1$. Also c_j corresponds to the transfer functions for normally emitted waves $(k_y = 0)$, or in other words when $\theta = 0$, which is the 2D-ARA case. Therefore Eq. (29) is identical to the Biésel transfer function defined before in Eq. (15), without the directional influence (2D), when $j = 0$. Eq. (28) can be reduced to 2D as it was just mentioned. Therefore this serves to demonstrate that by being able to calculate the angle of incidence of the reflected waves and using a 2D-ARA

approximation (1D recursive filter in time) we can achieve a Fully-3D ARA system, without the complications of fitting a 2D recursive filter in time and space, which as mentioned above is difficult. On the other hand, the ARA performance based on the theory just discussed is presented in the next section.

2.3.1 Theoretical Estimation of ARA Performance

It is important to evaluate the performance of an ARA system, which can be derived from the theory presented above. The following explanation to establish the theoretical performance of ARA can also be found in Schaffer et al. (1994), and Schaffer (2001). Let us assume that full reflection occurs at the paddle at rest, and that water follows the linear wavemaker theory presented before. Under these assumptions Eq. (23) to Eq. (26) can be re-written as follows:

$$\widetilde{A_I} = i \cdot \widetilde{X_a} \cdot e_0 + \widetilde{A_{RR}} \tag{30}$$

$$\widetilde{A_0} = i \cdot \widetilde{X_a} \cdot \left[e_0 + \sum_{j=1}^{\infty} e_j \right] + \widetilde{A_R} + \widetilde{A_{RR}} \tag{31}$$

$$\widetilde{A_R} = \widetilde{A_{RR}} \tag{32}$$

$$\widetilde{X_a} = \left(2A_I - \widetilde{A_0}\right) \cdot \tilde{F} \tag{33}$$

Here and in the next equations, the actual quantities (measured or realized) are represented with a tilde. Also notice that quantities without a tilde indicate the desired

value (theoretical). A definition of coefficient of generation for a wavemaker based on the equations presented above can be derived by using $\widetilde{A_0}$ from Eq. (31) in Eq. (33), where the quantity obtained is $\widetilde{X_a}$, which is then used in Eq. (30), and after some algebraic manipulation we obtain the coefficient of generation indicated in Eq. (34).

$$\lambda_{gen} = \left|\frac{\widetilde{A_I} - \widetilde{A_R}}{A_I - \widetilde{A_R}}\right| = \left|\frac{2 \cdot e_0}{-\frac{i}{\tilde{F}} + e_0 + \sum_{j=1}^{\infty} e_j}\right| \tag{34}$$

From the coefficient above the re-reflection coefficient of the wave maker can be further defined, this coefficient is obtained by considering $A_I = 0$, this is to obtain only the ratio of the unwanted re-reflected wave ($\widetilde{A_I} = \widetilde{A_{RR}}$, from Eq. (30), when no progressive wave is generated) to the reflected wave returning to the wavemaker ($\widetilde{A_R}$). The previous explanation can be better understood by writing the re-reflection coefficient as indicated in Eq. (35).

$$RR_{coef} = 1 - \lambda_{gen} = \frac{\widetilde{A_I} - A_I}{\widetilde{A_R} - A_I} \tag{35}$$

By using Eq. (34) and Eq. (35), it is possible to estimate the theoretical performance of the ARA system at hand, given the characteristics of $\tilde{F}$, which in this development is focused to a 3D-ARA system; however it can be easily reduced to a 2D-ARA as it has been indicated previously.

2.3.2 Physical Estimation of ARA Performance

In order to obtain a similar expression, as the one derived in the previous section, to calculate the performance of the ARA system from a physical experiment it is needed to multiply both numerator and denominator of Eq. (35) by $\widetilde{X_a}$ (actual paddle displacement), and eliminating $\tilde{F}$ by Eq. (33), the following equation is obtained.

$$\lambda_{expgen} = \left| \frac{2 \cdot e_0 \cdot \widetilde{X_a}}{-i\left(2A_I - \widetilde{A_0}\right) + \widetilde{X_a} \cdot \left[e_0 + \sum_{j=1}^{\infty} e_j\right]} \right| \tag{36}$$

$$RR_{expcoef} = 1 - \lambda_{expgen} \tag{37}$$

The previous equations include all the information required to estimate the practical performance of the ARA system, which can be compared with the theoretical one as indicated in Eq. (34) and Eq. (35). Any discrepancy between both corresponds to an unexpected behavior of the control system.

On the other hand the re-reflection coefficient can be calculated from the same physical experiments by gathering data that allow us to separate incident and reflected waves in a closed basin that is opened later. Here waves are reflected back to the wavemaker from normal (2D), and oblique angles (3D), in continuous and burst modes (these concepts will be defined in the next chapter). By knowing the incident wave height (in this case given by the reflected wave height H_R), and reflected wave height (in this case given by the re-reflected wave height H_{RR}), it can be calculated from experiments the re-reflection coefficient for a burst mode experiment by using the zero-

crossing method to feed Eq. (38), or by performing an analysis using the power spectral density method. Finally for continuous mode the re-reflection coefficient can be calculated as indicated in Eq. (39). In the next section it is covered the ARA loop.

$$Kr_{burst} = \frac{H_{RR}}{H_R} \tag{38}$$

$$Kr_{cont} = \frac{H_{I\ closed} - H_{I\ open}}{H_{R\ closed}} = \frac{H_{RR}}{H_R} \tag{39}$$

2.4 ARA Loop for TAMU Wave Generator

The ARA loop for the 48-paddle 3D multidirectional wave generator, installed by Bosch-Rexroth at the Haynes Coastal Engineering Laboratory, is explained in this section. This ARA loop is considered a real-time algorithm, which in principle works as presented in Fig. 3. Here the theory presented before is not obvious, basically due to the way that such theory needs to take when implemented in a discrete way. On the other hand, a portion of the theory was implemented using a program called GEDAP (Generalized Experiment Control and Data Acquisition Package, Miles, 1997).

The use of this program corresponds to the calculation of the paddle displacement, called setpoint position which creates the theoretical wave and the water surface elevation in front of the paddle, called setpoint level which is used to correct any deviating water level measured at the segment front.

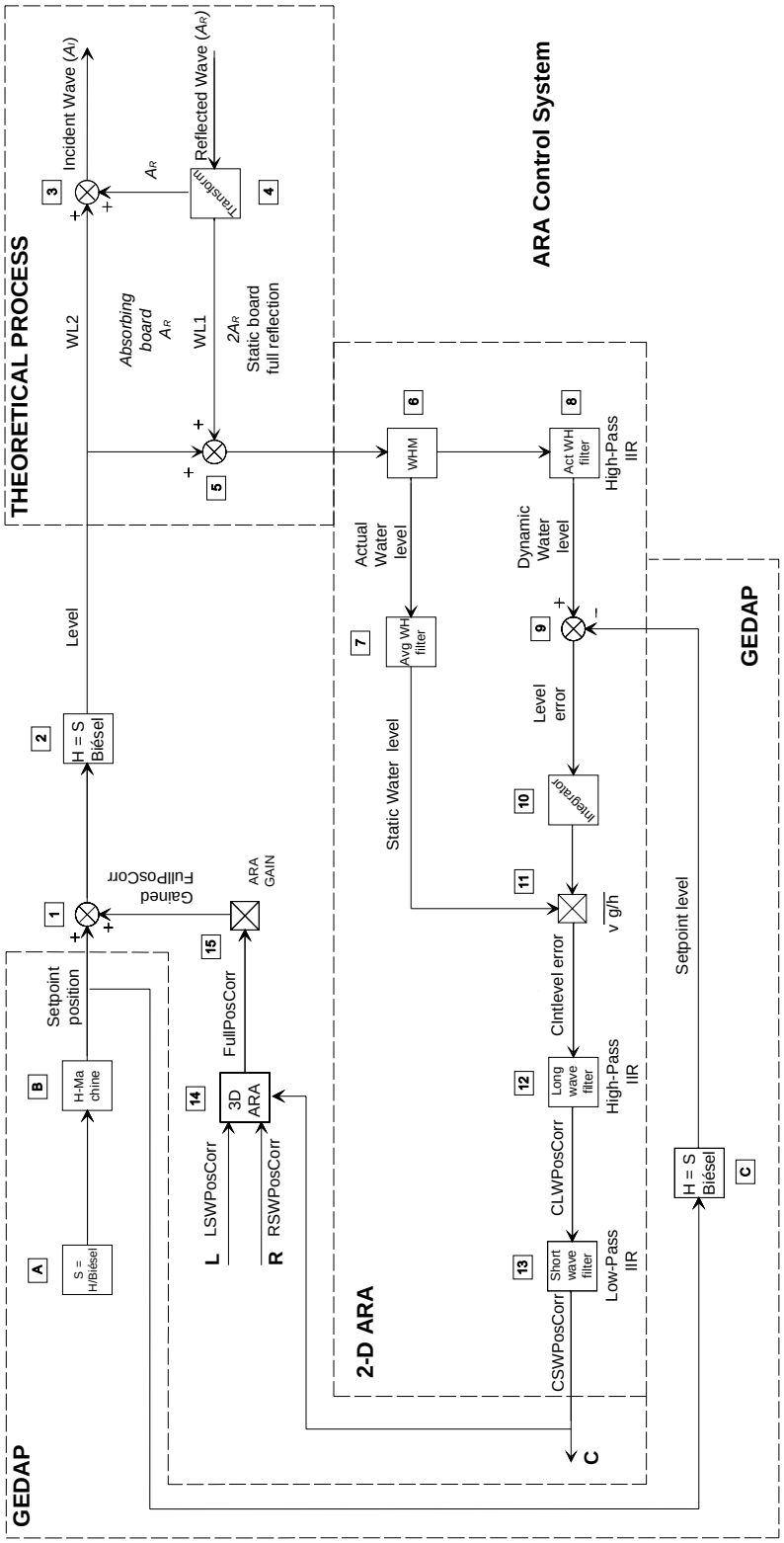

Fig. 3. Schematic of Control System (ARA Loop) for Individual Paddle (Bosch-Rexroth)

GEDAP calculates both setpoints using the Biésel transfer function (H-Biésel) as derived before for a piston type wavemaker. Then both signals are adjusted to account for the mechanical dynamics of the system using the machine transfer function (H-machine). Both signals are then stored in a file which links them together, so they can be played by the controlling software. The process just described is performed by blocks A, B and C, under the dashed block named GEDAP.

Focusing for a moment on the system, this works by having each segment equipped with wave height meters on the wave-board front, which measure the actual water level. Their working principle is based on the measurement of electrical capacitance between two conductors. Thus the measurement is sensitive to local variations in specific water parameters as temperature and conductivity. The wave height meter produces a signal proportional to the instantaneous water level at the segment. This signal is then to be processed in a suitable ARA algorithm in order to compensate certain water level profile; this process is explained in the next paragraphs.

Continuing with Fig. 3, the setpoint position is fed to block 2, which contains H-Biésel that converts wave board position back to level. The previous signal feeds a portion of the loop that corresponds to an explanation of the theoretical process of generation and reflection of waves (dashed block named Theoretical Process). Here it is considered that the wave height meter described above (WHM, block 6) will obtain its input from measurement of the elevation of the progressive wave generated by the wavemaker (block 2) and any reflection arriving to the paddle (block 4). This portion of the loop is similar to the theory presented in Eq. (23) to Eq. (25).

The difference comes at the time of making the consideration of a moving-absorbing board or a static board, where block 4 makes the transformation to either one of these two modes, and always outputs the reflected wave to be added in block 3 to the progressive wave that will result in the incident wave propagating towards the tank.

The resulting signal from block 6 is called ActualWaterLevel, which is then to be filtered in block 7 (AvgWHFilter, analog low-pass filter) in order to subtract the dynamic signal component and thus obtain the static water level, and block 8 (ActWHFilter, an IIR high-pass filter) that removes the static signal component and thus obtain the dynamic water level. Next, the dynamic water level is subtracted (block 9) with the water level setpoint, coming from the setpoint level in the file provided by GEDAP. This subtraction is performed to obtain the water level error. Here it is considered that any level error must be caused by waves traveling towards the paddle and that a correction to the paddle motion can reduce the level error.

The process continues with integration of the level error in block 10, where the output is multiplied with $\sqrt{g/h}$ (block 11), where g is the gravity acceleration constant, and h is the static water level obtained from block 7. The resulting signal is named CIntLevelError which is the input for block 12 (LongWaveFilter). Block 12 contains an IIR high-pass filter which main purpose is to avoid saturation of the paddle, its output is named CLWPosCorr and becomes the input of block 13 (ShortWaveFilter). Block 13 contains an IIR low-pass filter, whose purpose is to improve the performance of the system for higher frequencies (controlling stability and phase delay); its output is named

CSWPosCorr. This last position correction is made available by the software to be used for control loops of adjacent segments.

Let us stop briefly, to indicate the theory behind the long wave filter mentioned above. To obtain perfect absorption the paddle's velocity needs to match the velocity of the waves to be absorbed (in this case following the linear long wave theory) which requires a velocity as indicated in Eq. (40).

$$U(t) = \sqrt{g/h} \cdot \eta(t) \tag{40}$$

This velocity must be integrated in order to obtain the paddle position as indicated in Eq. (41).

$$X(t) = \sqrt{g/h} \cdot \int_{-\infty}^{t} \eta(t) \cdot dt \tag{41}$$

Shifting Eq. (41) to the frequency domain and letting A and X_a^{lw} (where *lw* means long wave) denote the respective complex amplitudes for η and X, a relationship is derived between A and X_a^{lw} that can be written as previously indicated in Eq. (26), where $A = (2A_I - A_0)$, therefore.

$$X_a^{lw} = A \cdot \sqrt{g/h} \cdot \frac{1}{i\omega} \tag{42}$$

The last portion in Eq. (42) is the long wave filter response that needs to be fitted in the control loop. In order to complete the linear full-spectrum wave theory for this

ARA loop, use of a short wave filter was implemented also, in order to damp the high frequency response of the system, the filter is an IIR low-pass filter as already indicated.

The description presented above corresponds to the dashed block named 2D-ARA, and it is executed for each paddle. Summarizing, the purpose of the 2D-ARA block is to cause the segments to move in such a position, that the influence of reflected waves (traveling towards the segments) will be sensed and reduced optimally while simultaneously generating the desired wave. Even during wave generation, ARA will remain in function, and any parasitic waves in the basin will be dampened out. As mentioned previously the system can switch from 2D ARA mode to 3D ARA mode.

For the case where 3D ARA mode is selected (block 14), it is required to obtain the position corrections coming from adjacent paddles (LSWPosCorr and RSWPosCorr), that together with the center position correction (CSWPosCorr), are used to obtain the signal called FullPosCorr for the center paddle. Block 14 obtains this signal using a distribution, that consists in taking a percentage of the position correction signal from each paddle (%L, %C, and %R), therefore when they are added a total of 100% for the center paddle position correction is obtained; this has been noted as the spatial gain mixer. This correction is multiplied by a gain (block 15, ARA gain) in order to regulate the influence of ARA on the system. Finally, the signal obtained from block 15 is named GainedFullPosCorr, which is applied by virtue of the superposition principle to the setpoint position (block 1) which closes the loop. The performance of the ARA loop is sensitive to control delay.

The algorithm described in Fig. 3 is considered a good approximation for a Fully 3D-ARA system, with the limitations mentioned in chapter I. Here, matters such as timing, data acquisition, fading in/out, etc, are taken care of by the existing software. Standard control objects, such as low-pass and high-pass filters are linked to the built-in data logger and analog test outputs. This gives considerable advantage in development and troubleshooting of the system (Bosch-Rexroth, 2004).

Another resource provided by the built-in software from Bosch-Rexroth is the Frequency Response Analyzer control software that allows the user to measure transfer functions by performing a frequency sweep. This is extremely useful when the transition in the transfer function is gradual. The analyzer was used to obtain the H-machine transfer function (as required by GEDAP) which due to the sensitivity of the ARA algorithm was used to compensate for any depth change.

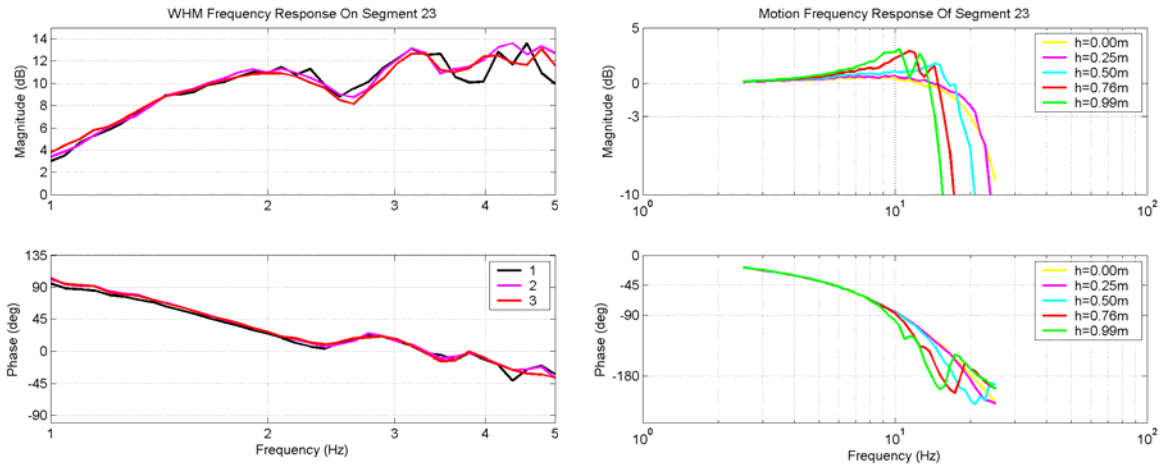

Fig. 4. Frequency Response Analyses for Typical Individual Paddle

Also the analyzer can be used for every single paddle of the wavemaker, that allow the measurement and analysis of the frequency response to properly calculate the

filter coefficients used (long wave and short wave filters) that will keep the system stable (Fig. 4).

2.5 Proposed Theory for DOA of Reflected Waves

Now it is presented an approach that consists in finding the DOA of the reflected waves applying concepts related to bearing estimation, which will handle the problem in the time-space domain, eliminating the necessity of employing a 2D recursive filter design to fit the theoretical directional transfer function for ARA application. Moreover it is proposed to only employ a 2D-ARA approach to obtain a stable system with a working frequency range adequate for physical experiments in a wave basin, and calculate the proper correction to the paddle position using the angle from the method that will be explained, which calculates the DOA of the reflected waves in as few as 5 snapshots.

This is an interesting approach since the gages placed in front of the paddles in the wavemaker can be used in an antenna fashion (array) to be able to determine the direction of arrival of the reflected waves. Beamforming is really an application of spatial wave number filtering where waves from different directions represent different sampled wavelengths at the array sensor locations (Swanson, 2000). The importance of estimating this angle comes from what has been explained by Ito et al. (1996), where the problem is that the system overreacts for oblique waves due to the correction applied to the paddle position which does not take $\cos(\theta)$ into account in a Quasi-3D ARA, or

Fully 3D-ARA if using a spatial gain mixer, creating spurious waves. Ideally the paddle excursions should be a factor of $\cos(\theta)$ smaller than that for the perpendicular case.

There are various techniques that can be employed to localize the direction of the waves. The following is a brief explanation of what bearing estimation is about, and the method found in literature that better couples with the ideas shown herein.

2.5.1 Bearing Estimation

There is a variety of topics covering the theory to estimate the angle of incidence for planar waves through use of an array of sensors located in line. The simplest way to perform this estimation and also the easiest way to explain the concept is through the following formulation:

$$\beta = cos^{-1}\left[\frac{\Delta\phi_{s2-s1}}{k \cdot d}\right] \tag{43}$$

This is generally known as “Direction cosine” or “Phase interferometric” where: k is the wave number, d is the distance between sensors in meters, $\Delta\phi_{s2-s1}$ is the phase difference (Phase sensor 2 – Phase sensor 1), or in other words $\Delta\phi_{s2-s1} = k \cdot d \cdot cos\beta$. Here the idea is to measure the relative phases across the array depending on the wavelength or frequency. With this information the angle of incidence with respect to the array axis can be estimated (within the half-plane above the linear array). Fig. 5 shows a general description of bearing estimation using direction cosine.

However this method is only a direct measurement of the angle of incidence of a single plane wave frequency. This research proposes the use of a more sophisticated method to calculate the direction of arrival of the reflected waves that also does it in the fastest way possible.

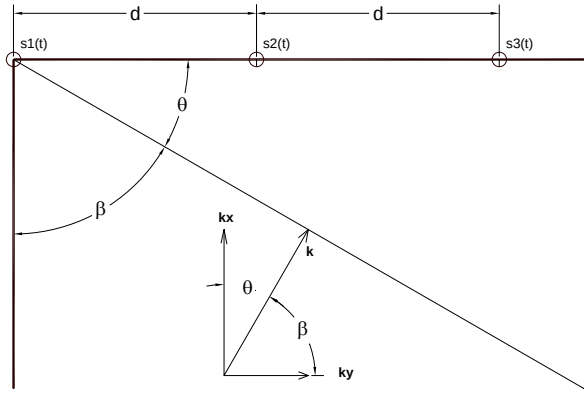

Fig. 5. General Description of Bearing Estimation Using Direction Cosine

Several methods are found that can perform the calculation of the angle of incidence of a planar wave, among them stand out; Bartlett method, Capon method, and MUSIC method (Multiple Signal Classification). The MUSIC algorithm is a subspace method (set of coordinates obtained from data vectors to produce a reduced-dimensional representation by linear projection into a subspace) that has different variations that allow its use for coherent signals, as would be the case in a wave tank, where the main objective is to obtain a covariance matrix with the data provided by the array elements, to determine the DOA of reflected waves. However, many data snapshots coming from an array are required to obtain a good performance, which will limit ARA performance.

The Bosch-Rexroth wavemaker and control system provide us with measurements of frequencies and sensor position (paddle position) with great accuracy

in real time. Therefore in order to apply this algorithm, or any other in the literature it is needed to make a reasonable assumption of the wave length for a given plane wave frequency. Based on the reasons discussed above we applied a method that can be adapted in real time to our control system, this method is explained in the next section.

2.5.2 Direct Data Domain Adaptive (DDDA) Beamformer*

A method explained by Kim et al. (2005) that uses a modified MUSIC approach is considered to achieve the calculation of θ in real time. The theory presented here fits very nicely with the control system of the wave maker at TAMU. The method proposes an algorithm that can estimate rapidly the DOA's of different signals (waves) by using a pseudo-covariance matrix even under coherent environments. The main advantage of this method is that it can calculate a bearing response after obtaining the pseudo-covariance matrix just after one snapshot, even when signals are correlated, this makes it a good option to be applied. In general this method relies on a direct data domain adaptive (DDDA) beamformer to obtain a pseudo-covariance matrix after one snapshot.

---

* Part of the data reported in this section is reprinted, with permission, from: ©2005 IEEE Transactions on Antennas and Propagation. Paper: Fast DOA estimation algorithm using pseudocovariance matrix. Authors: Jung-Tae Kim; Sung-Hoon Moon; Dong-Seog Han; Myeong-Je Cho. Volume 53, Issue 4, April 2005, Page(s): 1346-1351.

Then it obtains very roughly the incidence angle ranges of the signals by using the bearing response. Finally the exact incidence angles are obtained by using the bearing response and directional spectrum.

Consider a uniform linear array with *N* elements (wave height meters) that will be used to detect *R* narrow-band signals arriving from *R* directions $\theta_1, \theta_2, \dots, \theta_R$, where the angles $\theta_j,\ j = 1,2, \dots, R$, are defined from the broadside direction of the array (in this case the line formed by the sensors from where signals arrive). Fig. 6 shows this arrangement.

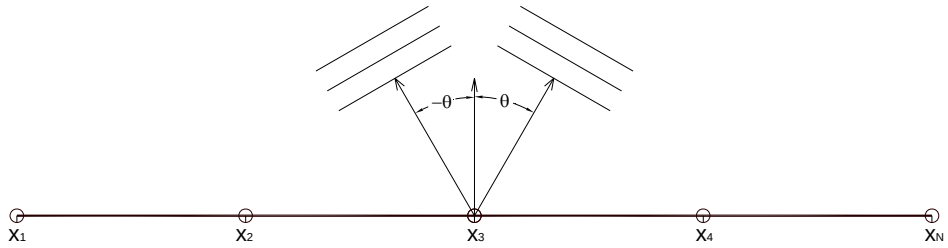

Fig. 6. Uniform Linear Array Formed with Wave Height Meters Attached to the Paddle Front

The signal vector $\mathbf{x}(k)$ impinging on the array at time k is defined in Eq. (44) as

$$\begin{matrix} [N\text{x}1] & [N\text{x}R] & [R\text{x}1] & [N\text{x}1] \\ \boldsymbol{x}(k) = & \boldsymbol{A}(\boldsymbol{\Theta}) & \boldsymbol{s}(k) + & \boldsymbol{n}(k) \\ = [x_1(k), x_2(k), \dots, x_N(k)]^T & & & \end{matrix} \tag{44}$$

The superscript *T* denotes a transpose, $\boldsymbol{A}(\boldsymbol{\Theta})$ is a matrix consisting of steering vectors, $\boldsymbol{s}(k)$ is the signal vector consisting of *R* different incidence signals, and $\boldsymbol{n}(k)$ is the white noise vector generated at each array element with a zero mean and variance of σ_n^2. $\boldsymbol{A}(\boldsymbol{\Theta})$, $\boldsymbol{s}(k)$ and $\boldsymbol{n}(k)$ are presented in Eq. (45) through Eq. (47) as

$$\boldsymbol{A}(\boldsymbol{\Theta}) = [a(\theta_1), a(\theta_2), \dots, a(\theta_R)] \tag{45}$$

$$\boldsymbol{s}(k) = [s_1(k), s_2(k), \dots, s_R(k)] \tag{46}$$

$$\boldsymbol{n}(k) = [n_1(k), n_2(k), \dots, n_N(k)] \tag{47}$$

Here *N* stands for the number of sensors used in the calculation (must be an odd number), *R* corresponds to the number of narrow-band signals to be detected. Furthermore, $\boldsymbol{a}(\theta_j), j = 1,2, \dots, R$, are the steering vectors of $s_j(k)$ coming from θ_j. The *j*-th steering vector $\boldsymbol{a}(\theta_j)$ is indicated in Eq. (48) as

$$\boldsymbol{a}(\theta_j) = \left[1, e^{i\frac{2\pi d}{L}\cdot \sin(\theta_j)}, \dots, e^{i\frac{2\pi d}{L}\cdot (N-1)\cdot \sin(\theta_j)}\right]^T \tag{48}$$

Here *d* corresponds to the separation between sensors, and *L* represents the wave-length of the carrier. Fig. 7 shows the DDDA beamformer structure as indicated by Kim et al. (2005).

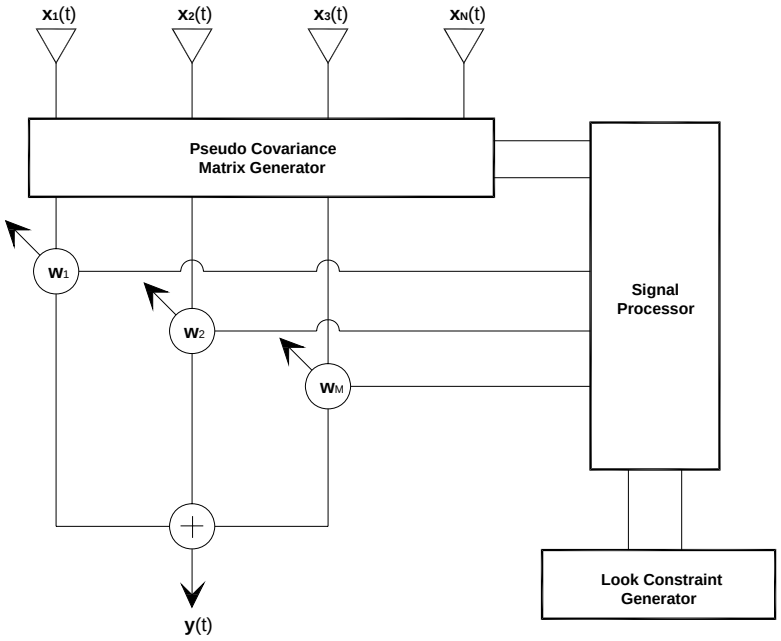

Fig. 7. DDDA Beamformer Structure

From the figure above the pseudo-covariance matrix generator builds $\boldsymbol{X}(k)$ as indicated in Eq. (49).

$$\boldsymbol{X}(k) = \begin{bmatrix} x_1(k) & x_2(k) & \dots & x_M(k) \\ x_2(k) & x_3(k) & \dots & x_{M+1}(k) \\ \vdots & \vdots & \ddots & \vdots \\ x_M(k) & x_{M+1}(k) & \dots & x_N(k) \end{bmatrix} \tag{49}$$

Where $M = (N+1)/2$, the pseudo-covariance matrix $\boldsymbol{X}(k)$ is the signal received at the antenna elements, and performs a similar function to a covariance matrix. When the look direction of the beamformer is θ_s, $\boldsymbol{a}(\theta_s)$ can be expressed as indicated in Eq. (50).

$$\begin{aligned} \boldsymbol{a}(\theta_s) &= [a_1(\theta_s), a_2(\theta_s), \dots, a_N(\theta_s)] \\ &= \left[1, e^{i\frac{2\pi d}{L}\cdot \sin(\theta_s)}, \dots, e^{i\frac{2\pi d}{L}\cdot (N-1)\cdot \sin(\theta_s)}\right]^T \end{aligned} \tag{50}$$

The look constraint generator transposes $\boldsymbol{a}(\theta_s)$ into Eq. (51) as

$$\boldsymbol{S}(\theta_s) = \begin{bmatrix} a_1(\theta_s) & a_2(\theta_s) & \dots & a_M(\theta_s) \\ a_2(\theta_s) & a_3(\theta_s) & \dots & a_{M+1}(\theta_s) \\ \vdots & \vdots & \ddots & \vdots \\ a_M(\theta_s) & a_{M+1}(\theta_s) & \dots & a_N(\theta_s) \end{bmatrix} \tag{51}$$

Here it is assumed that $\alpha\, \boldsymbol{S}(\theta_s)$ is the incident signal from the look direction θ_s, where α is the signal strength. The vector $\boldsymbol{v}$ for minimizing the noise power is defined to satisfy

$$[\boldsymbol{X}(k) - \alpha\, \boldsymbol{S}(\theta_s)][\boldsymbol{v}] = [0] \tag{52}$$

Eq. (52) can be expressed as an eigenvalue equation given by

$$\boldsymbol{X}(k)\, \boldsymbol{v} = \alpha\, \boldsymbol{S}(\theta_s)\, \boldsymbol{v} \tag{53}$$

In Eq. (53), the eigenvalue decomposition results in a diagonal matrix composed of generalized eigenvalues and full matrix whose columns are the corresponding eigenvectors, where α is the smallest eigenvalue and $\boldsymbol{v}$ is an $M\,x\,1$ eigenvector corresponding to α. The eigenvector $\boldsymbol{v}$ is defined as a noise subspace. Therefore, eigenvector $\boldsymbol{v}$ is orthogonal to other steering vectors except for the steering vector for the look direction θ_s. The constraint condition is determined as indicated in Eq. (54).

$$\boldsymbol{w}(\theta_s)^T \tilde{\boldsymbol{a}}(\theta_s) = 1 \tag{54}$$

where $\boldsymbol{w}(\theta_s) = [w_1(\theta_s), w_2(\theta_s), \dots, w_M(\theta_s)]^T$ and $\tilde{\boldsymbol{a}}(\theta_s) = \left[1, e^{i\frac{2\pi d}{L}\cdot \sin(\theta_s)}, \dots, e^{i\frac{2\pi d}{L}\cdot(M-1)\cdot \sin(\theta_s)}\right]^T$ is the steering vector for the look direction θ_s with $M\,x\,1$ dimension. The weight vector can be obtained from the eigenvector $\boldsymbol{v}$ and the steering vector $\tilde{\boldsymbol{a}}(\theta_s)$ as

$$\boldsymbol{w}(\theta_s) = \frac{\boldsymbol{v}}{\boldsymbol{v}^T \tilde{\boldsymbol{a}}(\theta_s)} \tag{55}$$

where $\boldsymbol{w}(\theta_s)$ is an $M\,x\,1$ vector, when the array is steered to the look direction θ_s, the output of the array $y(k)$ is defined by Eq. (56) as

$$y(k) = \sum_{m=1}^{M} w_m(\theta_s)\, x_m(k) = \boldsymbol{w}(\theta_s)^T \tilde{\boldsymbol{x}}(k) \tag{56}$$

where $\tilde{\boldsymbol{x}}(k) = [x_1(k), x_2(k), \ldots, x_M(k)]^T$

The output power can be minimized by the weight vector $\boldsymbol{w}(\theta_s)$ whose pattern nulls are formed based on the directions of the signal except for the incident signal from the look direction.

The array should satisfy $R \leq M$ to discriminate all incidence signals. In general when using adapting array systems, determination of DOA becomes difficult under correlated signal conditions, as is the case in a wave basin. If the MUSIC algorithm (which is a stochastic method) was to be employed, use of secondary data would be required to overcome the problem of correlated signals due to signal cancellation in order to estimate the DOA. In applying the proposed technique this problem is avoided since this algorithm is a deterministic method, and determining the DOA does not require secondary data. Therefore in the proposed method there is no signal cancellation problem, even with correlated signals present.

Let us define now the output power array $P_B(\theta_s)$, also known as the array bearing response, as indicated in Eq. (57).

$$P_B(\theta_s) = \frac{1}{K} \sum_{i=1}^{K} y(k) y(k)^* \tag{57}$$

Here K is the number of snapshots in time required to observe the output power. In order to get a more accurate DOA of the incident signals, we must use the directional

spectrum, for which we need to search first the smallest bearing response from Eq. (57), which is denominated $\theta_{P_{min}}$ and it is indicated in Eq. (58) as

$$\theta_{P_{min}} = arg_{\theta_s} \min P_B(\theta_s) \tag{58}$$

It is required to obtain the corresponding weight vector $\boldsymbol{w}(\theta_{P_{min}})$ from the already performed DDDA beamforming. Finally the normalized directional spectrum can expressed as indicated in Eq. (59) as

$$P_D(\theta) = 10\ log_{10}\left\{\frac{1}{\left|\boldsymbol{w}(\theta_{P_{min}})^T \tilde{\boldsymbol{a}}(\theta)\right|^2}\right\} \tag{59}$$

The theory presented above was implemented through Matlab™ and Simulink™. A program developed in Matlab™ was created to apply the DDDA beamforming technique in order to calculate the bearing response and the directional spectrum, from which the DOA of the reflected waves is obtained; this was done in real time in as few as 5 snapshots. The actual implementation of the DOA algorithm presented in this section, to the physical system (control software) depends on cooperation with Bosch-Rexroth. However we consider that the codified algorithm can be easily implemented in the control software.

CHAPTER III

METHODOLOGY

3.1 Introduction

This chapter will concentrate on the methodology followed to accomplish the objectives of this research. A description of the experiments as well as the procedures employed will be presented. The main points included here are related to evaluation and analysis of the system stability for the ARA loop, estimation of the coefficient of re-reflection of the wavemaker from theory and physical tests, codification of the algorithm for DOA, physical testing to feed the program for DOA, and gathering data from the system itself that will be used with the DOA program in combination with a Simulink™ program of the ARA loop. The program will allow for comparison with results obtained with the original spatial gain mixer.

3.2 Evaluation of the ARA Loop as Implemented by Bosch-Rexroth

One of the first steps followed to evaluate the ARA system stability was to obtain a frequency response analysis (FRA), of the input and output signals for the ARA loop with open and closed loop conditions. This was done to evaluate the influence of the filters employed for ARA especially for the short wave filter (low-pass filter, designed

by Bosch-Rexroth); this was accomplished employing the FRA analyzer from the control software (Pandora) provided with the wavemaker. With the data obtained an evaluation of the system was conducted employing built in functions already developed in Matlab™ to apply the Nyquist criterion to determine stability (Nyquist diagram). The system is stable if no encirclements of -1 occur.

On the other hand preliminary runs without any data recording were conducted with a configuration similar to that described in the next sections; with the purpose of visualizing the performance of the ARA system working in 2D ARA mode. The short wave filter was tested this way. Then the performance was analyzed using the 3D ARA mode for which data was recorded, and description is made in the next sections. Based on the qualitative behavior of the 2D ARA mode, and data recorded for the 3D ARA mode it was decided to design a new short wave filter and test it with measurements in the basin, in order to compare it with the original. This filter was designed using a program developed in Matlab™ which incorporates a lead-lag filter based on a Butterworth filter. A discussion of the new filter vs. the original filter and a description of their performance are made in Chapter IV.

3.3 Estimation of the Coefficient of Re-reflection from Theory and Physical Tests

The theoretical performance of the ARA loop for the TAMU wavemaker, based on the evaluation of the re-reflected coefficient, followed the theory presented already in the previous chapter, and a program developed in Matlab™ carried out the calculations.

For a physical estimation of the performance it would be ideal to test the ARA system at hand using another wave generator from which waves will travel towards the paddles of the wavemaker with ARA activated. Since this is not the case, a series of experiments were considered using reflected waves to test the 3D ARA mode of our wavemaker. The next sections describe the equipment, materials and tests carried.

3.3.1 Wavemaker Description

The wave generator is located on the west wall of a 3D basin 75ft wide (22.86 m), by 120 ft long (36.58 m) by 5ft height (1.524 m). It has 48 paddles or wave boards (each about 0.474 m wide); each is driven by a ball spindle and nut which are in turn driven by a digital AC-servomotor, or actuator. By converting the rotary motion of the actuator, the ball spindle is able to move in a linear motion guided by two ball guide rails. Each actuator contains feedback of the position and velocity of the paddle and is controlled by a Motor Controller which is mounted inside a nearby Motor Control Cabinet (MCC). Each MCC serves eight actuators and is controlled by a Serial Real-time Communication System (SERCOS) interface via fiber-optic cable from its respective Control Computer.

From the Operator Station the waves are calculated, generated and the system is monitored. The Operator Station is networked to the Control Computer Cabinet (CCC), which consists of three Control Computers. Each Control Computer governs the motion of 16 paddles through two MCCs. The first computer, the master computer, serves the

first 16 paddles. The second and third Control Computers serve paddles 17-32 and 33-48 respectively. The SERCOS interface provides control parameters and set points for segment positions to the Motor Controller and the actual position and torque of the paddles is retrieved from the Motor Controller. In addition the Motor Controller is able to limit the maximum velocities and torque; also if the motor should travel beyond these limits the system will perform a controlled emergency stop.

The Control Computers receive data and commands from the Operator Station and then distribute segment set points to their respective MCC via the SERCOS interface. All three computers are synchronized, and allow smooth start-up and shutdown of the paddles. They also monitor the wave generator's behavior. The software utilized to compute the wave signal is GEDAP, developed by the Canadian Hydraulics Centre (CHC). The user enters the wave properties into GEDAP, which then creates a set point file. LIMITING software is then used to ensure the system's operational limits are not exceeded. The set point file is then sent to the master Control Computer, which then distributes the set points locally and to the slave computers. The set point file contains a time series for both the paddle position and the water level at the paddle.

Finally, this wavemaker is capable of generating various waves such as regular long-crested waves, irregular long-crested waves, and short-crested waves in perpendicular and oblique directions. The ARA control loop is executed in an industrial PC running Linux, and a program called Pandora which is a real-time control software developed by Bosch Rexroth; no special hardware is used.

3.3.2 Data Acquisition Equipment Description

For the tests conducted a data acquisition (DAQ) system was employed using two laptop computers that contain software exclusively developed for working in LabVIEW™ that allow measurement and recording of data in the wave basin. Both computers are equipped with DAQ cards (National Instruments) that allow measurement from up to 8 channels each. The DAQ cards and computers obtain their input from 2 types of wave gages, which are either 8 wireless capacitance-type wave gages, or 4 resistance-type wave gages.

Calibration of the wave gages is performed once per week for the wireless gages and every day when experiments are conducted in the case of the resistance gages. Their response is linear and only changes in temperature, and salinity may influence their performance, however this situation is not common. The calibration procedure is conducted with the software, in the DAQ computers, that setup and trigger an automatic displacement calibrator. The automatic displacement calibrator is connected to only one computer from which trigger signals travel to calibrator and the other computer, so all wave gages can be calibrated at the same time. Also the selected computer can trigger the DAQ measurements for all installed wave gages and any other sensors connected to other computers at once. The equipment just described is employed to measure the wave field inside the basin, with a frequency of sampling of up to 250 Hz.

Additional data from the wave field measured in front of the paddles as well as signals from the wavemakers ARA loop were obtained employing the data logger

available in the Pandora software. These signals can be recorded with a sampling rate of up to 250 Hz which is also the sampling rate used by the control system to communicate. Other equipment used for our testing included, one 3D Vectrino ADV (Acoustic Doppler Velocimeter), and two video cameras. The ADV has its own proprietary software for DAQ, and the data recorded can be used directly in any Windows based software.

3.3.3 Practical Performance from 2D Model Tests

A series of experiments were considered using reflected waves to test the three dimensional ARA system, for the wavemaker at the Haynes Coastal Engineering Laboratory. The setup consisted in placing a concrete wall on the south side of the 3D basin to create a closed area of about 9 m wide and 27 m long, that covered 19 paddles of the wave maker. The intention here was to guide waves to a reflector wall located at the end of this closed area and then having reflected waves coming back to the wave generator. The reflector wall was placed parallel with respect to the intended direction of wave travel to form an incident wave angle of 0 degrees (non-directional action, 2D). A general view of the wave tank and the position of the wireless gages can be seen in Fig. 8, where the setup for these tests is shown in detail.

The first part of the tests consisted of using the configuration mentioned above for one wave height H= 0.07 m, three wave periods T= 1.0, 1.5 and 2.0 sec, and water level d= 0.40 m, with the basin closed. The second phase repeated the same wave

conditions but this time with the basin opened, leaving the rock beach exposed to absorb the waves.

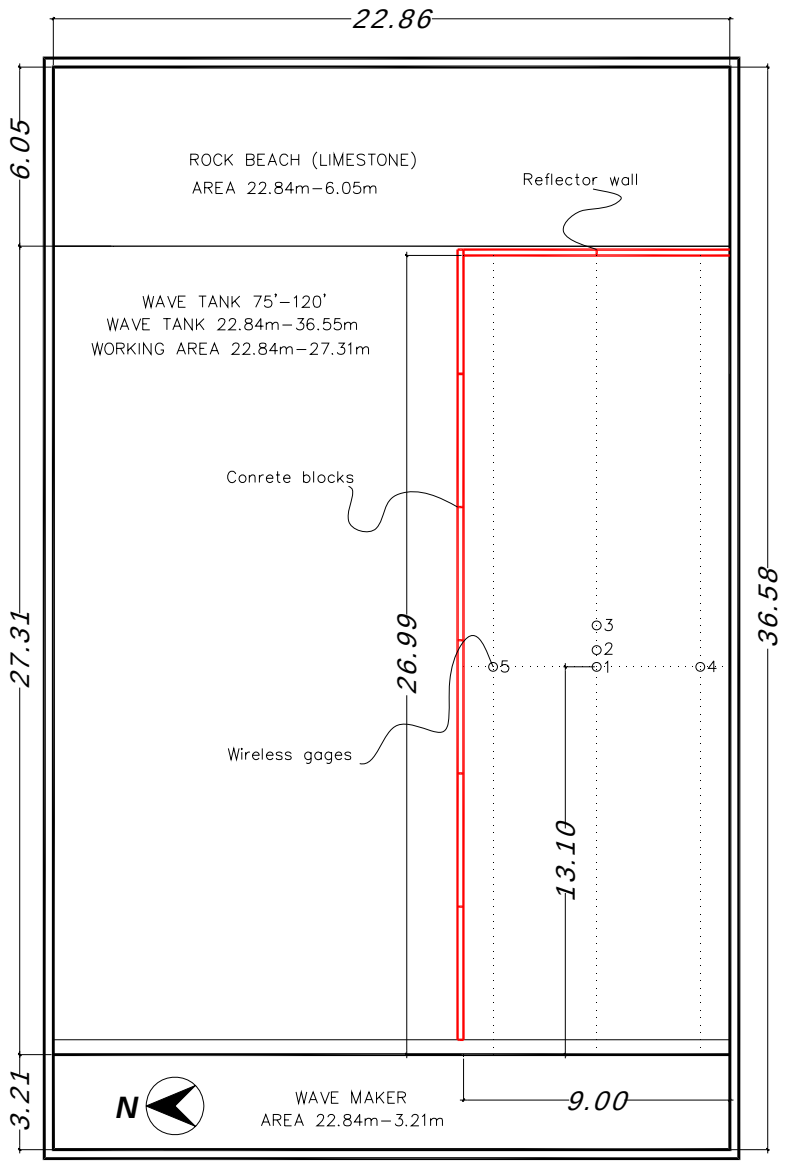

Fig. 8. General View of the ARA Test, 2D Setup

For all of these tests the waves were monochromatic with a wave incident angle of 0 degrees, the 3D ARA mode was activated with local and overall ARA gain factors of “1” (100%), and also without ARA to make comparisons. The filters used in the Pandora control software for the 3D ARA mode, were designed earlier by Bosch-Rexroth based on initial tests of the frequency response analysis of the paddles. The 3D ARA signal distribution for the experiments was with Left= 25%, Center= 50%, and Right= 25%.

A burst mode generation of waves for the closed cases for each of the three wave periods was used in order to get an easy separation of the incident, reflected and re-reflected waves, from the wave time series, although here generation and absorption of waves is not performed at the same time. Therefore, a continuous mode generation of waves was also employed to be able to see how the generation and absorption of waves was performing simultaneously.

A total of five wireless capacitance type wave gages were employed to measure the wave field inside the basin as shown in Fig. 8. Along the center line, an array of three wave gages were placed to measure the water surface elevation and the wave reflection coming from the end wall, for the continuous wave mode. The array was setup to calculate the incident and reflected wave traces at the position of gage 1, which is located 13.10 m away from the wavemaker front at still position. The separation of the wave gages is defined according to the recommendations of Mansard and Funke (1980) for the array located in the middle of the basin. The separation of incident and reflected waves was conducted with a program in GEDAP denominated REFLS.

A total of 12 tests were made for the conditions indicated in Table 1. Tests 1 to 3 were made with ARA, and tests 4 to 6 without ARA, in order to make a comparison of the effectiveness of the ARA absorption in the closed basin condition with wave burst mode. Tests 7 to 12 for the opened and closed basin cases were made to assess the behavior of the ARA for continuous wave generation and absorption.

Table 1. Test matrix configuration for ARA experiments, 2D model monochromatic waves (0 degrees)

H (m)	d (m)	Test	T (sec)	ARA condition	Wave Generation Mode	Basin Condition
0.07	0.40	1	1.00	100% 3D ARA mode	burst	closed
		2	1.50			
		3	2.00			
0.07	0.40	4	1.00	NO ARA	burst	closed
		5	1.50			
		6	2.00			
0.07	0.40	7	1.00	100% 3D ARA mode	continuous	closed
		8	1.50			
		9	2.00			
0.07	0.40	10	1.00	100% 3D ARA mode	continuous	opened
		11	1.50			
		12	2.00			

3.3.4 Practical Performance from 3D Model Tests

Similar tests to those conducted for the 2D model, were made for three dimensional waves. Twelve tests for both, continuous and burst wave mode were developed to measure the performance of the 3D ARA mode with a 3D setup. The setup consisted in placing 14 concrete blocks in the basin to create a closed area of about 27.46 m long by 8.6 m wide, which covered 20 paddles of the wave maker. The end wall formed an angle of about 30 degrees with respect to the paddles of the wavemaker. Within this area, a total of five wireless capacitance type wave gages were employed to measure the wave field inside the basin, from which along the center line, an array of three wave gages was placed to measure water surface elevation and wave reflection, for the position of gage 1 which is located at about 13.46 m from the wavemaker front. A detailed view of the setup is illustrated in Fig. 9.

This configuration was used for a combination of wave height H=0.07 m, T= 1.00, 1.50 and 2.00 sec and d= 0.40 m, with the basin closed and later opened for the continuous mode. The waves were monochromatic with a wave incident angle of 30 degrees, the 3D ARA was activated with local and overall ARA gain factors of “1” (100%), and also without ARA, for the burst mode. The conditions described are summarized in Table 2. Tests 1 to 3 were made with ARA, and tests 4 to 6 without ARA, in order to make a comparison of the effectiveness of the ARA absorption in the closed basin condition with wave burst mode. Tests 7 to 12 for the opened and closed

basin cases were made to assess the behavior of the ARA for continuous wave generation and absorption.

The filters used in the Pandora control software for the 3D ARA, were designed based on initial tests of the frequency response analysis of the paddles. The 3D ARA mode signal distribution for the experiments was with Left= 25%, Center= 50%, and Right= 25%.

Table 2. Test matrix configuration for ARA experiments, 3D model monochromatic waves (30 degrees)

H (m)	d (m)	Test	T (sec)	ARA condition	Wave Generation Mode	Basin Condition
0.07	0.40	1	1.00	100% 3D ARA mode	burst	closed
		2	1.50			
		3	2.00			
0.07	0.40	4	1.00	NO ARA	burst	closed
		5	1.50			
		6	2.00			
0.07	0.40	7	1.00	100% 3D ARA mode	continuous	closed
		8	1.50			
		9	2.00			
0.07	0.40	10	1.00	100% 3D ARA mode	continuous	opened
		11	1.50			
		12	2.00			

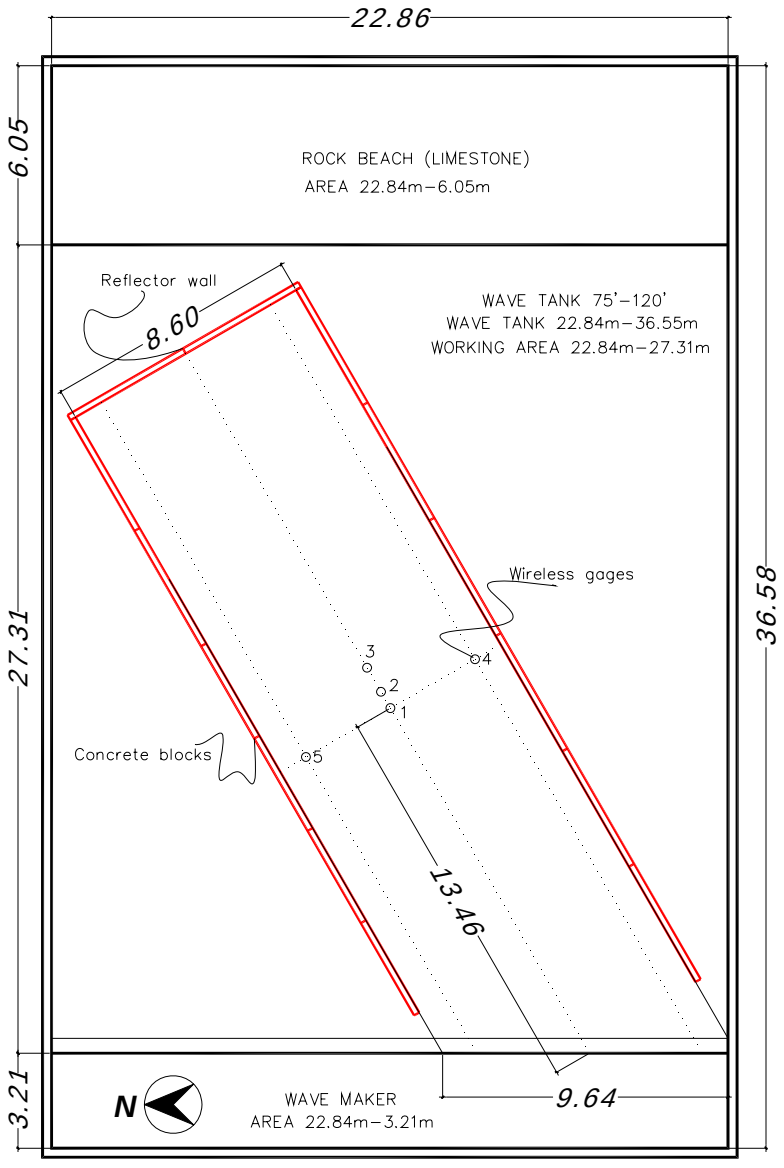

Fig. 9. General View of the ARA Test, 3D Setup

3.3.5 Practical Performance from 2D Model Tests, Using the Whole Wavemaker

Twenty four tests were considered in order to evaluate the performance of 3D ARA mode for the entirety of the wave maker. Here the methodology followed is the same as that described previously for section 3.3.3 where tests in burst and continuous mode, with and without ARA, and with open and closed basin, were conducted. The difference comes only in the setup and the inclusion of tests for a new short wave filter, to evaluate if better stability was achieved. The purpose was to allow for comparison with previous measurements of the original filter with the previous 2D setup, in order to corroborate the results obtained, and also to compare with the new filter. A summary of the testing conditions is presented in Table 3 and Table 4, and a detailed view of the experimental setup is shown in Fig. 10, for the burst mode, and Fig. 11 for the continuous mode. Wave gages 1 thru 3 had different positions as can be observed in Fig. 10 and Fig. 11, this was due to for the continuous mode the array had to be located in a line perpendicular to the waves in order to separate incident a reflected waves.

Table 3. Test matrix configuration for ARA experiments, 2D model, whole wavemaker, monochromatic waves (0 degrees), burst mode

H (m)	d (m)	Test	T (sec)	ARA condition	Wave Generation Mode	Basin Condition
0.07	0.40	1	1.00	100% 3D ARA mode original SWF Filter	burst	closed
		2	1.50			
		3	2.00			
0.07	0.40	4	1.00	100% 3D ARA New SWF Filter	burst	closed
		5	1.50			
		6	2.00			
0.07	0.40	7	1.00	NO ARA	burst	closed
		8	1.50			
		9	2.00			

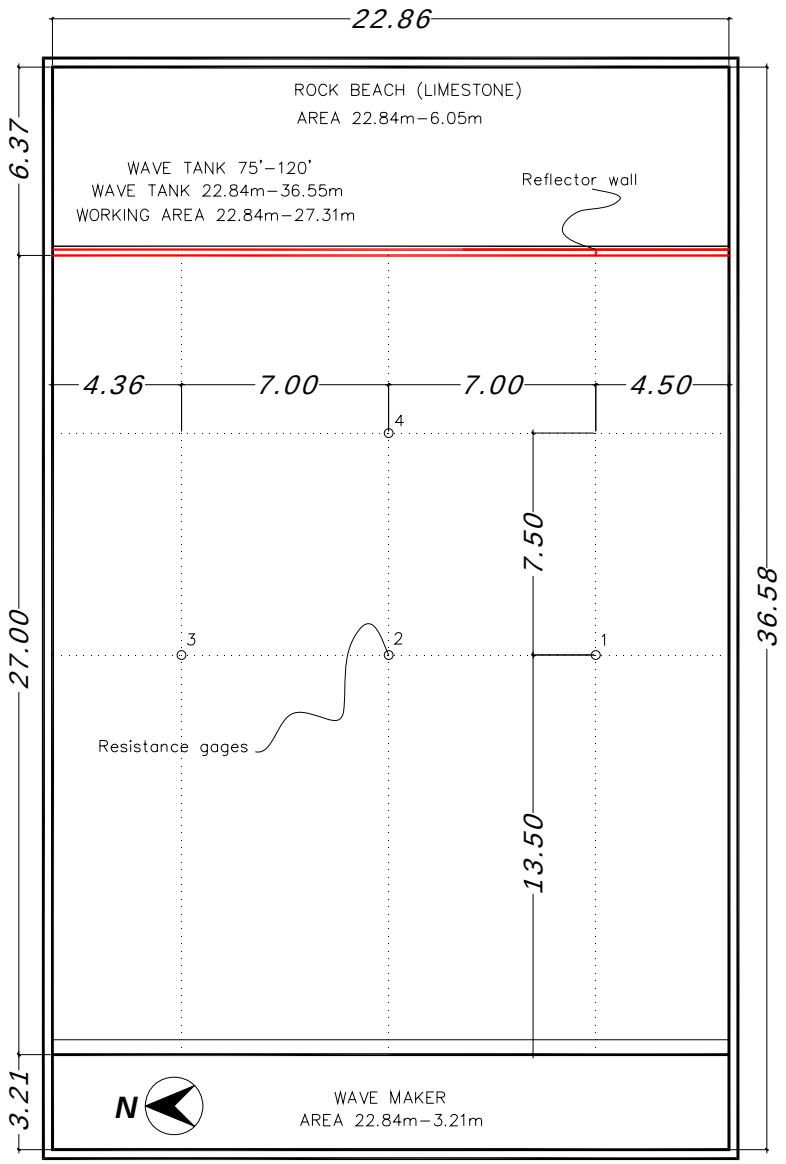

Fig. 10. General View of the ARA Test, 2D Setup, Whole Wavemaker, Burst Mode

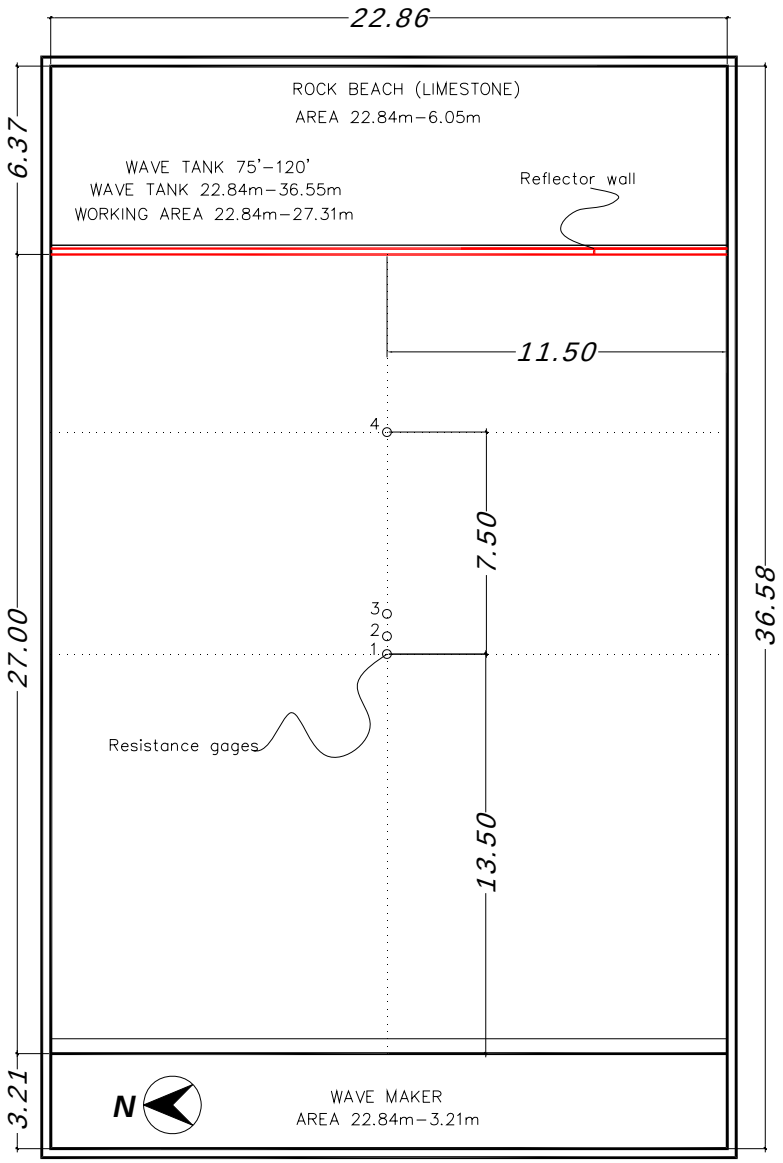

Fig. 11. General View of the ARA Test, 2D Setup, Whole Wavemaker, Continuous Mode

Table 4. Test matrix configuration for ARA experiments, 2D model, whole wavemaker, monochromatic waves (0 degrees) continuous mode

H (m)	d (m)	Test	T (sec)	ARA condition	Wave Generation Mode	Basin Condition
0.07	0.40	10	1.00	100% 3D ARA mode, original SWF Filter	continuous	closed
		11	1.50			
		12	2.00			
0.07	0.40	13	1.00	100% 3D ARA mode, new SWF Filter	continuous	closed
		14	1.50			
		15	2.00			
0.07	0.40	16	1.00	100% 3D ARA mode, original SWF Filter	continuous	open
		17	1.50			
		18	2.00			
0.07	0.40	19	1.00	100% 3D ARA mode, New SWF Filter	continuous	open
		20	1.50			
		21	2.00			
0.07	0.40	22	1.00	NO ARA	continuous	open
		23	1.50			
		24	2.00			

3.4 Program Development for DOA Detection and Validation with Measured Data

A codification of the algorithm for DOA presented in section 2.5.2 was accomplished in Matlab™, where several built-in functions were used; the actual program code is presented in Appendix A. The program follows the theory presented before and it was originally tested with synthetic data (monochromatic waves, following linear wave theory), assuming a linear array of sensors with a separation of 0.48 m. Up to 11 sensors were used to calculate the DOA of the tested signal. After this preliminary

test it was decided to use data gathered from the wave basin, this was accomplished in two phases, which are described in the following sections.

3.4.1 Preliminary Tests for Validation of DOA Program with Measured Data

The first phase to validate the DOA program consisted in gathering data from the wave basin by placing a linear array of wave gages as indicated in Fig. 12. Here a combination of four resistance and seven wireless gages were employed to obtain a linear array with a separation among sensors of 0.48 m. This array was switched in position in order to change the angle that the array formed with respect to the front of the wavemaker. The idea was to generate orthogonal waves (0 degree angle) for all cases and by changing the position of the gages achieved different angles of incidence arriving to the array. The array was moved to form angles of 0, 10, 20, 30 and 40 degrees, with respect to the wavemaker front.

The wave conditions tested consisted of a series of tests for regular waves, using the entirety of the wave maker. The regular waves had a combination of one wave height H= 0.06 m, with three different wave periods, T= 1 sec, 1.5 sec and 1.8 sec, with a water depth of d= 0.30 m. The waves mentioned above were run every time that the array was switched in position. Table 5 summarizes the tests conducted. Analysis of the data gathered and the use of the DOA program are discussed in the next chapter.

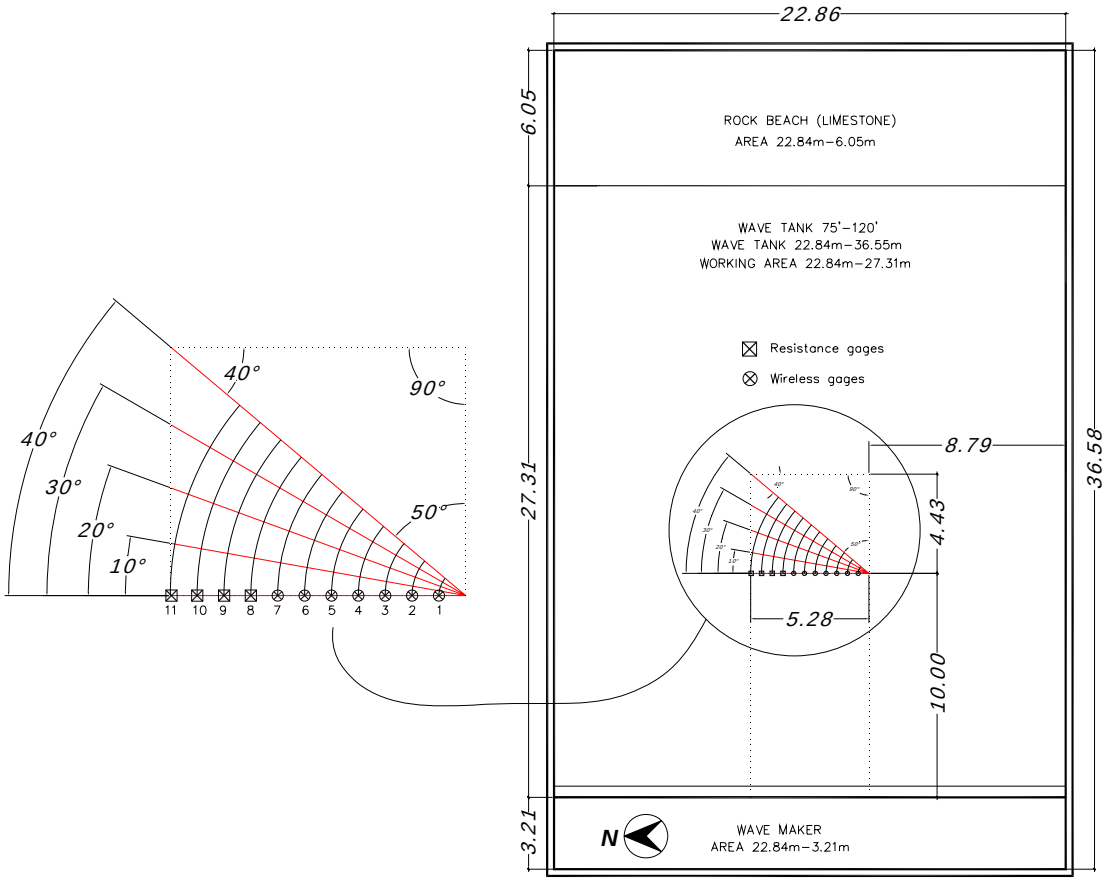

Fig. 12. General View for Tests to Obtain Data for DOA Program

Table 5. Test matrix configuration for tests to obtain data for DOA program, monochromatic waves (0 degrees)

H (m)	d (m)	Test	T (sec)	Array angle condition	Wave Generation angle	Basin Condition
0.06	0.30	1	1.00	0 degrees	0 degrees	open
		2	1.50			
		3	1.80			
0.06	0.30	4	1.00	10 degrees	0 degrees	open
		5	1.50			
		6	1.80			
0.06	0.30	7	1.00	20 degrees	0 degrees	open
		8	1.50			
		9	1.80			
0.06	0.30	10	1.00	30 degrees	0 degrees	open
		11	1.50			
		12	1.80			
0.06	0.30	13	1.00	40 degrees	0 degrees	open
		14	1.50			
		15	1.80			

3.4.2 2D and 3D Model Tests for Validation of DOA Program with Data Obtained from the Control System of TAMU Wavemaker

A series of tests with the same wave conditions as those described in section 3.3.3 and 3.3.4, but with a slightly different setup were conducted this time to record several signals from the control system software of the wavemaker. Fig. 13 and Fig. 14 show the setup for the 2D model and 3D model tests respectively. Table 6 and Table 7 summarize the wave conditions. The data recorded was obtained in order to use it in the DOA program. The DOA program was modified to adapt it for working with actual data obtained to use the position of the paddles and the water level error from the 2D ARA loop as inputs. Also a total of 65 signals per paddle were obtained from the ARA loop were recorded (from paddle 1 to paddle 32), with a sampling rate of 250 Hz, these signals were used to feed a program developed in Simulink^{TM} to reproduce the calculation of the paddle correction of our system. This was done in order to allow comparison between the 3D ARA loop using the spatial gain-mixer, and the use of only the 2D ARA loop with our DOA program.

The comparison can be performed in only a small part (about 20 sec) of the data recorded for the continuous mode due to the feedback nature of the system, which depends of course on the correction calculated. This is also the case for the burst mode. Nonetheless, as already discussed in Chapter I by calculating effectively the DOA of reflected waves, the displacement correction calculated at the paddle front only needs to be reduced by a factor of $\cos\theta$, where θ is the DOA of the reflected wave in real time. In

our case we already know what the angle should be from our setup. Therefore we can evaluate how the DOA program performs from these tests with actual measurements from our system.

Table 6. Test matrix configuration for ARA experiments, 2D model monochromatic waves (0 degrees)

H (m)	d (m)	Test	T (sec)	ARA condition	Wave Generation Mode	Basin Condition
0.07	0.40	1	1.00	100% 3D ARA mode New SWF	burst	closed
		2	1.50			
		3	2.00			
0.07	0.40	4	1.00	NO ARA	burst	closed
		5	1.50			
		6	2.00			
0.07	0.40	7	1.00	100% 3D ARA mode New SWF	continuous	closed
		8	1.50			
		9	2.00			
0.07	0.40	10	1.00	NO ARA	continuous	closed
		11	1.50			
		12	2.00			

Table 7. Test matrix configuration for ARA experiments, 3D model monochromatic waves (30 degrees)

H (m)	d (m)	Test	T (sec)	ARA condition	Wave Generation Mode	Basin Condition
0.07	0.40	1	1.00	100% 3D ARA mode New SWF	burst	closed
		2	1.50			
		3	2.00			
0.07	0.40	4	1.00	NO ARA	burst	closed
		5	1.50			
		6	2.00			
0.07	0.40	7	1.00	100% 3D ARA mode New SWF	continuous	closed
		8	1.50			
		9	2.00			
0.07	0.40	10	1.00	NO ARA	continuous	closed
		11	1.50			
		12	2.00			

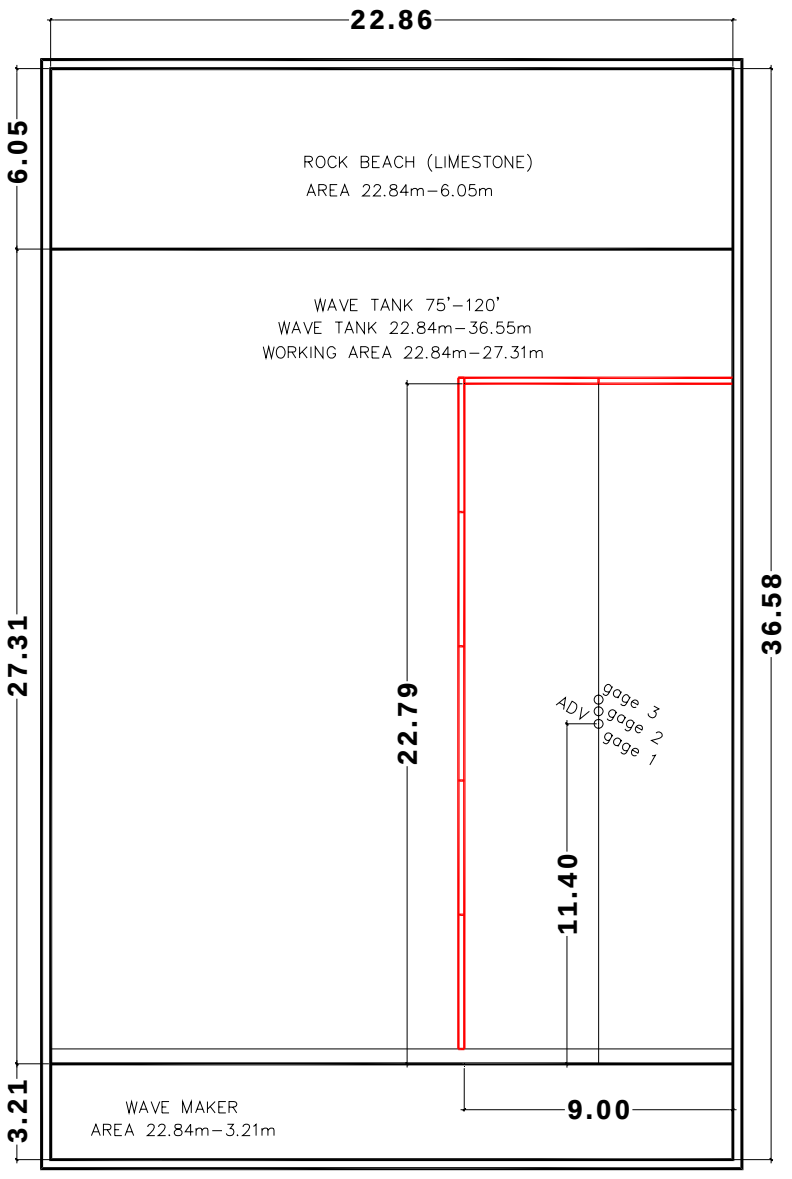

Fig. 13. General View of the ARA Test, 2D Setup

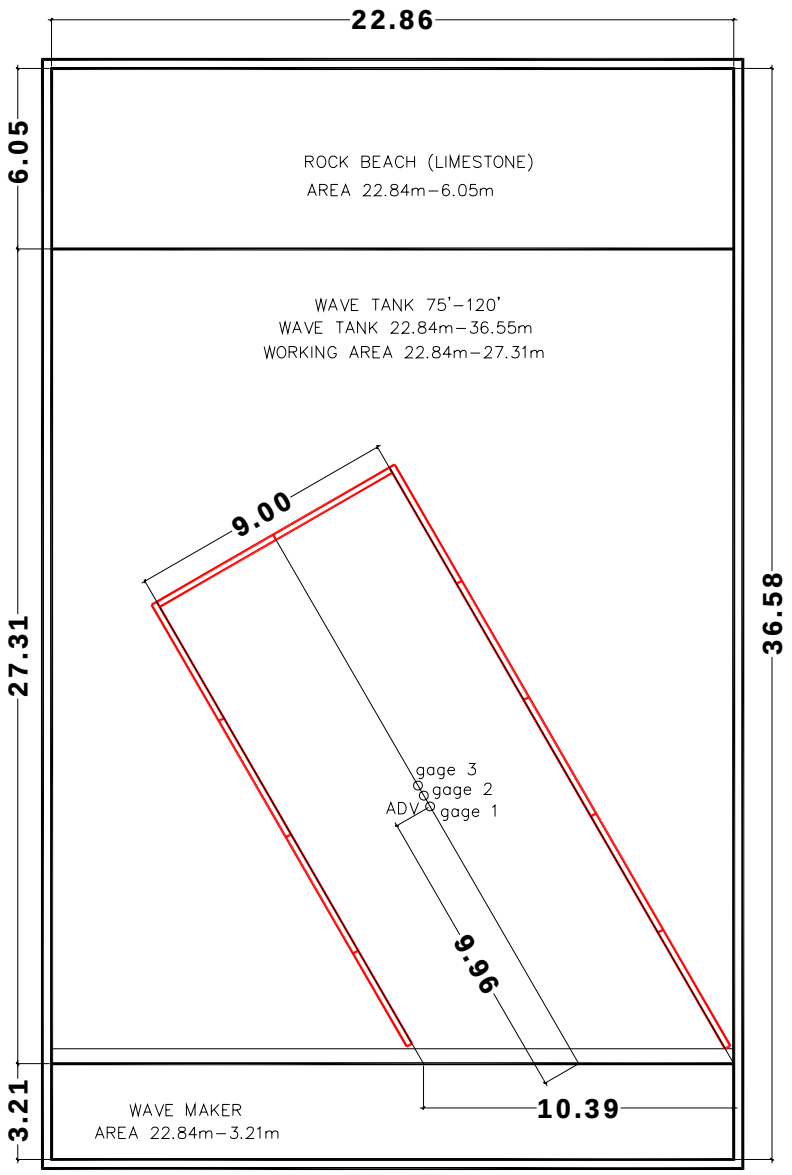

Fig. 14. General View of the ARA Test, 3D Setup

CHAPTER IV

ANALYSIS OF RESULTS

4.1 Introduction

This chapter presents the analysis of results of the physical tests and the analysis of the program for DOA. The order of this chapter follows that of the previous chapter for clarity. When needed most of the results will be presented and discussed in this chapter. Information obtained that is repetitive will be made available in the Appendix section.

4.2 Results of the Evaluation of the ARA Loop as Implemented by Bosch-Rexroth

Basically two filters are involved in the performance of our ARA loop; both were designed by Bosch-Rexroth using the Filter Design Toolbox™ available on Matlab™. One is the LWF (long wave filter), which is a first order IIR digital high-pass filter, and the second one is a SWF (short wave filter), which is a second order IIR digital low-pass filter. The LWF has a normalized cutoff frequency of $\omega_n = 0.01/250$, and the SWF one of $\omega_n = 2/250$. Bode plots of the filters and some of their characteristics are shown in Fig. 15 for the LWF and in Fig. 16 for the SWF.

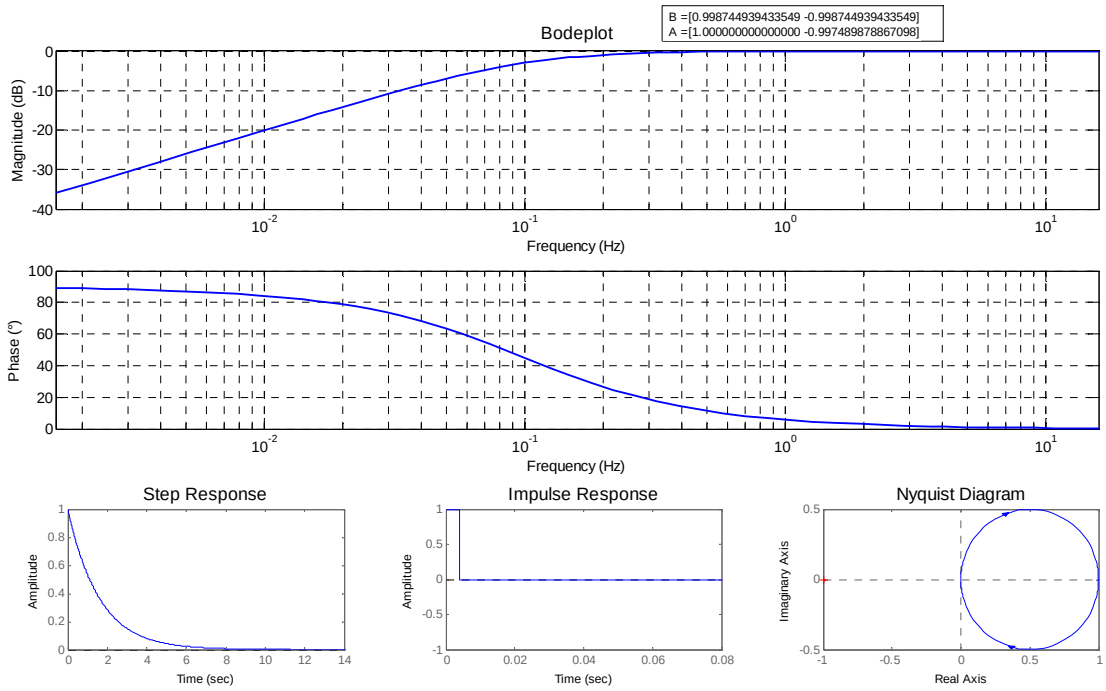

Fig. 15. LWF Designed by Rexroth, Bode Plot, Step Response, Impulse Response and Nyquist Diagram

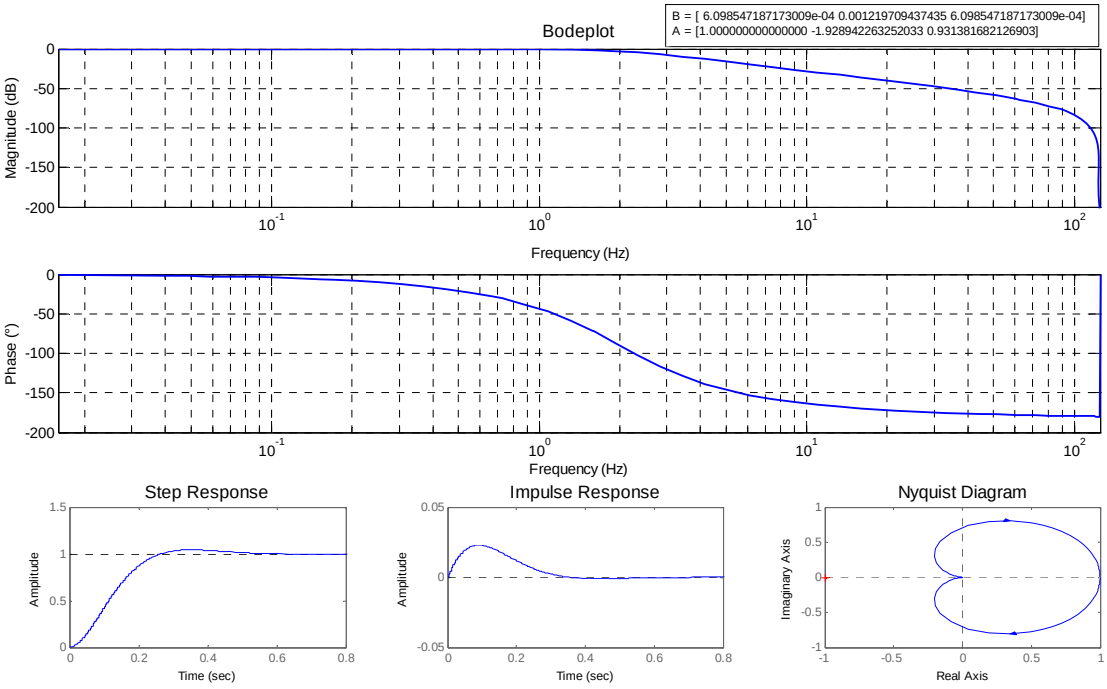

Fig. 16. SWF Designed by Rexroth, Bode Plot, Step Response, Impulse Response and Nyquist Diagram

These filters are stable and were entered into the ARA loop as a transfer function in the z-domain as coefficients of the numerator [B] and coefficients of the denominator [A]. In order to evaluate the influence of the SWF and the stability of the ARA loop several frequency response analyses were made using the FRA analyzer. The conditions were with and without the SWF, and for open and closed loop, where the loop is open when the value of alpha is 0, and is closed when alpha is 1. Alpha corresponds to the ARA gain which is a coefficient that regulates the influence of the ARA in the system. The signals employed correspond to the ARA input (setpoint position) and the output signal CSWPosCorr (see Fig. 3 for reference). Fig. 17 shows a FRA for paddle 45, with h =0.50 m, for the open loop case. Fig. 18 shows the same data for paddle 45 but for the closed loop case.

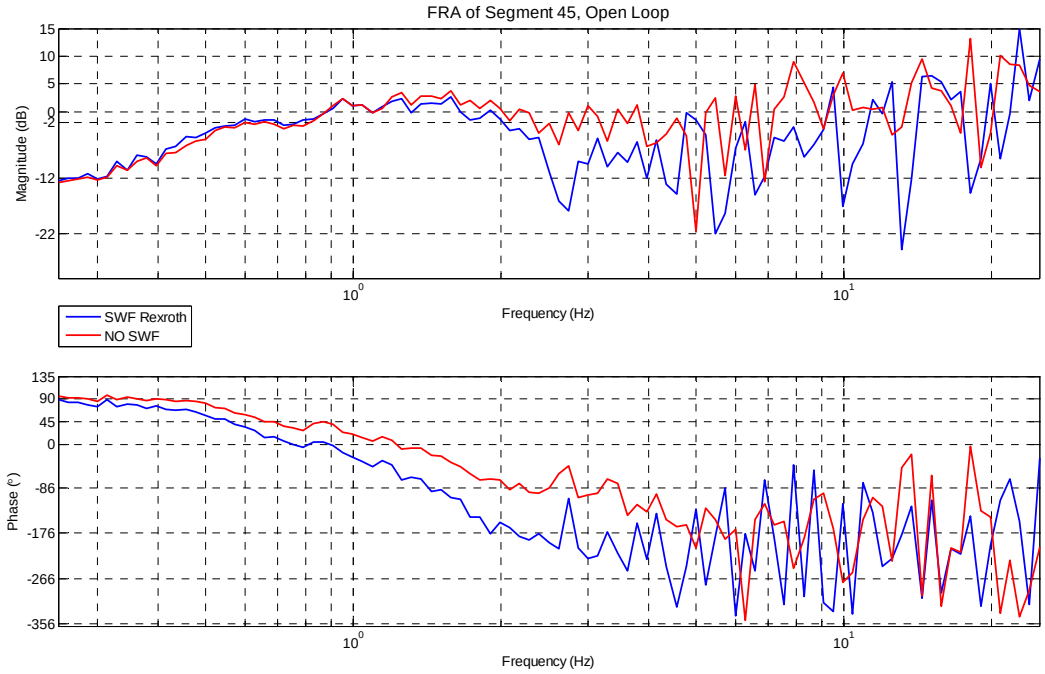

Fig. 17. FRA for Paddle 45, h=0.50 m, Open Loop, Alpha = 0, with and without SWF from Rexroth

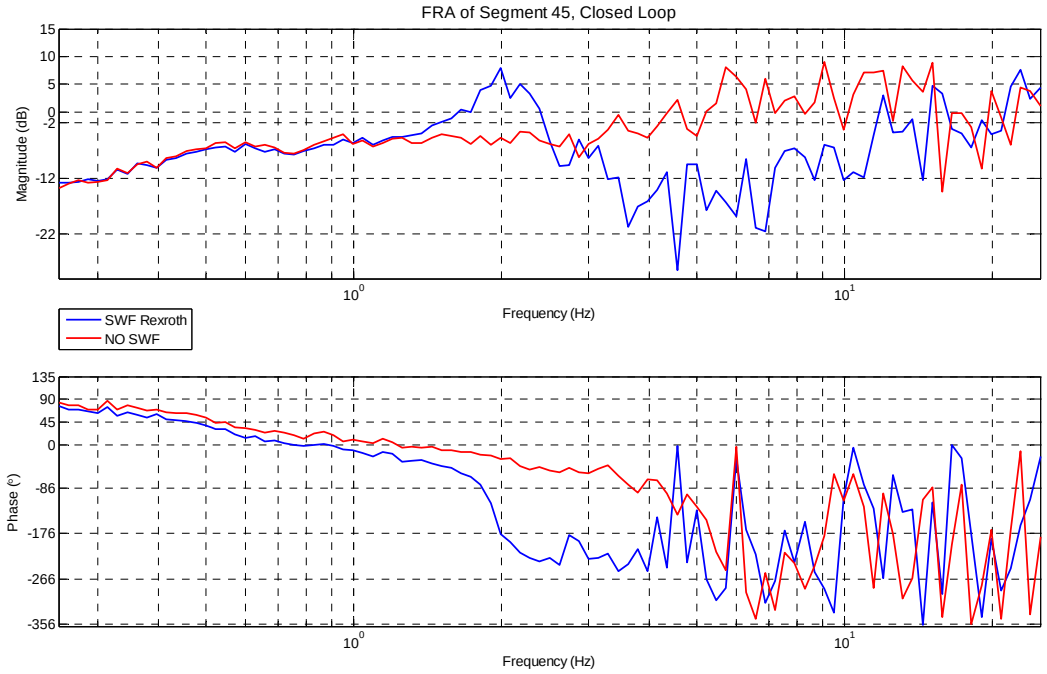

Fig. 18. FRA for Paddle 45, h=0.50 m, Closed Loop, Alpha = 1, with and without SWF from Rexroth

In the previous figures it can be observed that for both loop conditions (open and closed) the response goes wild after 4 Hz. From Fig. 18 (closed loop) it can be seen that at about 2 Hz the SWF filter has a peak that indicates an instability that was confirmed later with preliminary physical tests (for qualitative purposes) with a setup as that indicated in section 3.3.5. Here the paddles showed resonance at about this frequency, with 2D ARA mode active, during and after waves were stopped in the burst mode, when a series of trailing waves arrived to the paddles (especially for T= 1.00 sec). A more severe behavior was observed in the continuous mode which indicates that 2D ARA mode is not workable since it cannot control oscillations of the paddles when high frequency waves appear. A much less severe situation occurred for the 3D ARA mode,

where the resonance is effectively reduced due to the spatial-gain mixer, which allows the use of ARA.

In order to evaluate the stability of the ARA system Nyquist plots were obtained and shown in Fig. 18 for the No SWF case in open and closed loop and the SWF from Rexroth also in open and closed loop. From Fig. 19 it is confirmed the instability observed for the SWF from Rexroth (closed loop), where the points exceeding -1 along the real axis correspond to the peak indicated before around 2 Hz. The response of the system is affected at high frequencies which are most of the points exceeding -1 for the open and closed loop without SWF, where the system is unstable after about 4 Hz.

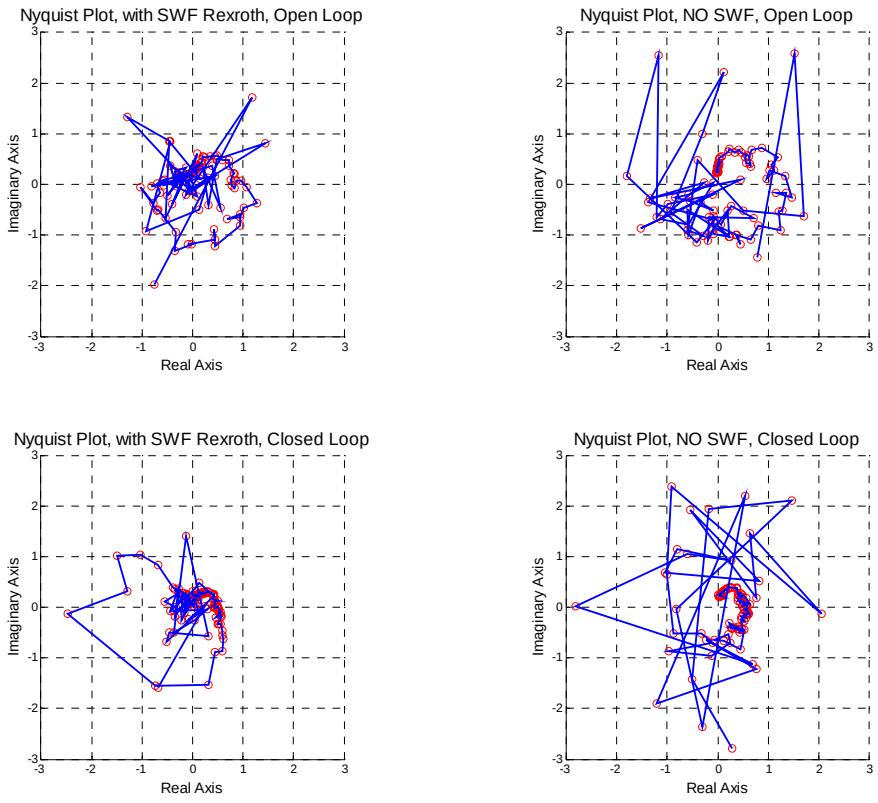

Fig. 19. Nyquist Plots for Closed and Open Loop, with and without SWF from Rexroth

Due to the situation just described it was decided to design a filter that removed the instability at 2Hz. A program developed in Matlab™ was provided by Rexroth to design a lead-lag compensator filter, which used as a base a first order Butterworth filter with cutoff frequency of $\omega_n = 2/250$. A Bode plot of this filter and some of its characteristics are shown in Fig. 20.

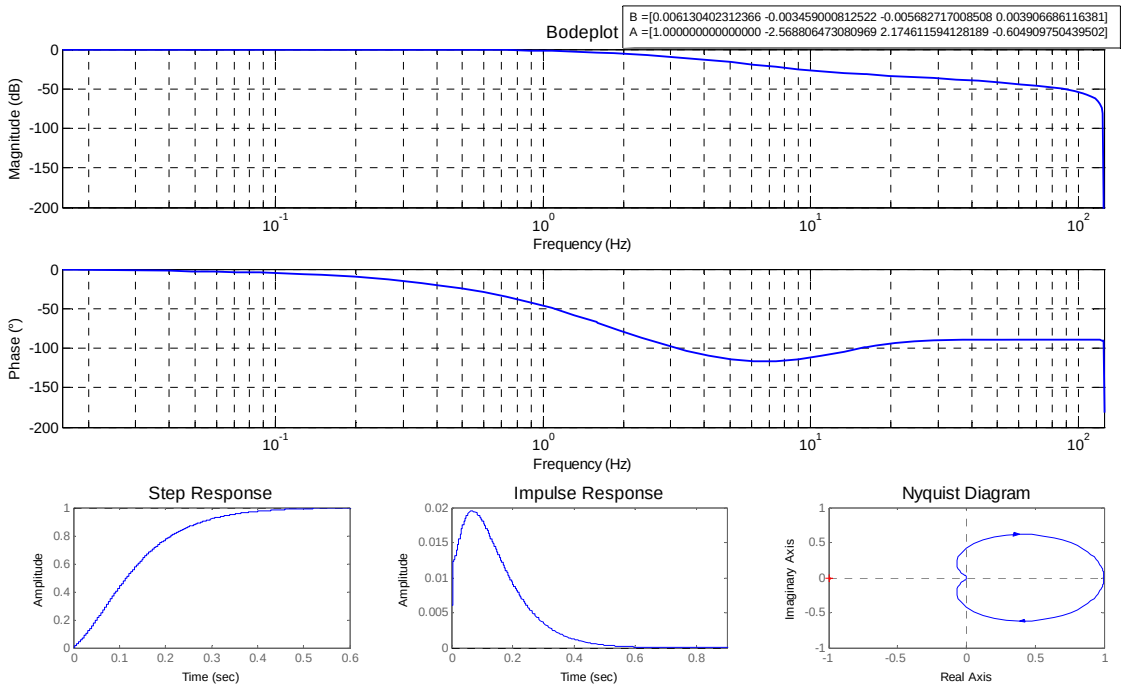

Fig. 20. New SWF with Lead-Lag Compensator, Bode Plot, Step Response, Impulse Response and Nyquist Diagram

The filter is stable and FRA's were done for the same conditions as for the SWF from Rexroth, using the same input signals. Fig. 21 shows a FRA for paddle 45, with h =0.50 m, for the open loop case. Fig. 22 shows the same data for paddle 45 but for the closed loop case, both figures for the New SWF.

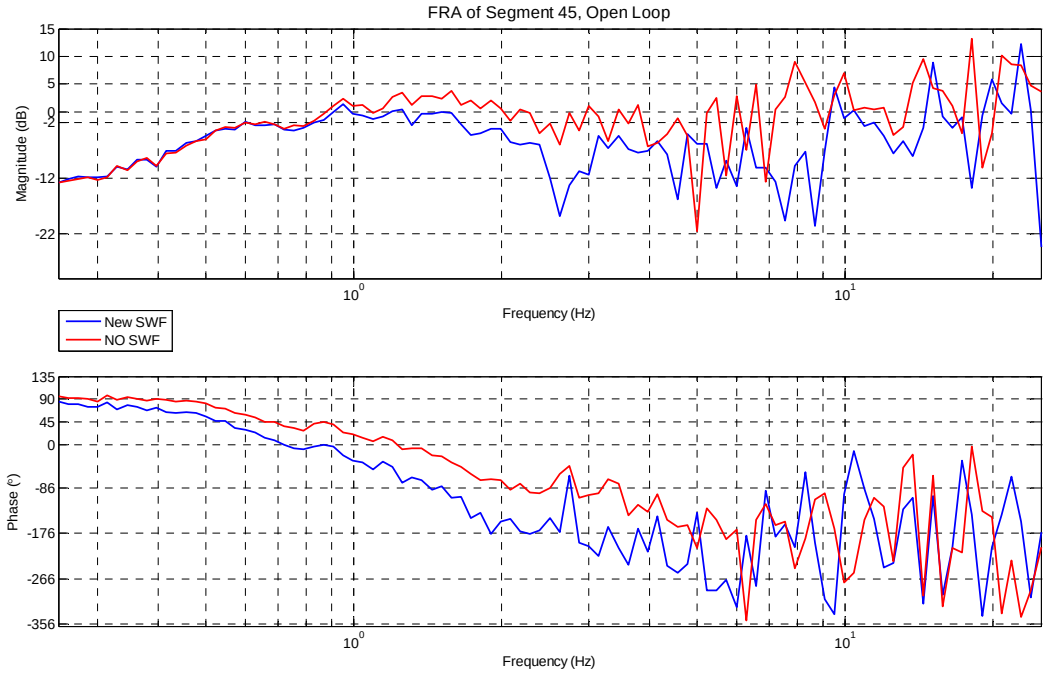

Fig. 21. FRA for Paddle 45, h=0.50 m, Open Loop, Alpha = 0, with and without New SWF

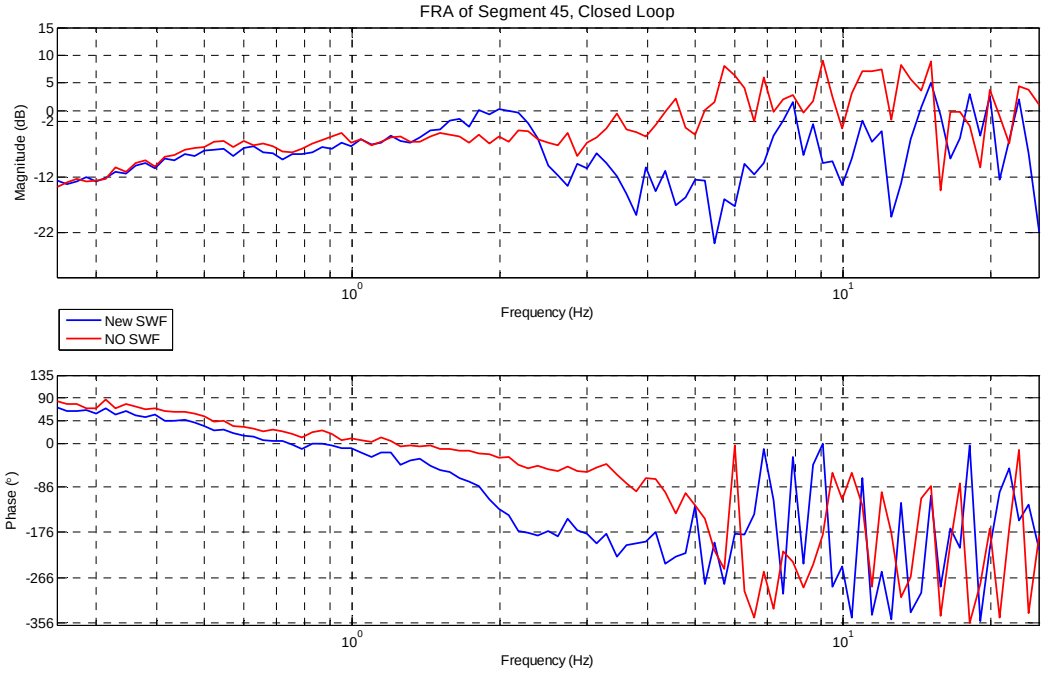

Fig. 22. FRA for Paddle 45, h=0.50 m, Closed Loop, Alpha = 1, with and without New SWF

In the previous figures it can be observed that for both loop conditions (open and closed) the response goes wild this time after about 5 Hz, but not as much as before. From Fig. 22 (closed loop) it can be seen that the peak at about 2 Hz originally present for the SWF from Rexroth has been reduced. From preliminary physical tests (for qualitative purposes) with a setup as that indicated in section 3.3.5, with a wave period of T=1.00 sec, with burst waves, it was observed that still trailing waves in the tank with high frequencies may produce an unstable system when working in 2D ARA mode, although is not as severe as observed with the SWF from Rexroth. For burst wave generation mode with wave periods of T= 1.50 sec, and 2.00 sec, the trailing waves have lower frequency, and do not affect the system as much as before. With the new SWF the only concern comes when the 2D ARA mode is left working for a long time, as the systems gets unstable.

However still a severe behavior was observed in the wave continuous mode which indicates that 2D ARA mode is still not workable with the new SWF since it cannot control oscillations of the paddles when high frequency waves appear, although it does last longer in the wave generation and absorption mode than the Rexroth SWF. A different behavior occurred for the 3D ARA mode, where the system works fine, for the wave conditions mentioned above. Here the response of the system is effectively reduced due to the spatial-gain mixer.

In order to evaluate the stability of the new SWF, Nyquist plots were obtained and are shown in Fig. 23 for the No SWF case in open and closed loop and the new SWF also in open and closed loop. From Fig. 23 it is confirmed that the instability observed

for the SWF from Rexroth (closed loop), has been removed. The response of the system is still affected at high frequencies which are most of the points near to -1 for the open and closed loop with the new SWF, where the system is unstable after about 5 Hz.

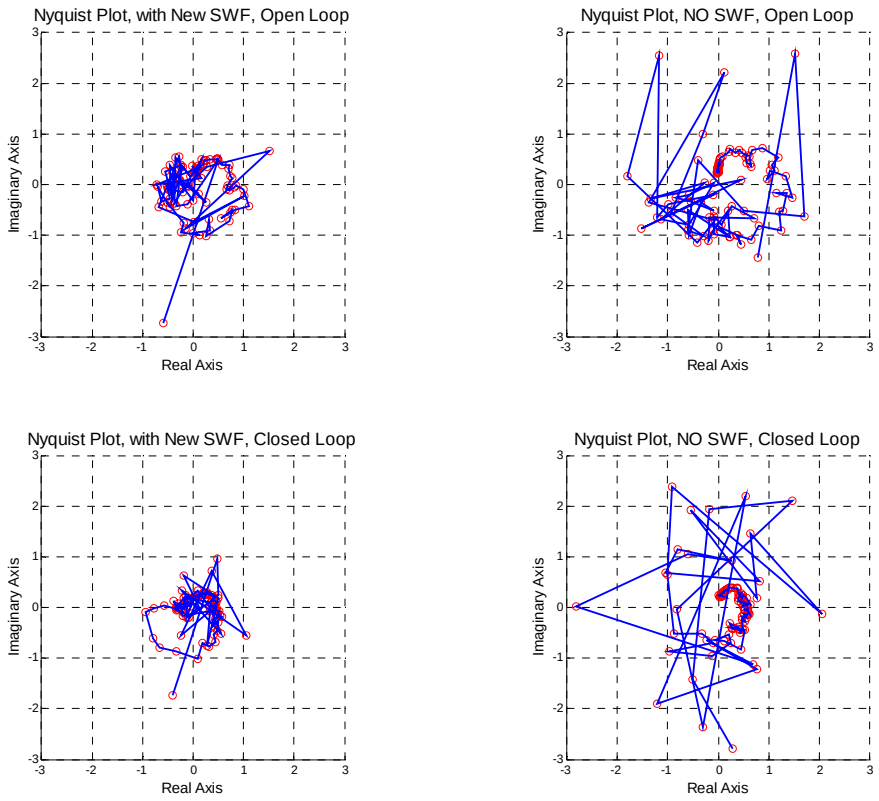

Fig. 23. Nyquist Plots for Closed and Open Loop, with and without New SWF

Due to the poor stability shown in the preliminary tests of the 2D ARA mode, it was only considered to conduct measurements with the 3D ARA mode in order to evaluate the performance of our ARA system. This situation indicates that a better tune up of the filters needs to be conducted, which is out of the scope of this research, since it

was accomplished an acceptable behavior of our system for the 3D ARA mode from preliminary test.

4.3 Results of the Estimation of the Coefficient of Re-reflection from Theory and Physical Tests

Following the theory presented in section 2.3.1, Fig. 24 shows the theoretical behavior of the ARA system with and without evanescent modes. This figure will be used in the next sections to compare the results obtained from experiments with the calculated theory for our system.

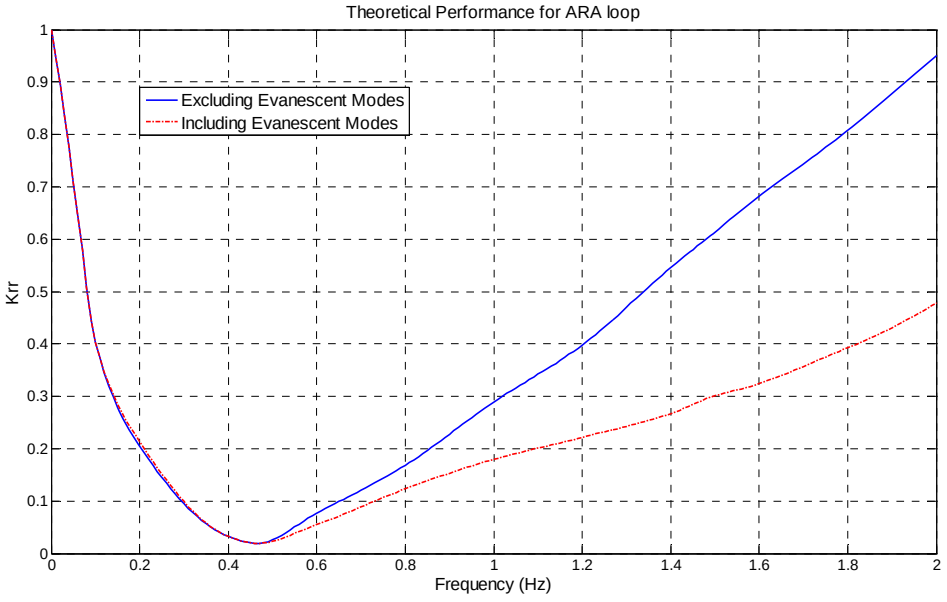

Fig. 24. Theoretical Performance for ARA Loop, for TAMU Wavemaker

4.3.1 Results from Practical Performance from 2D Model Tests

4.3.1.1 Burst Wave Mode

This section presents the results of the 2D model tests to measure the performance of the 3D ARA mode of our wavemaker as indicated in section 3.3.3. Fig. 25 through Fig. 27 show the wave traces for experiments 1 through 6 (burst mode) at the position of gage 1. Fig. 25 shows the comparison for tests 1 and 4 (T=1.0 sec), where it is shown in detail the reflected wave originated by the reflector wall, traveling towards the wave maker, as well as the re-reflected wave from the wave maker, for both conditions ARA and NO ARA. In a similar fashion Fig. 26 and Fig. 27 show the comparisons for experiments 2 and 5 (T=1.5 sec), and for 3 and 6 (T=2.0 sec), respectively.

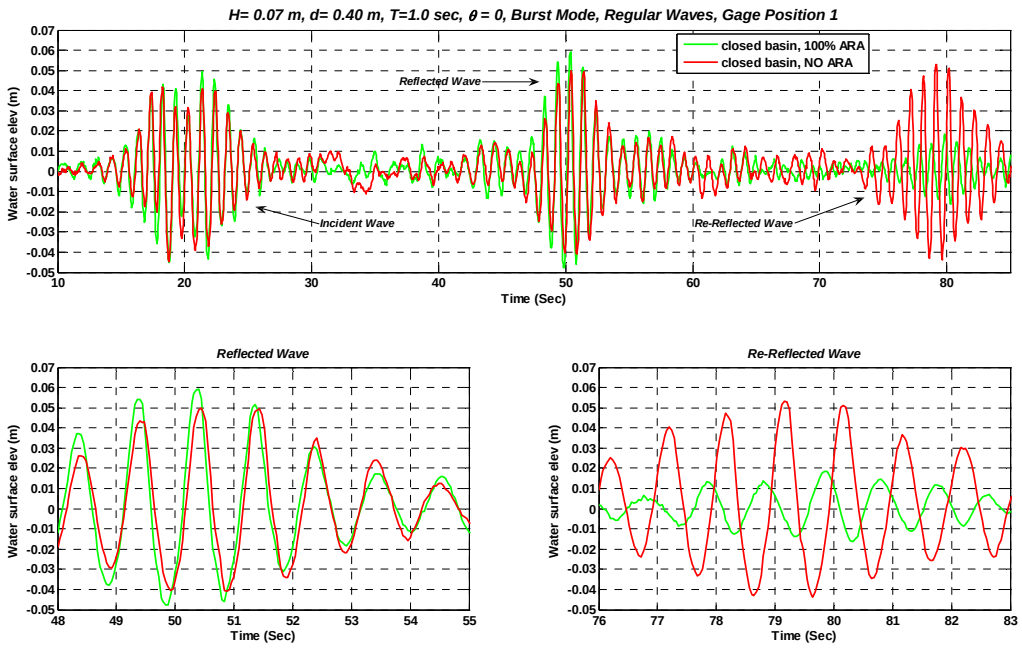

Fig. 25. Wave Traces for Experiments 1 and 4 at the Position of Gage 1, T = 1.00 sec, Burst Mode, Closed Basin, with and without ARA, 0 Degree Angle

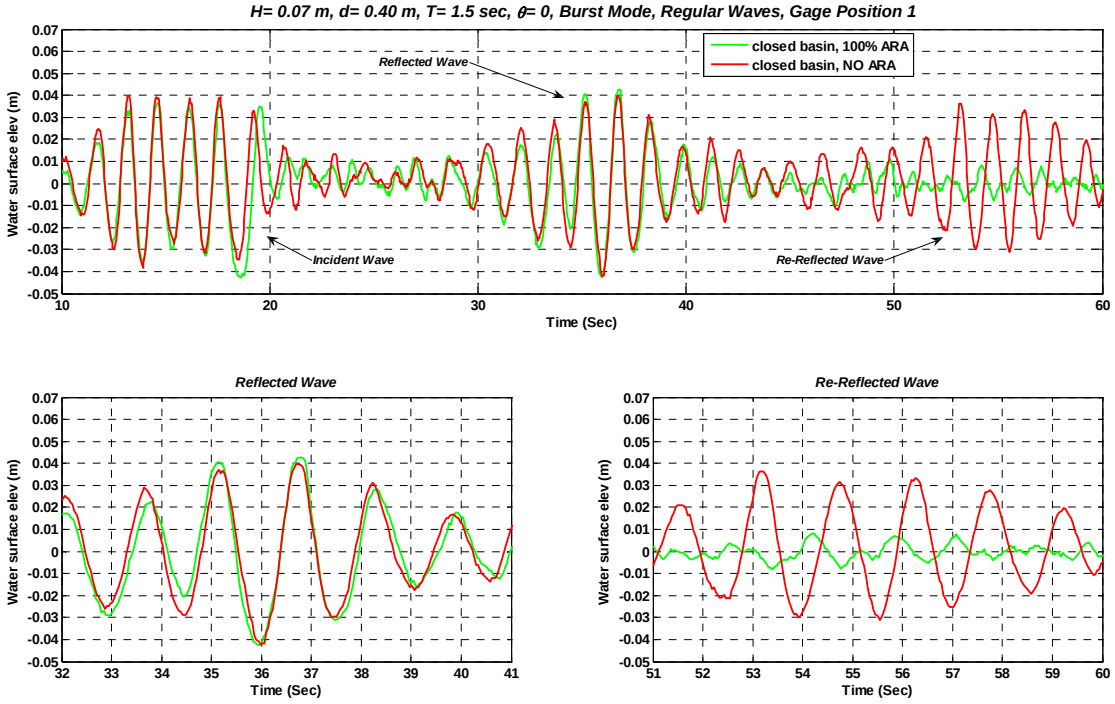

Fig. 26. Wave Traces for Experiments 2 and 5 at the Position of Gage 1, T= 1.50 sec, Burst Mode, Closed Basin, with and without ARA, 0 Degree Angle

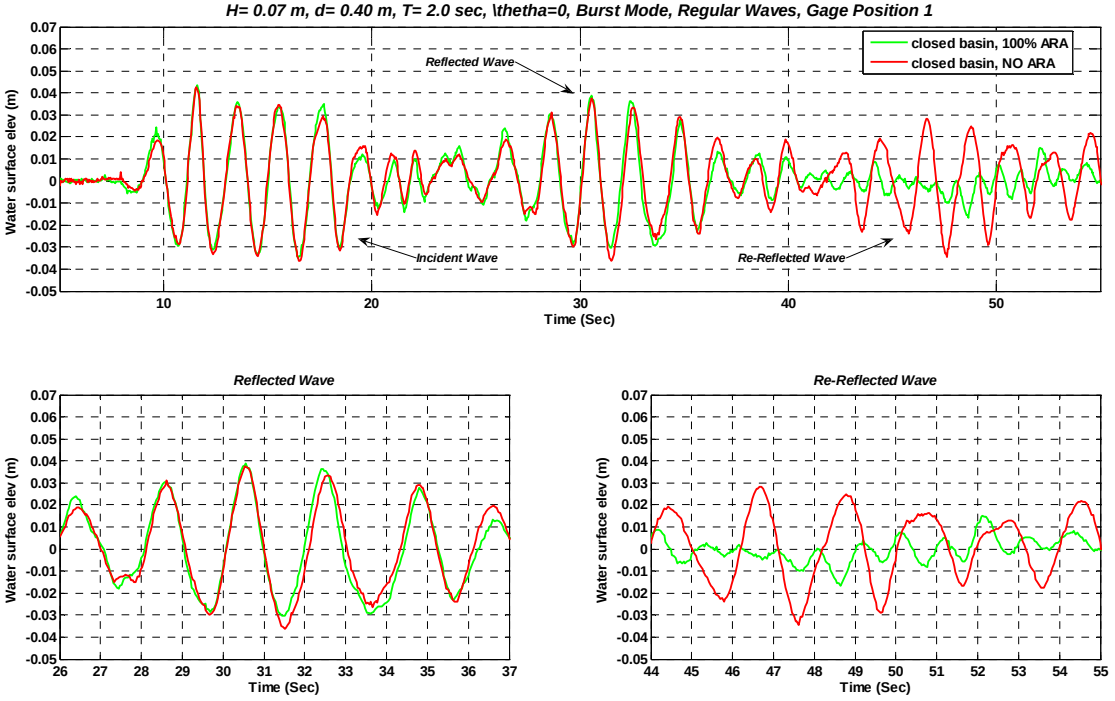

Fig. 27. Wave Traces for Experiments 3 and 6 at the Position of Gage 1, T= 2.00 sec, Burst Mode, Closed Basin, with and without ARA, 0 Degree Angle

From the figures above the reflection from the paddle was calculated by using the zero-crossing method with the Reflected wave ($H_i = H_R$) and the Re-reflected wave ($H_R = H_{RR}$). An analysis using the power spectral density method was employed also to calculate the reflection coefficients for the wave generator, in the wave burst mode. This method was selected to circumvent noise-induced errors unavoidable in the wave measurements; however these errors if similar in numerator and denominator for the reflection coefficient calculation are reduced or canceled out. The results are shown in Table 8 for the coefficients obtained with the methods mentioned above, for the positions of gages 1, 2 and 3 as indicated in Fig. 8.

Table 8. Summary of the results obtained for 2D ARA model experiments burst mode

					Zero-crossing		Power spectral density				
H (m)	T (sec)	d (m)	ARA	Gage pos.	Reflected wave Hi (m)	Re-Reflected wave Hr (m)	Total energy Hi (m/Hz)	Total energy Hr (m/Hz)	Krr Zero-cross	Krr using PSD.	Krr Avg.
0.07	1.00	0.40	100%	1	0.0821	0.0253	0.0466	0.0043	0.308	0.304	0.323
				2	0.0836	0.0281	0.0458	0.0049	0.336	0.327	
				3	0.0814	0.0273	0.0397	0.0043	0.335	0.330	
0.07	1.00	0.40	NO	1	0.0691	0.0797	0.0416	0.0472	1.153	1.065	1.090
				2	0.0692	0.0786	0.0414	0.0471	1.136	1.066	
				3	0.0770	0.0818	0.0382	0.0427	1.062	1.057	
0.07	1.50	0.40	100%	1	0.0597	0.0077	0.0259	0.0006	0.129	0.150	0.117
				2	0.0617	0.0064	0.0297	0.0004	0.104	0.109	
				3	0.0596	0.0067	0.0315	0.0003	0.112	0.095	
0.07	1.50	0.40	NO	1	0.0618	0.0570	0.0291	0.0218	0.922	0.865	0.914
				2	0.0594	0.0638	0.0301	0.0227	1.074	0.868	
				3	0.0599	0.0581	0.0326	0.0199	0.970	0.782	
0.07	2.00	0.40	100%	1	0.0624	0.0097	0.0368	0.0001	0.155	0.059	0.131
				2	0.0584	0.0096	0.0385	0.0004	0.164	0.106	
				3	0.0606	0.0107	0.0371	0.0006	0.177	0.123	
0.07	2.00	0.40	NO	1	0.0545	0.0510	0.0384	0.0217	0.936	0.751	0.777
				2	0.0565	0.0490	0.0418	0.0204	0.867	0.699	
				3	0.0580	0.0449	0.0402	0.0161	0.774	0.634	

From the table, an average reflection coefficient (based on wave height) of Krr= 0.323, for the wave period of T=1.0 sec, is obtained. For the wave period of T=1.5 sec, an average Krr= 0.117, and for the wave period of T=2.0 sec, an average Krr= 0.131 is obtained. For the case of T=1.0 sec the Krr is significantly greater than that of the other 2 wave periods. It is believed that this is due to the evanescent modes not yet being taken into account. However a better performance can be seen for T=1.5 sec and T=2.0 sec; the coefficients obtained are close to the theoretical values indicated by Schaffer et al. (1994) and follow predictions reasonably well. On the other hand for the case of NO ARA, the average Krr (reflection coefficient of the wavemaker) coefficients are 1.09, 0.914, and 0.777 for the wave periods of T=1.0, 1.5, and 2.0 sec respectively. The results show a clear functioning of the 3D ARA mode system. Fig. 28 shows a comparison of the results obtained in the burst mode and the theoretical ones.

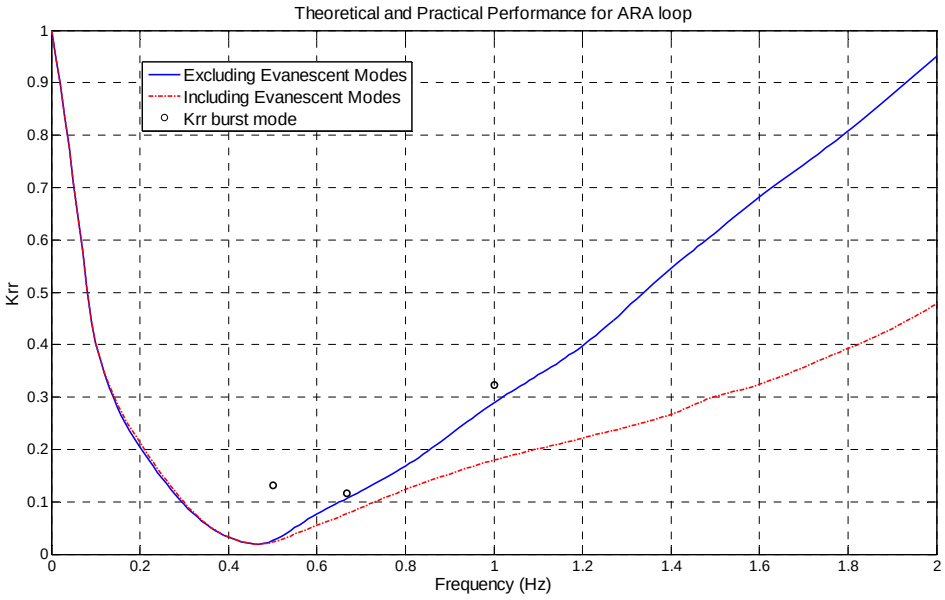

Fig. 28. Theoretical and Practical Performance for ARA Loop, 2D Model Tests (Burst Mode)

4.3.1.2 Continuous Wave Mode

The GEDAP program, REFLS, was used to calculate the reflection coefficient coming from the wall, as well as the incident and the reflected wave time series for the continuous wave mode. For this case the reflection coefficient coming from the wave generator was calculated using the formulation indicated in section 2.3.2 Eq. (39) and Table 9. The table shows the data employed to calculate the Krr for the wavemaker in the continuous mode. Fig. 29 through Fig. 31, show the wave traces for experiments 7 through 12 at the position of gage 1.

Fig. 29 shows the comparison for tests 7 and 10 (T=1.0 sec) where it can be observed in detail the difference between the opened and closed basin case, as well as the separated incident and reflected wave traces. For this case a Krr= 0.147 for the wavemaker was calculated. In a similar fashion Fig. 30 and Fig. 31 show the comparisons for experiments 8 and 11 (T=1.5 sec), and for 9 and 12 (T=2.0 sec), respectively. For these cases a Krr= 0.085 and Krr= 0.053 for the wavemaker were calculated. Fig. 29 shows that for the wave period T=1.0 sec, ARA is not stable and long period harmonics start after a short time of wave generation. On the other hand for wave periods T=1.5, and 2.0 sec, the performance is acceptable and the wave traces of the incident and reflected waves are in good agreement with the wave conditions used as input, although harmonics are also present. These harmonics are related with cross waves in the basin that influence the 1D calculation of the program REFLS.

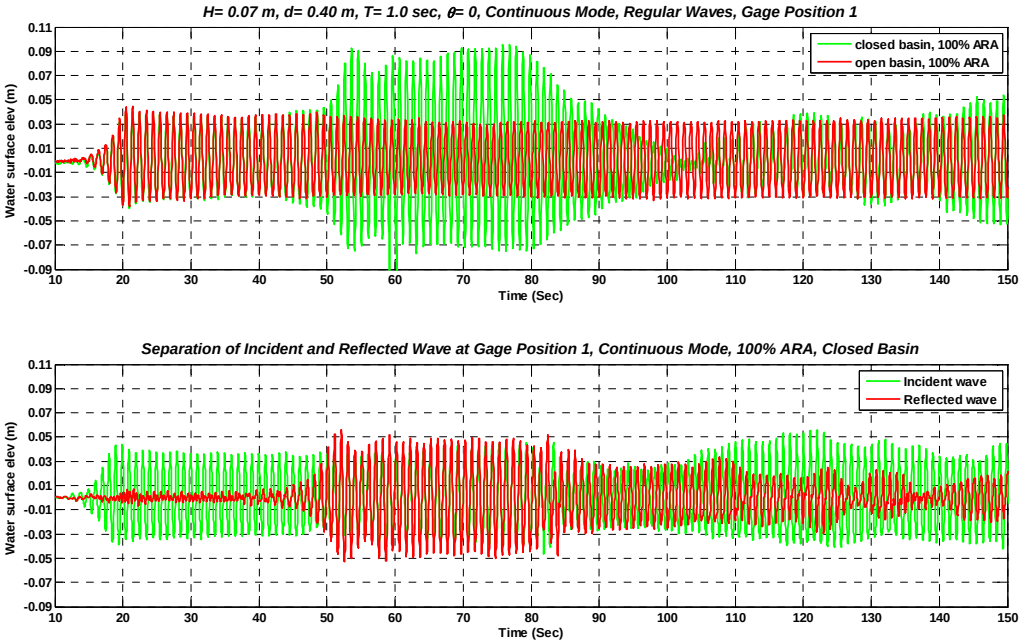

Fig. 29. Wave Traces for Experiments 7 and 10 at the Position of Gage 1, T= 1.00 sec, Continuous Mode, for Open and Closed Basin, with ARA, 0 Degree Angle

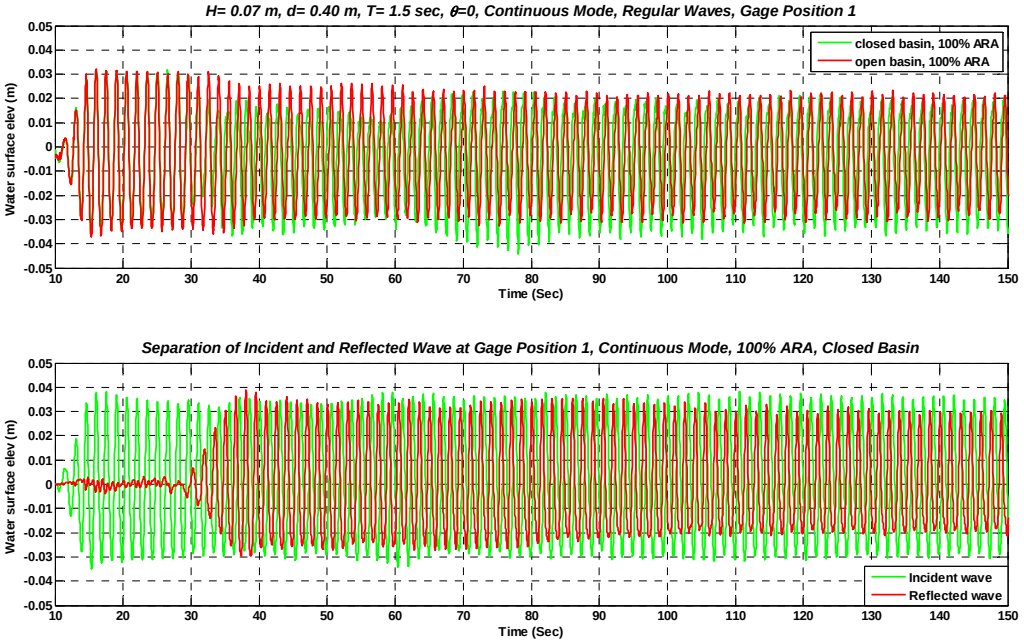

Fig. 30. Wave Traces for Experiments 8 and 11 at the Position of Gage 1, T= 1.50 sec, Continuous Mode, for Open and Closed Basin, with ARA, 0 Degree Angle

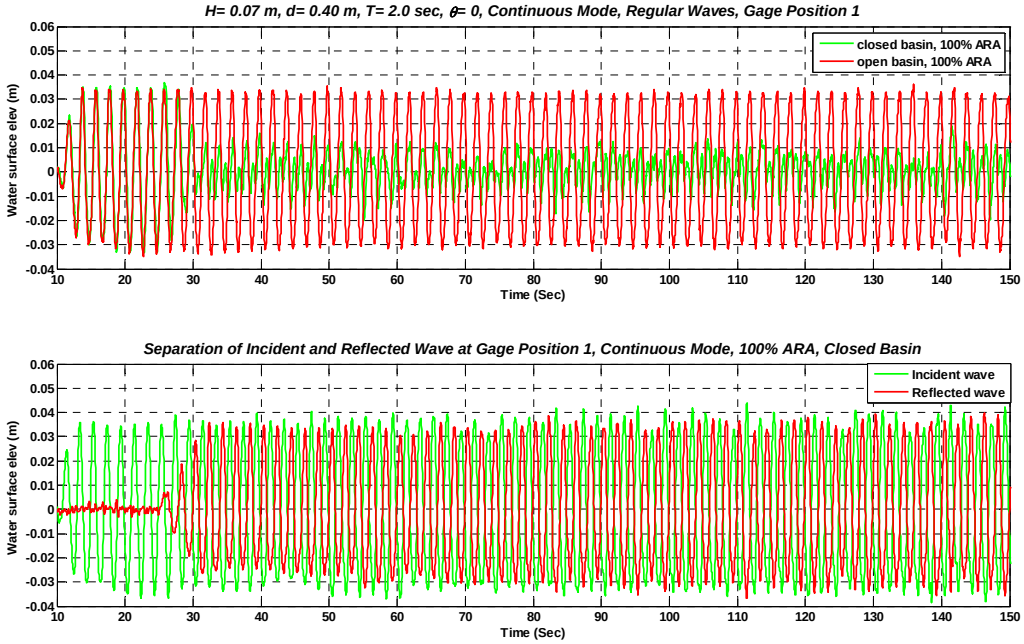

Fig. 31. Wave Traces for Experiments 9 and 12 at the Position of Gage 1, T= 2.00 sec, Continuous Mode, for Open and Closed Basin, with ARA, 0 Degree Angle

The situation just described related to the harmonics may explain the low Krr values calculated in the continuous mode versus those calculated in the burst mode. Table 9 summarizes the results obtained, and Fig. 32 shows the theoretical performance versus the practical performance for the continuous wave mode.

Table 9. Summary of the results obtained for 2D ARA model experiments continuous mode

H (m)	T (sec)	d (m)	ARA	Hi_{closed} (m)	Hr_{closed} (m)	Hi_{open} (m)	Krr formulation	Krr
0.07	1.00	0.40	100%	0.0741	0.0613	0.0651	$Krr = \frac{H_{I\ closed} - H_{I\ open}}{Hr_{closed}}$	0.147
0.07	1.50	0.40	100%	0.0646	0.0530	0.0601		0.085
0.07	2.00	0.40	100%	0.0714	0.0664	0.0679		0.053

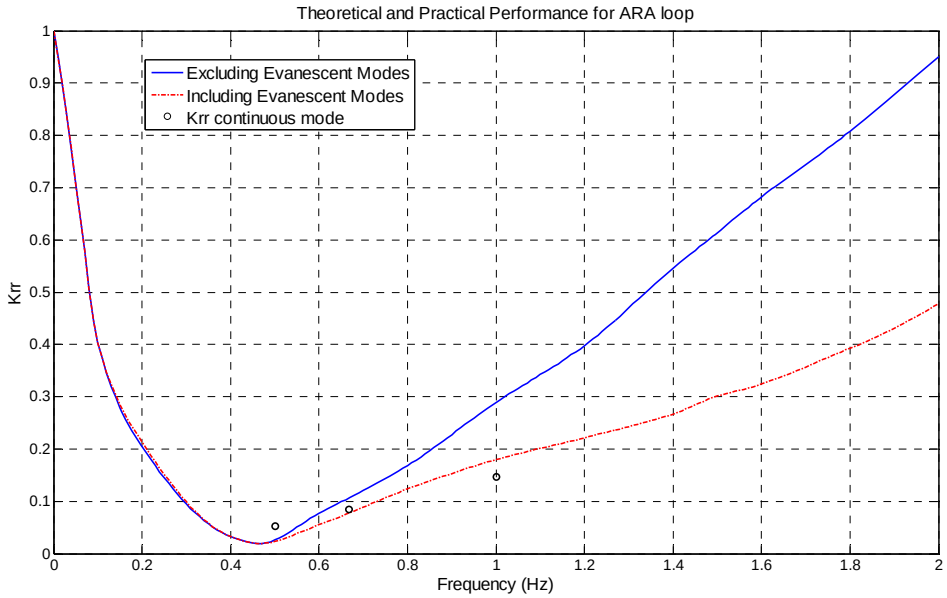

Fig. 32. Theoretical and Practical Performance for ARA Loop, 2D Model Tests (Continuous Mode)

Summarizing, the performance of the 3D ARA mode in 2D model tests just presented is satisfactory and indicates a fair performance of the ARA system, in continuous wave generation and absorption.

4.3.2 Results from Practical Performance from 3D Model Tests

4.3.2.1 Burst Wave Mode

This section presents the results of the 3D model tests to measure the performance of the 3D ARA mode of our wavemaker as indicated in section 3.3.4. Fig. 33 through Fig. 35 show the wave traces for experiments 1 through 6 (burst mode) at the

position of gage 5 for T= 1.00 sec, and gage 2 for T=1.50 and 2.00 sec. This was done due to failure of the wireless gages for the other positions (see Fig. 9). Fig. 33 shows the comparison for tests 1 and 4 (T=1.0 sec), where it is shown in detail the reflected wave originated by the reflector wall, traveling towards the wave maker, as well as the re-reflected wave from the wave maker, for both conditions ARA and NO ARA. In a similar fashion Fig. 34 and Fig. 35 show the comparisons for experiments 2 and 5 (T=1.5 sec), and for 3 and 6 (T=2.0 sec), respectively. It is pertinent to indicate also that due to the method waves were generated for this setup (30 degree angle), waves emitted from the wavemaker start propagating at once. This created diffraction on the right side of the setup (along the line where gage 4 is located) that introduced some cross-waves.

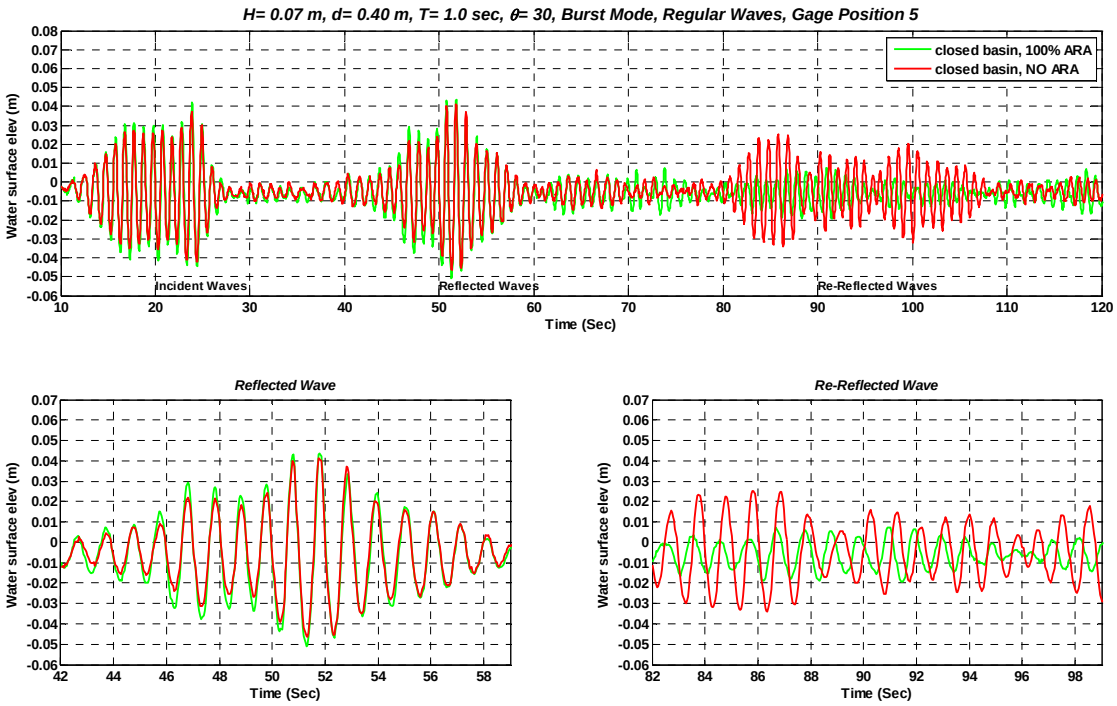

Fig. 33. Wave Traces for Experiments 1 and 4 at the Position of Gage 5, T = 1.00 sec, Burst Mode, Closed Basin, with and without ARA, 30 Degree Angle

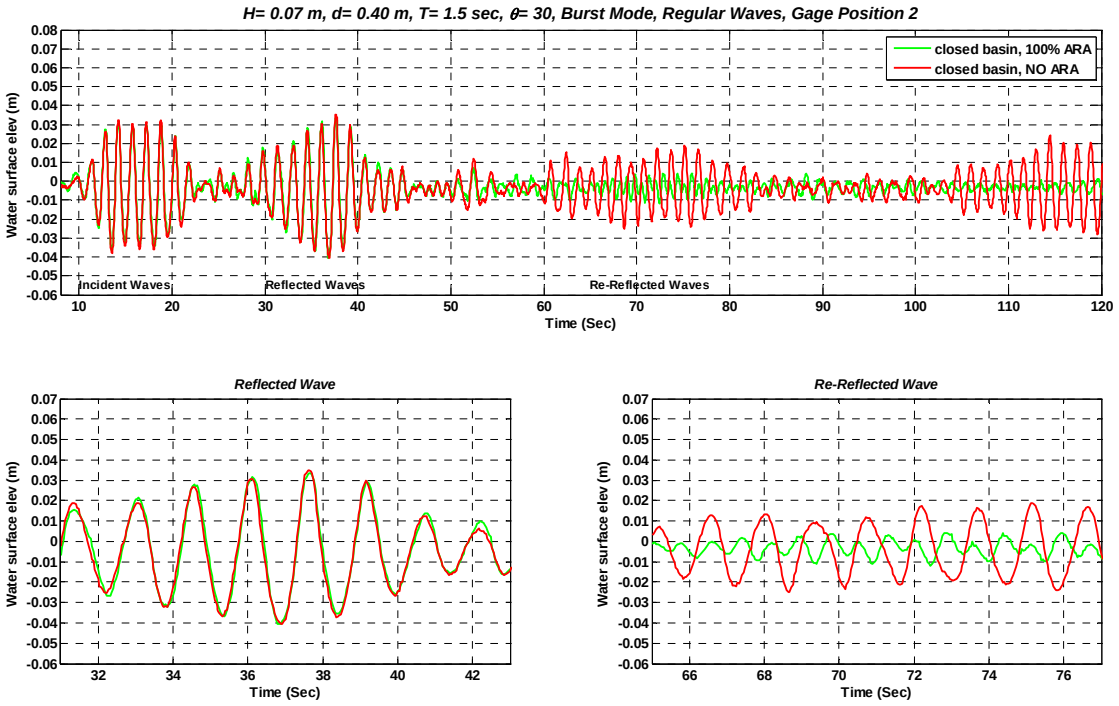

Fig. 34. Wave Traces for Experiments 2 and 5 at the Position of Gage 2, T = 1.50 sec, Burst Mode, Closed Basin, with and without ARA, 30 Degree Angle

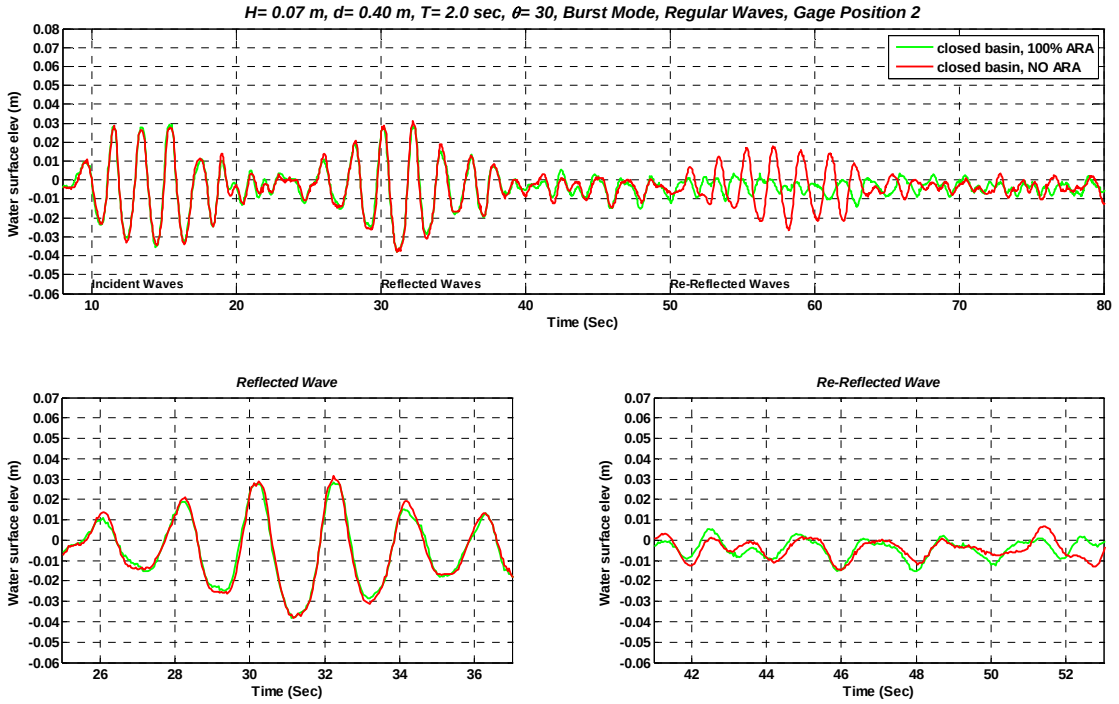

Fig. 35. Wave Traces for Experiments 3 and 6 at the Position of Gage 2, T = 2.00 sec, Burst Mode, Closed Basin, with and without ARA, 30 Degree Angle

From the figures above the reflection coefficient from the wavemaker was calculated only using the power spectral density method, since it gives the same results as the zero crossing method. The results are shown in Table 10 for the positions of gages 2 and 5 as indicated in Fig. 9.

Table 10. Summary of the results obtained for 3D ARA model experiments burst mode

					Power Spectral Density Method				
H (m)	T (sec)	d (m)	ARA	Gage	Total Energy Hi (m/Hz)	Total Energy Hr (m/Hz)	Krr Generator	Krr Generator ARA	Krr Generator No ARA
0.07	1.00	0.40	100%	5	0.0216	0.00209	0.311	0.311	0.726
			No		0.0170	0.0090	0.726		
0.07	1.50	0.40	100%	2	0.0195	0.0002	0.109	0.109	0.640
			No		0.0193	0.0079	0.640		
0.07	2.00	0.40	100%	2	0.0149	0.0003	0.149	0.149	0.694
			No		0.0165	0.0079	0.694		

From the table, a reflection coefficient Krr= 0.311, for the wave period of T=1.0 sec, is obtained. For the wave period of T=1.5 sec, a coefficient Krr= 0.109, and for the wave period of T=2.0 sec, a coefficient Krr= 0.149 is obtained. For the case of T=1.0 sec the Krr is significantly greater than that of the other 2 wave periods. As indicated before for the 2D model tests, it is believed this is due to the evanescent modes not yet taken into account. A better performance can be observed for T=1.5 sec and T=2.0 sec; the coefficients obtained are close to the theoretical values and follow predictions reasonably well. On the other hand for the case of NO ARA, the average Krr coefficients are 0.726, 0.640, and 0.694 for the wave periods of T=1.0, 1.5, and 2.0 sec respectively. The results show a clear functioning of the 3D ARA mode system for a

3D model setup. Fig. 36 shows a comparison of the results obtained in the burst mode and the theoretical ones.

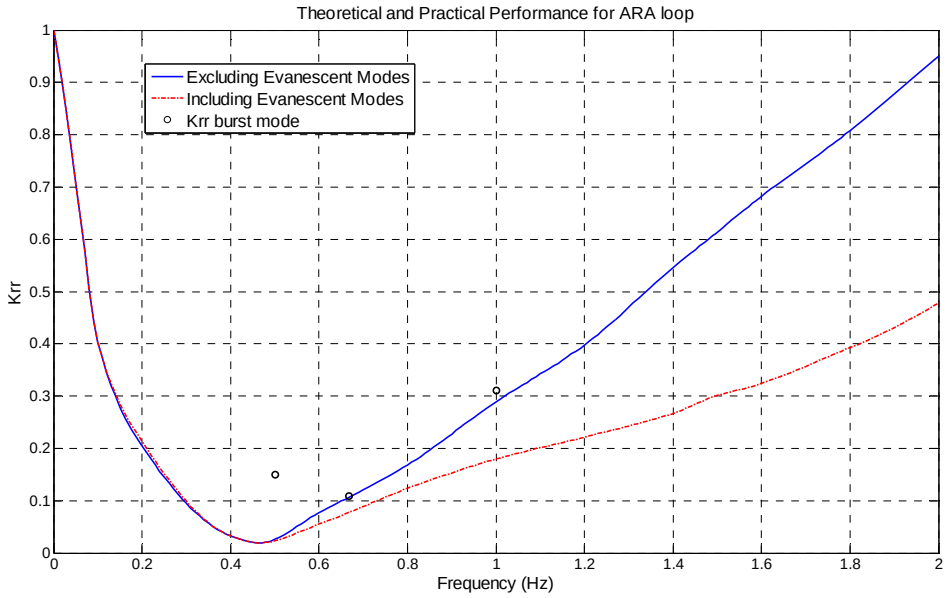

Fig. 36. Theoretical and Practical Performance for ARA Loop, 3D Model Tests (Burst Mode)

4.3.2.2 Continuous Wave Mode

The calculation made to obtain the incident and reflected waves is exactly the same as that already described in section 4.3.1.2, only this time for a 3D model setup. Table 11 shows the data employed to calculate the Krr for the wavemaker in the continuous wave mode. Fig. 37 through Fig. 39, show the wave traces for experiments 7 through 12 at the position of gage 1.

Fig. 37 shows the comparison for tests 7 and 10 (T=1.0 sec) where it can be observed in detail the difference between the opened and closed basin case, as well as

the separated incident and reflected wave traces. For this case a Krr= 0.187 for the wavemaker was calculated. In a similar fashion Fig. 38 and Fig. 39 show the comparisons for experiments 8 and 11 (T=1.5 sec), and for 9 and 12 (T=2.0 sec), respectively. For these cases a Krr= 0.080 and Krr= 0.236 for the wavemaker were calculated. Fig. 37 shows that for the wave period T=1.0 sec, ARA is not very stable and long period harmonics start after a short time of wave generation. On the other hand for wave periods T=1.5, and 2.0 sec, the performance is acceptable and the wave traces of the incident and reflected waves are in good agreement with the wave conditions used as input, although harmonics are also present especially at T= 2.00 sec. These harmonics are related with cross waves in the basin that influence the 1D calculation of the program REFLS, which may explain the value of Krr for T= 1.00 and 2.00 sec.

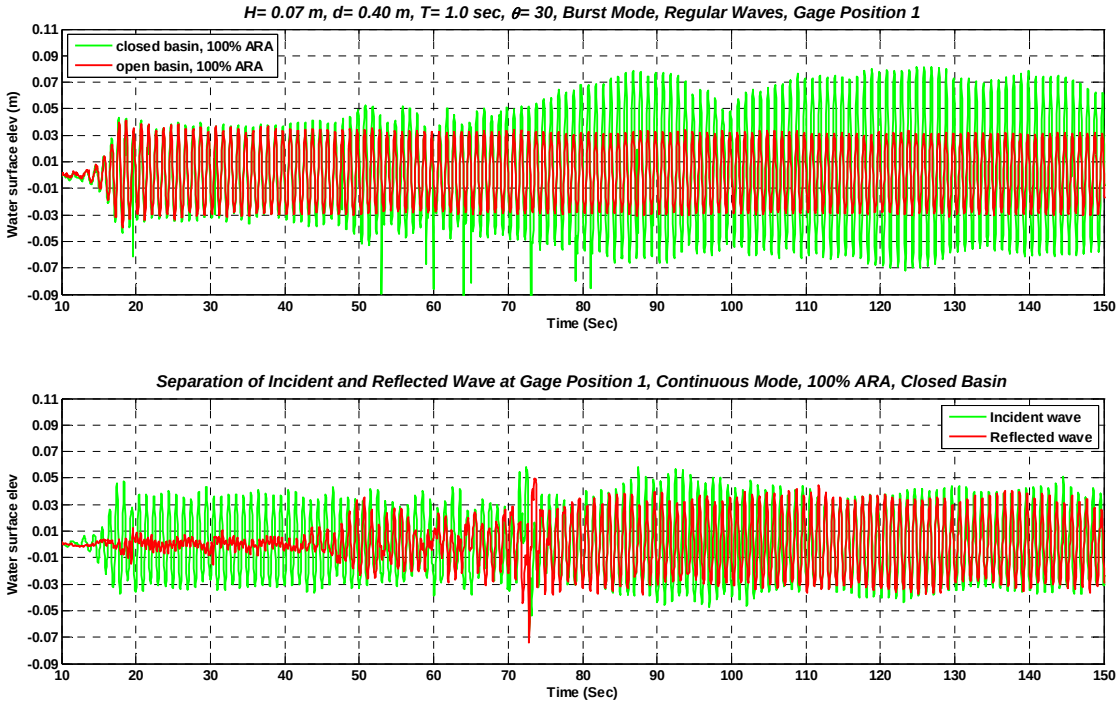

Fig. 37. Wave Traces for Experiments 7 and 10 at the Position of Gage 1, T= 1.00 sec, Continuous Mode, for Open and Closed Basin, with ARA, 30 Degree Angle

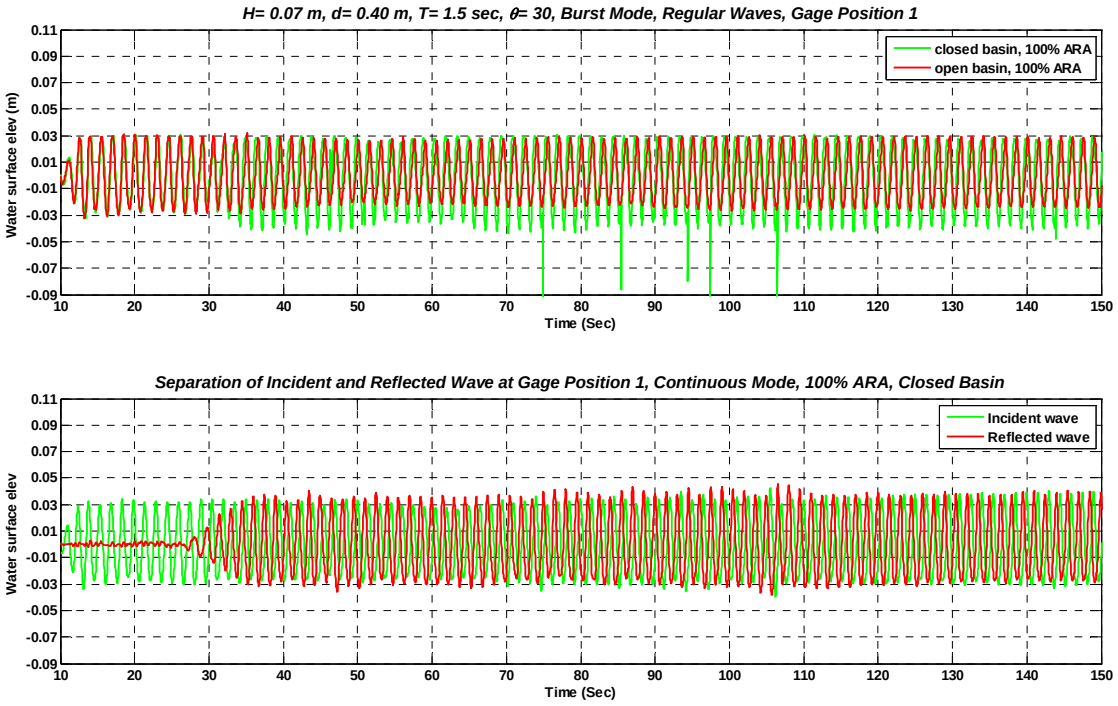

Fig. 38. Wave Traces for Experiments 8 and 11 at the Position of Gage 1, T= 1.50 sec, Continuous Mode, for Open and Closed Basin, with ARA, 30 Degree Angle

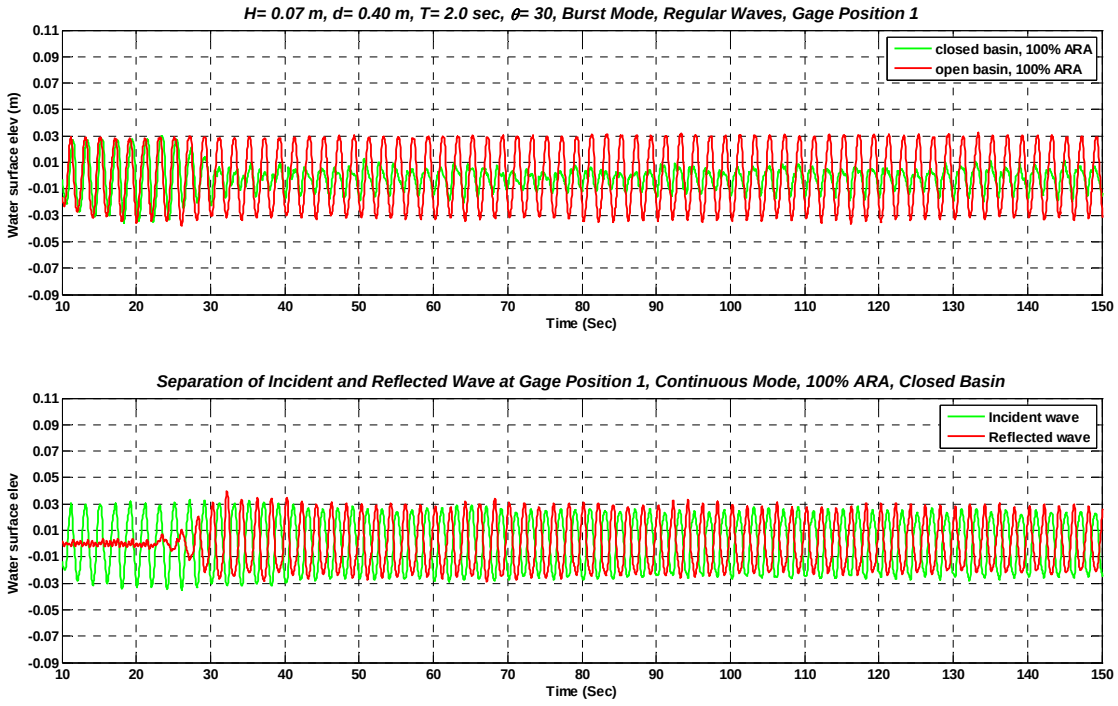

Fig. 39. Wave Traces for Experiments 9 and 12 at the Position of Gage 1, T= 2.0 sec, Continuous Mode, for Open and Closed Basin, with ARA, 30 Degree Angle

The situation just described related to the harmonics may explain the low Krr values calculated in the continuous mode versus those calculated in the burst mode. Table 11 summarizes the results obtained, and Fig. 40 shows the theoretical performance versus the practical performance for the continuous wave mode.

Table 11. Summary of the results obtained for 2D ARA model experiments continuous mode

H (m)	T (sec)	d (m)	ARA	Hi_{closed} (m)	Hr_{closed} (m)	Hi_{open} (m)	Krr formulation	Krr
0.07	1.00	0.40	100%	0.0731	0.0590	0.0621	$Krr = \frac{H_{I\ closed} - H_{I\ open}}{Hr_{closed}}$	0.187
0.07	1.50	0.40	100%	0.0632	0.0675	0.0578		0.080
0.07	2.00	0.40	100%	0.0541	0.0539	0.0668		0.236

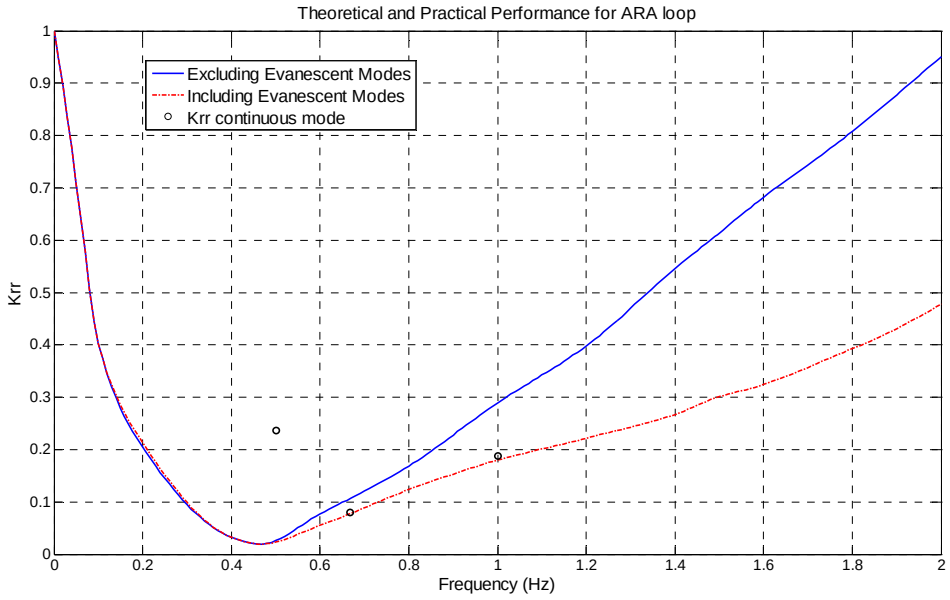

Fig. 40. Theoretical and Practical Performance for ARA Loop, 3D Model Tests (Continuous Mode)

Summarizing, the performance of the 3D ARA mode in 3D model tests just presented is satisfactory and indicates a fair performance of the ARA system, in continuous wave generation and absorption. Finally it is important to indicate that for the experiments mentioned above for the 2D and 3D setups, the 3D ARA loop must derive directional information from the signals using the spatial gain mixer, where the left and right adjacent wave height signals are combined with the center signal into a representative wave height signal for the center paddle. Assuming small paddle motion, a relation between wave frequency and error caused by wave angle was developed by Bosch-Rexroth and is presented in Fig. 41.

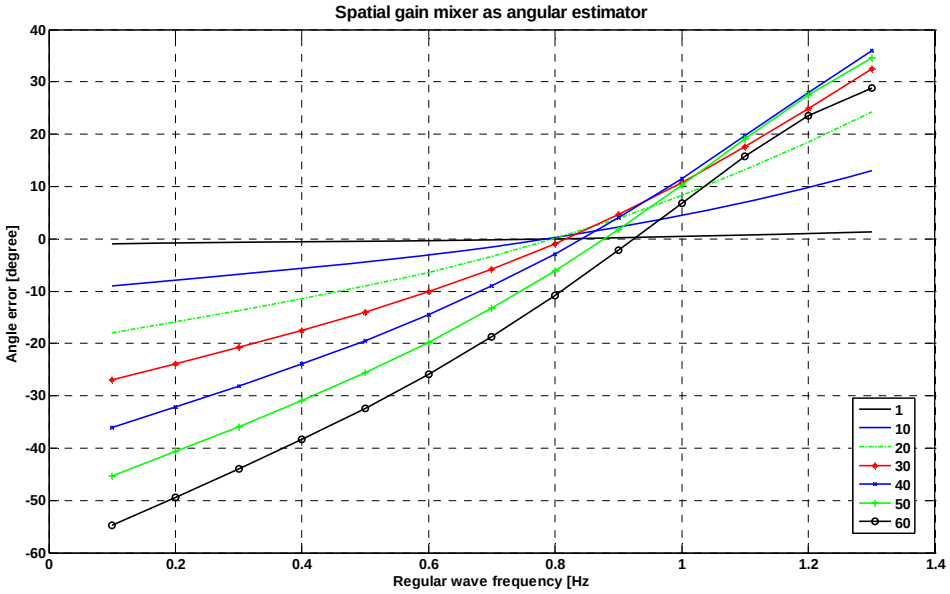

Fig. 41. Angle Error of the Spatial Gain Mixer, for Various Input Angles

From Fig. 41 it is observed that only at around 0.80-0.85 Hz does the spatial gain mixer work well for all directions. For the lower frequencies, the angle is

underestimated, therefore the motion reduction will be too small, and absorption performance will suffer. Similarly, for higher frequencies the angle is overestimated, and motion reduction is excessive; absorption performance will again be reduced. Nevertheless, qualitative experience shows that this approach is fruitful as it has been demonstrated.

4.3.3 Results from Practical Performance from 2D Model Tests, Using the Whole Wavemaker

Due to the repetitiveness of the description of the experiments and because these tests were made to validate the previous measurements, and also for testing the new SWF designed, we will just show a summary of the results in this section. Detailed graphs for the experiments pertaining to this section can be found in Appendix B.

4.3.3.1 Burst Wave Mode

Table 12 shows a summary of the results obtained for these tests. Here it can be observed that the performance of both filters the Rexroth SWF and the New SWF perform similarly. The advantage with the New SWF is that improved stability is achieved with high frequency waves. Fig. 42 shows the theoretical performance versus

the practical performance for the burst wave mode, using the whole wavemaker, for the position of the gages indicated in Fig. 10.

Table 12. Summary of the results obtained for 2D ARA model experiments using the whole wavemaker (burst mode)

					Power Spectral Density Method				
T (sec)	H (m)	d (m)	ARA	Gage	Total Energy Hi (m/Hz)	Total Energy Hr (m/Hz)	Krr Gen	Krr Gen Rex filter Avg	Krr Gen New filter Avg
1.00	0.07	0.40	100 % Rex SWF	1	0.0214	0.0014	0.26	0.27	0.27
			100% New SWF		0.0207	0.0015	0.27		
			No ARA		0.0170	0.0170	1.00		
			100 % Rex SWF	2	0.0229	0.0022	0.31		
			100% New SWF		0.0250	0.0024	0.31		
			No ARA		0.0211	0.0193	0.96		
			100 % Rex SWF	3	0.0260	0.0015	0.24		
			100% New SWF		0.0266	0.0015	0.24		
			No ARA		0.0230	0.0130	0.75		
1.50	0.07	0.40	100 % Rex SWF	1	0.0160	0.0002	0.11	0.11	0.13
			100% New SWF		0.0167	0.0002	0.11		
			No ARA		0.0161	0.0130	0.90		
			100 % Rex SWF	2	0.0146	0.0002	0.12		
			100% New SWF		0.0157	0.0003	0.14		
			No ARA		0.0155	0.0190	1.11		
			100 % Rex SWF	3	0.0175	0.0002	0.11		
			100% New SWF		0.0180	0.0003	0.13		
			No ARA		0.0184	0.0116	0.79		
2.00	0.07	0.40	100 % Rex SWF	1	0.0163	0.00006	0.06	0.06	0.06
			100% New SWF		0.0154	0.00004	0.05		
			No ARA		0.0157	0.0058	0.61		
			100 % Rex SWF	2	0.0162	0.00008	0.07		
			100% New SWF		0.0154	0.00009	0.08		
			No ARA		0.0153	0.0137	0.95		
			100 % Rex SWF	3	0.0164	0.0001	0.06		
			100% New SWF		0.0152	0.0001	0.06		
			No ARA		0.0155	0.0056	0.60		

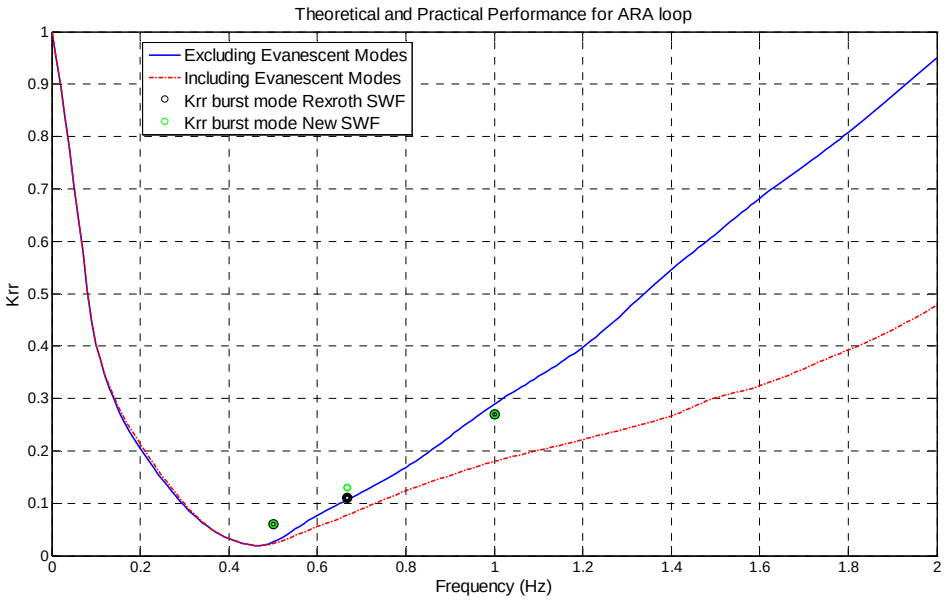

Fig. 42. Theoretical and Practical Performance for ARA Loop, 2D Model Tests Using the Whole Wavemaker (Burst Mode)

The performance of the 3D ARA mode in 2D model tests using the whole wavemaker is satisfactory and indicates a good performance of the ARA system, in burst wave generation for both filters, only this time a better fit with the theoretical performance is achieved, mainly due to the fact that cross waves for this mode were less than observed before and did not influence the calculations as much.

4.3.3.2 Continuous Wave Mode

Table 13 and Table 14 summarize the results obtained for the continuous wave mode for the Rexroth SWF and the New SWF respectively.

Fig. 43 shows the theoretical performance versus the practical performance for the continuous wave mode, using the whole wavemaker for both filters.

Table 13. Summary of the results obtained for 2D ARA model experiments using the whole wavemaker and Rexroth SWF continuous mode

H (m)	T (sec)	d (m)	ARA	Hi_{closed} (m)	Hr_{closed} (m)	Hi_{open} (m)	Krr formulation	Krr
0.07	1.00	0.40	100%	0.0634	0.0511	0.0710	$Krr = \frac{H_{I\,closed} - H_{I\,open}}{Hr_{closed}}$	0.149
0.07	1.50	0.40	100%	0.0669	0.0510	0.0627		0.082
0.07	2.00	0.40	100%	0.0661	0.0636	0.0617		0.069

Table 14. Summary of the results obtained for 2D ARA model experiments using the whole wavemaker and New SWF continuous mode

H (m)	T (sec)	d (m)	ARA	Hi_{closed} (m)	Hr_{closed} (m)	Hi_{open} (m)	Krr formulation	Krr
0.07	1.00	0.40	100%	0.0675	0.0682	0.071	$Krr = \frac{H_{I\,closed} - H_{I\,open}}{Hr_{closed}}$	0.051
0.07	1.50	0.40	100%	0.0665	0.0563	0.0652		0.023
0.07	2.00	0.40	100%	0.065	0.0631	0.0624		0.041

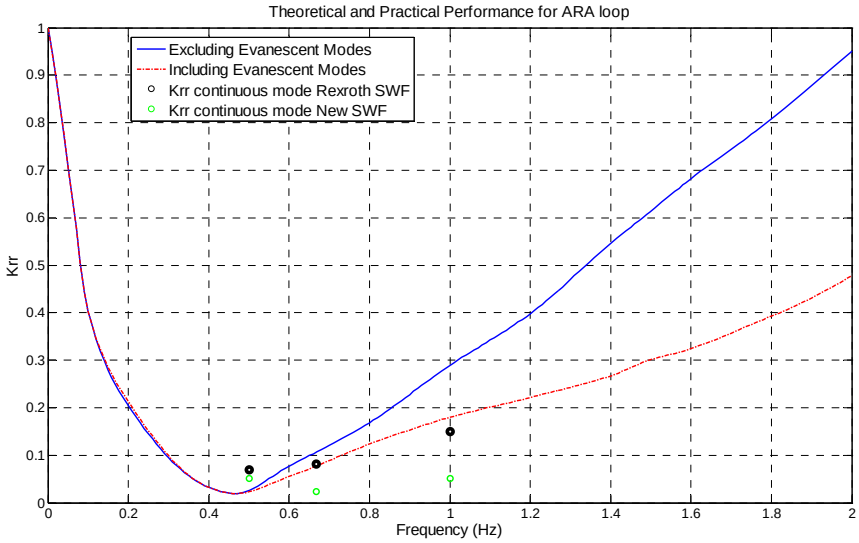

Fig. 43. Theoretical and Practical Performance for ARA Loop, 2D Model Tests Using the Whole Wavemaker for Rexroth SWF, and New SWF (Continuous Mode)

The performance of the 3D ARA mode in 2D model tests using the whole wavemaker is satisfactory and indicates a good performance of the ARA system, in continuous wave generation and absorption for both filters. The cross waves for the continuous mode were observed and can be confirmed in the wave traces shown in Appendix B. However this time the coefficient of reflection calculated with the program REFLS showed a better performance.

4.4 Results of the Program Developed for DOA Detection and Validation with Measured Data

The theory presented in Chapter II related to DDDA beamformer (section 2.5.2) has been implemented through Matlab^{TM}. The program developed was tested first with synthetic data and later with data measured in the wave tank. The calculations were performed with K=5, meaning only 5 snapshots were employed. Sampling rate of the synthetic and measured signals was of 250 Hz. Fig. 44 shows an example of the output for the synthetic data calculation for a 30 degree angle; the figure also includes an example of the synthetic data used.

For use of the program with synthetic data it was obvious that this algorithm is good as long as a good estimate of the wave length is provided (which in turn depends on the wave frequency). It was also noticed that if only one direction is present on the wave field a short number of samples can be used; at 250 Hz it is required about 0.020 sec of sampling, and as few as 5 sensors to estimate accurately the DOA of the waves. If

we add another direction, then with the conditions mentioned above the DOA's cannot be resolved.

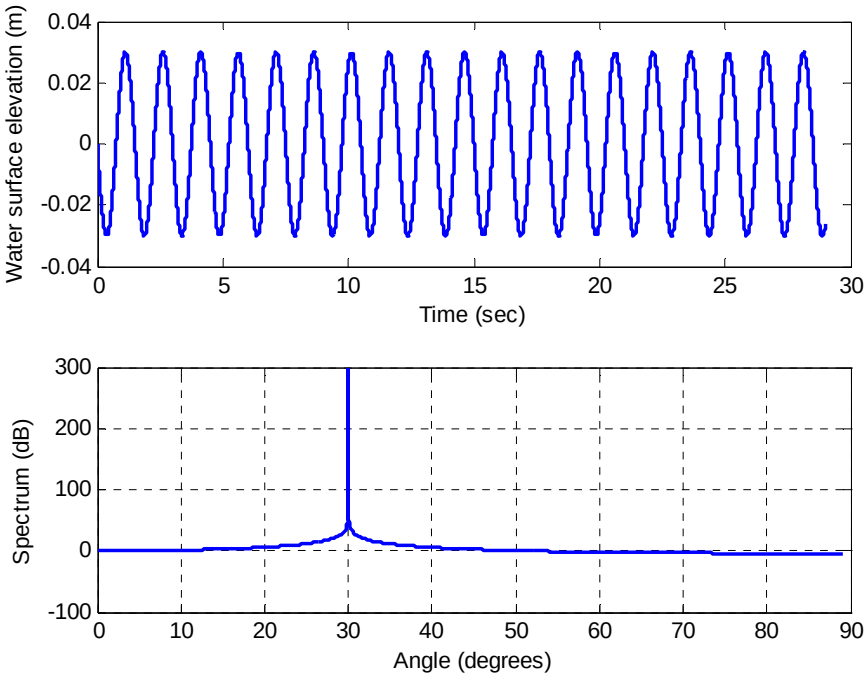

Fig. 44. Output of DDDA Beamformer Algorithm, Synthetic Data, T=1.5 sec, 9 Wave Gages Used for Calculation

Therefore it was required to increase the number of sensors in the calculation (extend the space), then if the number of sensors is increased from 5 to 7 sensors, the DOA's are resolved. This situation is basically a trade of sampling time, number of sensors used, and noise. It needs to be pointed out that this applies for wave periods of not less of 0.80 sec, and water depths greater than 0.25 m approximately. This is due to the separation among gages. Also the wave length should not exceed half of the wave length for good beamforming.

4.4.1 Results from Preliminary Tests for Validation of DOA Program with Measured Data

The program was adapted to calculate the DOA of the reflected waves from data measured in the tank, since we can prepare a series of steering vectors that will scan the waves until one or several of them locate the DOA's of the reflected waves. This scanning of the waves was performed every 0.20 sec to estimate the DOA. A total of 11 gages were used for the calculations. The value of θ to apply the ARA correction was estimated this way. Fig. 45 shows an example of the calculation applied to data measured in the wave basin, including data for one gage.

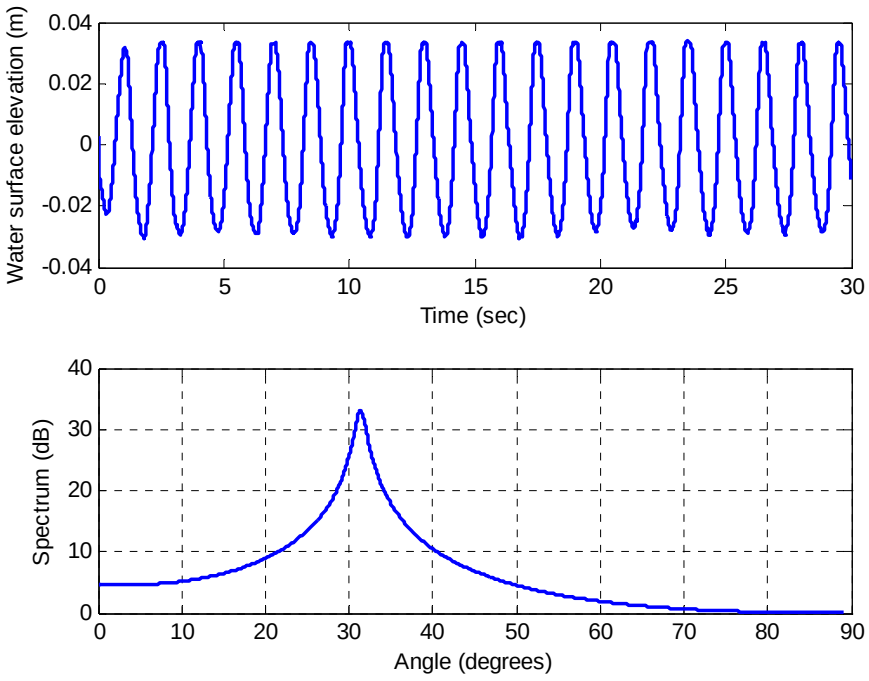

Fig. 45. Output of DDDA Beamformer Algorithm, Measured Data, T=1.5 sec, 11 Wave Gages Used for Calculation

Fig. 46 through Fig. 50 show the results obtained from the tests indicated in Table 5 (section 3.4.1) using the DDDA program, only for the wave period T= 1.00 sec. Here it can be observed that in general the angle of incidence calculated for each snapshot was properly estimated most of the time. The rest of the figures showing the results for the other wave periods indicated in Table 5 are shown in Appendix C. There it can be observed that also the angle of incidence is in general very close to what the angle formed by the array with the crest of the waves was. From these results it is observed that an acceptable performance from the algorithm has been achieved, and based on this it is possible to use it in combination with the ARA loop of our wavemaker, and in general with any wavemaker, with a similar configuration.

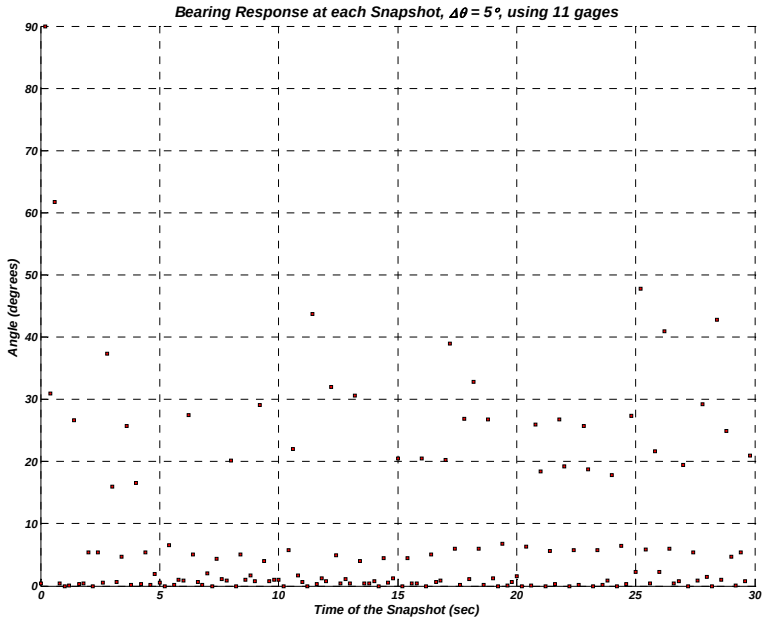

Fig. 46. Bearing Estimation from Wave Data: Regular Waves, T= 1.00 sec, H= 0.06 m, θ= 0 Degrees

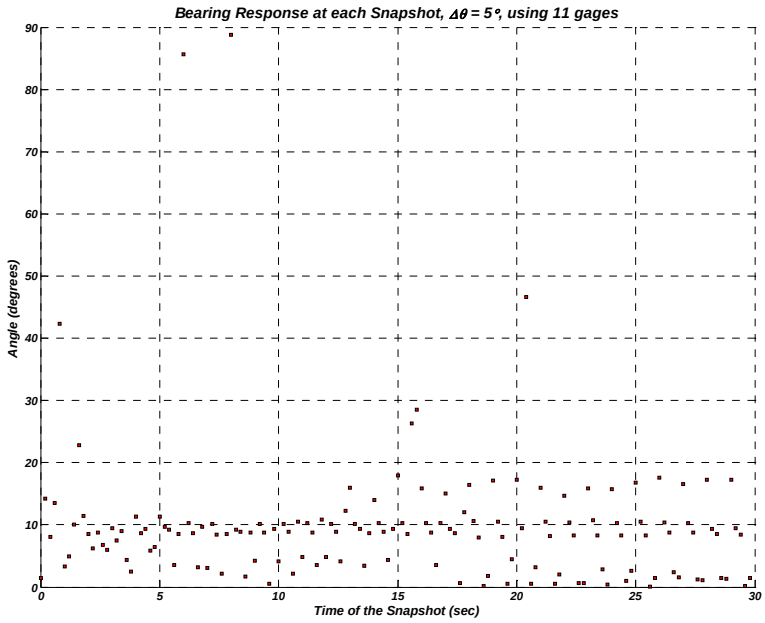

Fig. 47. Bearing Estimation from Wave Data: Regular Waves, T= 1.00 sec, H= 0.06 m, θ= 10 Degrees

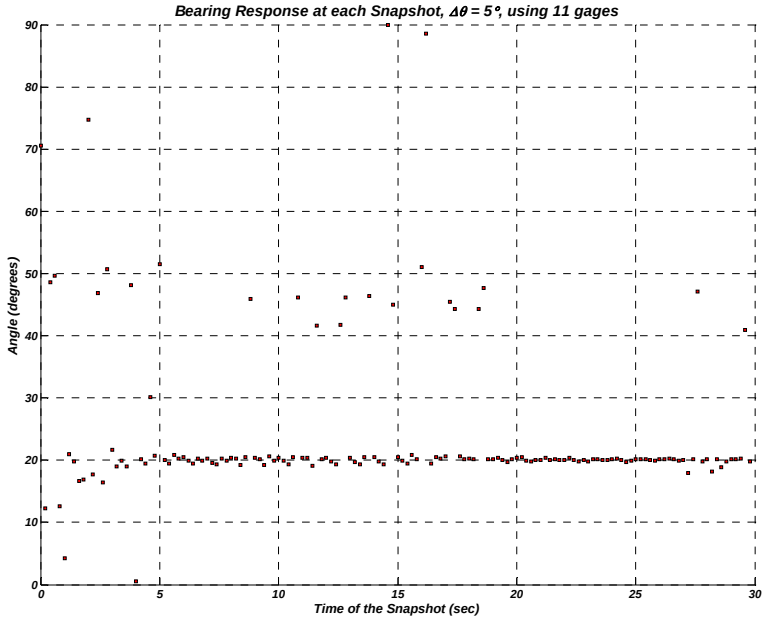

Fig. 48. Bearing Estimation from Wave Data: Regular Waves, T= 1.00 sec, H= 0.06 m, θ= 20 Degrees

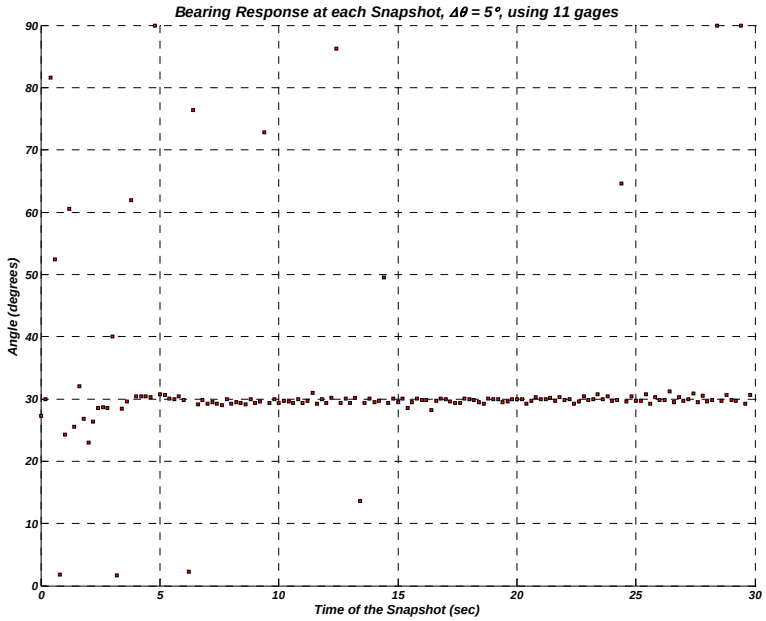

Fig. 49. Bearing Estimation from Wave Data: Regular Waves, T= 1.00 sec, H= 0.06 m, θ= 30 Degrees

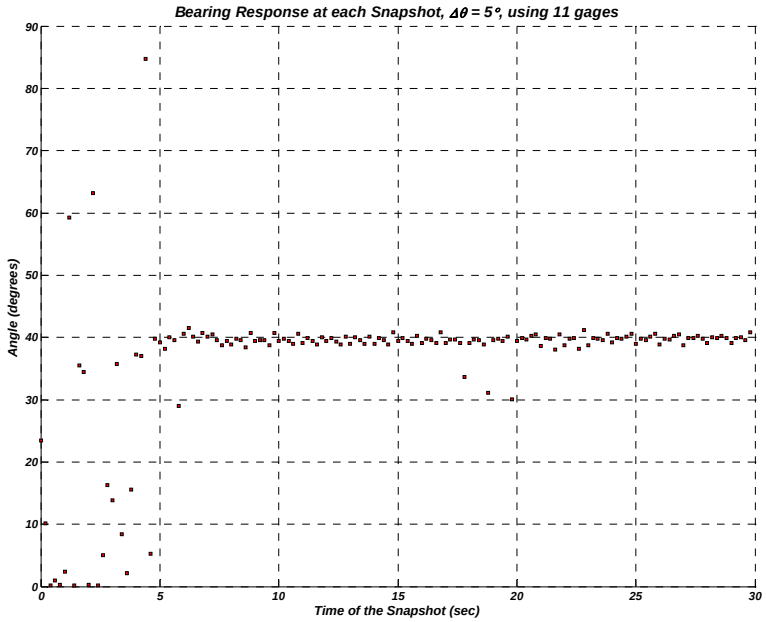

Fig. 50. Bearing Estimation from Wave Data: Regular Waves, T= 1.00 sec, H= 0.06 m, θ= 40 Degrees

4.5 Results from 2D and 3D Model Tests for Validation of DOA Program with Data Obtained from the Control System of TAMU Wavemaker

The results obtained from measurements in 2D and 3D model setups allowed to verify the performance of the DOA program, with data obtained from the control system of our wavemaker. The program was adapted to calculate the DOA of the reflected waves using these data. A total of 11 paddles were used for the calculations. The value of θ to apply the ARA correction was calculated this way.

4.5.1 Validation from 2D and 3D Model Tests

A summary of these results is provided in Table 15 for the 2D model tests (0 degrees), and Tables 16 and 17 for the 3D model tests (30 degrees). These tables show an estimation of the accuracy of the calculations based in the percentage of points lying within a range defined as possible tolerances for the estimation of the DOA of reflected waves. It can be observed that only a portion of the data recorded was used to estimate the percentages, this is due to we selected data portions where the reflected waves arrived to the wavemaker, which was determined from the burst mode tests. Therefore the same portions of the data that showed reflected waves in the burst mode were used for the continuous mode tests in order to make comparisons. The figures showing the bearing estimation used to obtain the tables are shown in Appendix D.

In general it can be observed that for the 2D model tests the average of the time that the DOA calculation was performed properly is about 78%. For the case of the 3D model tests the average drops to 52.2 % when considering an angle range of 25-35 degrees. If considering an angle range of 20-40 this percentage increases to 66.3%

Table 15. Accuracy of DOA for ARA experiments, 2D model monochromatic waves (0 degrees)

Test	Time Range (sec)	Angle Range (degrees)	Number of points in Time Range	Number of points in Angle Range	%	Wave Generation Mode	ARA condition
1	50-75	0-10	125	78	62.4	burst	100%
2	40-60	0-10	100	83	83.0		
3	35-50	0-10	75	67	89.3		
4	60-80	0-10	100	72	72.0	burst	NO ARA
5	40-60	0-10	100	80	80.0		
6	35-50	0-10	75	64	85.0		
7	50-75	0-10	125	83	66.4	continuous	100%
8	40-60	0-10	100	87	87.0		
9	35-50	0-10	75	69	92.0		
10	50-75	0-10	125	75	60.0	continuous	NO ARA
11	40-60	0-10	100	80	80.0		
12	35-50	0-10	75	58	77.3		

Table 16. Accuracy of DOA for ARA experiments, 3D model monochromatic waves (30 degrees)

Test	Time Range (sec)	Angle Range (degrees)	Number of points in Time Range	Number of points in Angle Range	%	Wave Generation Mode	ARA condition
1	64-74	25-35	50	27	54.0	burst	100%
2	46-54	25-35	40	28	70.0		
3	40-46	25-35	30	11	36.7		
4	65-75	25-35	50	40	80.0	burst	NO ARA
5	44-54	25-35	50	30	60.0		
6	38-48	25-35	50	18	36.0		
7	60-73	25-35	65	52	80.0	continuous	100%
8	45-75	25-35	150	91	60.7		
9	40-80	25-35	200	63	31.5		
10	60-73	25-35	65	40	61.5	continuous	NO ARA
11	45-75	25-35	150	61	40.7		
12	40-80	25-35	200	30	15.0		

Table 17. Accuracy of DOA for ARA experiments, 3D model monochromatic waves (30 degrees) angle range increased

Test	Time Range (sec)	Angle Range (degrees)	Number of points in Time Range	Number of points in Angle Range	%	Wave Generation Mode	ARA condition
1	64-74	25-35	50	30	60.0	burst	100%
2	46-54	25-35	40	34	85.0		
3	40-46	25-35	30	16	53.3		
4	65-75	25-35	50	40	80.0	burst	NO ARA
5	44-54	25-35	50	43	86.0		
6	38-48	25-35	50	26	52.0		
7	60-73	25-35	65	52	80.0	continuous	100%
8	45-75	25-35	150	121	80.7		
9	40-80	25-35	200	105	52.5		
10	60-73	25-35	65	41	63.1	continuous	NO ARA
11	45-75	25-35	150	103	68.7		
12	40-80	25-35	200	68	34.0		

The decrease in the accuracy of the DOA estimation for the 2D and 3D model tests can be explained because of the considerations done for the steering vector, which considers the array of sensor as linear. This is mostly true since in this case the paddle position movement is relatively small compared with the separation and number of gages used. However when ARA is activated it can be seen paddle excursions that may create the lower performance observed, since a more sinusoidal position type of array is present if we look at positions at certain time. Summarizing, the performance of the program for DOA estimation is fair. However a new formulation for the steering vector needs to be developed in order to corroborate if this improves the performance.

On the other hand a program developed in Simulink^{TM} was used with the DOA program to obtain the paddle correction by using the angles obtained. As mentioned

above this can be done in a small portion of the data recorded (the same indicated in the tables). Just to illustrate this calculation Fig. 51 shows a comparison among the paddle position corrections obtained with the 2D ARA loop, the spatial gain-mixer (3D ARA loop), and the same paddle position but calculated with the DOA program. The figure shows the net corrections applied for each approach. As it can be observed, the spatial gain-mixer underestimates the correction that needs to be applied if it is compared with the correction obtained with the DOA program. It can be noticed also the similitude between the correction with the 2D ARA loop and the DOA program, this can be expected due to as it was explained before what it was done is to obtain the paddle position correction using the 2D ARA loop and then with the $\cos(\theta)$ factor obtain the proper correction. Fig. 52 shows the schematic in Simulink™ where the DOA program feeds data to the 2D ARA loop.

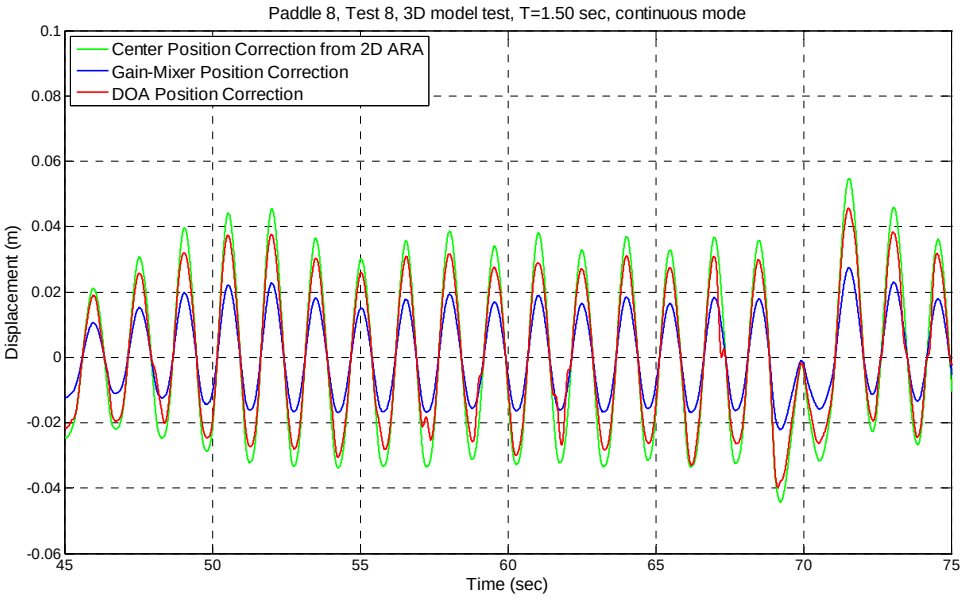

Fig. 51. Paddle Position Correction Using Different Approaches: Regular Waves, T= 1.50 sec, H= 0.06 m, θ= 30 Degrees

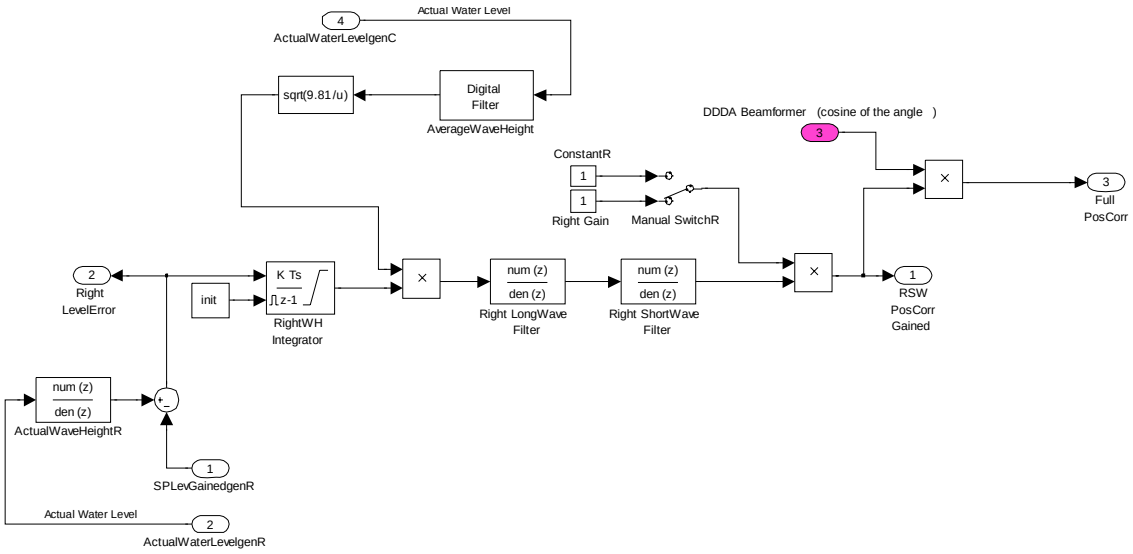

Fig. 52. DOA Program Feeding Data to 2D ARA Loop

A portion of the Simulink™ program corresponding to the 3D ARA loop (spatial gain-mixer), is shown in Appendix E.

CHAPTER V

CONCLUSIONS

5.1 Summary

The existing system was evaluated theoretically and with physical tests in a 3D wave basin for different conditions of reflected waves arriving with an angle to the wavemaker front and acceptable performance has been found for the 3D ARA mode. The performance of the 3D ARA mode in 2D model tests using the whole wavemaker was also satisfactory and indicates a good performance of the ARA system, in continuous wave generation and absorption.

Due to the poor stability shown in the preliminary tests of the 2D ARA mode, a new SWF was designed, however stability problems still appear at high frequencies. This situation indicates that a better tune up of the filters needs to be conducted. In general the system behaves acceptably for the 3D ARA mode from the physical tests performed.

On the other hand, for the DOA program, the tests conducted with measurements in the tank for validation show that for regular waves the DDDA method is able to accurately detect the DOA of these in as few as 5 snapshots, with a minimum of 7 gages used as the antenna input. Also with data obtained directly from the control system of the wavemaker using regular waves, the program was able to determine the DOA. The computational burden of the algorithm is not significant in the case of regular waves. For

the case of irregular waves this computational burden may increase since several frequencies need to be considered.

5.2 Recommendations

The steering vector assumed for the DOA program needs to take a general form to better scan the waves, especially when ARA is activated since the gages mounted on the paddles are not really in a line. This new formulation needs to be tested in order to corroborate if this improves the performance.

A modification of the DOA program is also required to analyze the reflected irregular waves, which may increase computational burden. Actual implementation of this program to the control system needs to be conducted in conjunction with Bosch-Rexroth.

REFERENCES

Bosch-Rexroth (2004). Operation Manual for the 3D Multidirectional Wavemaker for the Haynes Coastal Engineering Laboratory. College Station, TX.

Christensen, M., and Frigaard, P. (1994). Design of absorbing wave maker based on digital filters. Proc. Waves – Phys. and Numer. Modelling, Vancouver, Canada, pp. 100-109.

Dalrymple, R. A., (1989). Directional wave maker theory with sidewall reflection. J. Hydraulic Research, 27(1), pp. 23-34.

Dean, R.G., and Dalrymple, R.A., (1984). Wavemaker theory. Water Wave Mechanics for Engineers and Scientists, Prentice-Hall, Englewood Cliffs, N.J., pp. 170–180. ISBN: 0-13-946038-1

Havelock, T. H., (1929). Forced surface waves on water. Phil. Mag. 8, pp. 569-576.

Hirakuchi, H., Kajima, R., Shimizu, T., and Ikeno, M., (1992). Characteristics of Absorbing Directional Wave Maker. Proc. 23rd Int. Conf. on Coast. Engrg., ASCE, Venice, Italy, ed. New York, pp. 281-294.

Ito, K., Katsui, H., Mochizuki, M. and Isobe, M., (1996). Non-reflected multidirectional wave maker theory and experiments of verification. Proc. 25th Int. Conf. on Coast. Engrg., ASCE, Orlando, FL., ed. New York, pp. 443-456.

Kim, J. T., Moon, S. H., Han, D. S., and Cho, M. J., (2005). Fast DOA estimation algorithm using pseudocovariance matrix. IEEE Transactions on Antenas and Propagation, 53(4), April 2005., pp. 1346-1351.

Klopman, G., Reniers, A. J. H. M., Wouters, J., and De Haan, Th., (1996). Active multidirectional wave absorption. Abstract No. 415, 25th Int. Conf. on Coast. Engrg., ASCE, Orlando, FL.

Klopman, G., Dongeren, A. V., Reniers, A., and Petit, H., (2001). High-quality laboratory wave generation for flumes and basins. In: Edge, B.L. and Helmsley, J. M. (Eds.), Proc. 4th Int. Symp. Waves: Ocean Wave Measurement and Analysis, ASCE, San Francisco, CA, pp. 1190-1199.

Madsen, O. S., (1974). A three-dimensional wavemaker, its theory and application. J. of Hydraulic Research, 12(2), pp. 205-222.

Mansard, E.P.D., and Funke E.R. (1980). The measurement of incident and reflected spectra using a least squares method. Proc. 17th Int. Conf. on Coast. Engrg., ASCE, Sydney, Australia, Vol. 1, pp. 154-172.

Miles, M.D., (1997). GEDAP User's Guide for Windows NT. Canadian Hydraulics Centre, Ottawa, Ontario, Canada.

Milgram, J. H., (1970). Active water wave absorbers. J. Fluid. Mech. 43(4), pp. 845-859.

Salter S. H. (1981). Absorbing wave makers and wide tanks. Proc. Directional Wave Spectra Applications, Berkeley, Calif., pp. 185-202.

Salter S. H. (1984). Physical modeling of directional seas. Proc. Symp. Description and Modeling of Directional Seas, Copenhagen, Denmark, pp. D-74-D-82.

Schaffer, H. A. (2001). Active wave absorption in flumes and 3D basins. Proc. 4th Int. Symp. Waves: Ocean Wave Measurement and Analysis, ASCE, San Francisco, Calif., pp. 1200-1208.

Schaffer, H. A., Fuchs J. U., and Hyllested, P. (2000). An absorbing multidirectional wave maker for coastal applications. Proc. 27th Int. Conf. on Coast. Engrg., ASCE, Sydney, Australia, ed. New York, pp. 981-993.

Schaffer, H. A., and Hyllested, P. (1999). Reflection analysis using active wave absorption control system. Proc. Int. Conf. Coast. Structures '99, Santander, Spain, pp. 93-99.

Schaffer, H. A., and Klopman, G. (2000). Review of multidirectional active wave absorption methods. J. Wtrwy., Port, Coast., and Oc. Engrg., ASCE, 126(2), pp. 88-97.

Schaffer, H. A., and Skourup, J. (1996). Active absorption of multidirectional waves. Proc., 25th Int. Conf. on Coast. Engrg., ASCE, Orlando, FL., ed. New York, pp. 55-66.

Schaffer, H. A., Stolborg, T., and Hyllested, P. (1994). Simultaneous generation and active absorption of waves in flumes. Proc. Waves- Phys. Numer. Modelling, Dept. of Civ. Engrg., University of British Columbia, Vancouver, Canada, pp. 90-99.

Steenberg, C. M., and Schaffer, H. A. (2000). Second-order wave generation in laboratory basins. Proc. 27th Int. Conf. on Coast. Engrg., ASCE, Sydney, Australia, ed. New York, pp. 994-1007.

Swanson, D. C., (2000). Signal Processing for Intelligent Sensor Systems. Marcel Dekker, Inc. New York-Basel., ISBN: 0-8247-9942-9

APPENDIX A

```
clc
clear all
close all
% Programmer: Oscar Cruz-Castro
% Date created: May/19/08
% Last update: Feb/10/09

ns=input('Enter # of waves (signals) to analyze: ');
T(ns)=0;                % Array to store the wave periods
global nos
nos=11;                 % Number of sensors (wave gages) to analyze ***********
inc=0.48;               % Separation in meters of the grid elements in the
                        % "x" and "y" axes (square)
g=9.81;                 % Gravitational constant (m2/s)
h=0.30;                 % Water depth in the tank (m)
Lsh(ns)=0;              % Array to store the wave lengths (m)
k(ns)=0;                % Array to store the wave numbers (1/m)

% (For) cycle to gather data and calculate Wave Length, number and freq.
for i=1:ns
    T(i)=input('Enter the wave period in seconds: ');
    % Wave Length calculation using shallow approximation (acc Fenton)
    Lsh(i)=(g*T(i)^2/(2*pi)).*(tanh(((2*pi/T(i)).^2.*h/g).^(3/4)).^(2/3));
    k(i)=2*pi/Lsh(i);   % Wave number
end

fs=250;                 % Sampling frecuency in Hz
dfactor=inc./Lsh;       % Relationship of array aperture should not exceed
                        % 0.5*Wave lenght for good beamforming
longi=60;   %length of the plot***************
name1='jun6Jons_H06';
name2='_T1_30g_';
name3='C:\Users\Oscar Cruz
Castro\Desktop\DDDAProgramOscar_Lastversion\Figures_DDDA_fordata\';
Wls=load([name1 name2 'w' '.dat']);
Res=load([name1 name2 'r' '.dat']);  %Load Data*****************************

Wls1(size(Wls,1),size(Wls,2)-2)=0;
for j=1:size(Wls,2)-2
    Mean=mean(Wls(:,j+1));          %Substract mean for all wireless gages
    Wls1(:,j)=Wls(:,j+1)-Mean;
end
Res1(size(Res,1),size(Res,2)-1)=0;
for j=1:size(Res,2)-1
    Mean2=mean(Res(:,j+1));         %Substract mean for all resistance gages
    Res1(:,j)=Res(:,j+1)-Mean2;
end
zero=zeros();
Padzero=150;    %padded zeros to remove the phase between wireless and resistance
for h=1:size(Res1,1)
    for g=1:size(Res1,2)
        if h<=Padzero
            zero(h,g)=0;
        end
        zero(h+Padzero,g)=Res1(h,g);
    end
end
%--------------------------------------------------------------------------
```

```
P2=[Wls1,Res1];     %Data accomodated for Analisys
P3=[P2(:,1:3),P2(:,6),P2(:,5),P2(:,4),P2(:,7),zero(1:size(Res1,1),:)];

tic
scrsz = [1 1 1280 1024];
figure('Position',[1 1 scrsz(3) scrsz(4)])

sa=1:50:(longi/(1/fs));       %Array indicating the snapshots for DDDA calculations******
DOA=zeros(1,size(sa,2));

for SigCal=1:size(sa,2)
%-------------------------------------------------------------------------
%DDDA BEAMFORMER SPECTRUM CALCULATION
%-------------------------------------------------------------------------
teta1=(-180:5:180)*pi/180; % Array with angles in rad for calculation
d=0.48;                     % Sensor separation (m)
X=P3';                      % Transpose of the final data for calculations
%_________________________________________________________________________
% Finding vectors for look direction of the beamformer
AA=zeros(nos,size(teta1,2));
for q=1:size(teta1,2)
    for v=1:size(k,2)
        AA(:,q,v)=manifold3(teta1(q),k(v),d);
    end
end
%_________________________________________________________________________
% Finding pseudo-covariance matrix of the input X
m=(nos+1)/2;
count=0;
Xs=zeros(m,m);
for kk=1:m
    for ii=1:m
        Xs(ii,kk)=X(ii+count,sa(SigCal));
    end
    count=count+1;
end
%_________________________________________________________________________
% Finding the Look constraint generator S(o)
a=zeros();
count=0;
for kk=1:m
    for ii=1:m
        for nn=1:size(teta1,2)
            for v=1:size(k,2)
                A(:,:)=AA(:,:,v);
                a(ii,kk,nn,v)=A(ii+count,nn);
            end
        end
    end
    count=count+1;
end
%_________________________________________________________________________
% Eigenvectors and eigen values calculation
Us=zeros(m,m,size(teta1,2));
Ss=zeros(m,m,size(teta1,2));
for v=1:size(k,2)
    for g=1:size(teta1,2)
        [U S]=eig(Xs,a(:,:,g,v));
        Us(:,:,g,v)=U(:,:);
        Ss(:,:,g,v)=S(:,:);
    end
end
%_________________________________________________________________________
% Identifying the index of the smallest eigenvalue to separate the
% eigenvector that corresponds to that eigevalue
column=zeros(m,size(teta1,2),size(k,2));
eigvindx=zeros(1,size(teta1,2),size(k,2));
```

```
for v=1:size(k,2)
    for g=1:size(teta1,2)
        [im,jm]=sort(abs(diag(Ss(:,:,g,v))));
        column(:,g,v)=jm(:,:);
    end
    eigvindx(1,:,v)=column(1,:,v);
end

% Forming the eigenvector matrix corresponding to the smallest eigenvalue
Ueigv=zeros(m,size(teta1,2),size(k,2));
for v=1:size(k,2)
    for g=1:size(teta1,2)
        Ueigv(:,g,v)=Us(:,eigvindx(1,g,v),g,v);
    end
end
%_____________________________________________________________________
%Creating the weigth vectors
at=AA(1:m,1:size(teta1,2),1:size(k,2));
wt(1:m,1:size(teta1,2),1:size(k,2))=0;
for nn=1:size(teta1,2)
    for v=1:size(k,2)
        wt(:,nn,v)=Ueigv(:,nn,v)/((Ueigv(:,nn,v).')*at(:,nn,v));
    end
end
%_____________________________________________________________________
%Calculating the output of the array y(k)
K=5;                %Number of snapshots to calculate the output power array****
Yk=zeros(size(teta1,2),size(k,2),K);
Ps=zeros(size(teta1,2),size(k,2),K);
for b=1:K
    for v=1:size(k,2)
        for q=1:size(teta1,2)
            Yk(q,v,b)=(wt(:,q,v)')*X(1:m,b+sa(SigCal)-1);
            Ps(q,v,b)=Yk(q,v,b)*conj(Yk(q,v,b));
        end
    end
end
Pb=zeros(size(teta1,2),1);
for q=1:size(teta1,2)
    Pb(q)=sum((1/K)*sum(Ps(q,:,:)));    %Output Power Array
end
%_____________________________________________________________________
teta2=(-180:0.05:180)*pi/180;  % Array with angles in rad for calculation
teta22=(-180:0.05:180);        % Array with angles in degrees for plotting
[Tmin,Tcol]=sort(Pb);
Tmincol=Tcol(1);
%_____________________________________________________________________
% Finding vectors for look direction of the beamformer for the best
% resolution plot, using a Normalized Directional Spectrum
Aa=zeros(nos,size(teta2,2));
for q=1:size(teta2,2)
    for v=1:size(k,2)
        Aa(:,q,v)=manifold3(teta2(q),k(v),d);
    end
end
%_____________________________________________________________________
Pd=zeros(size(teta2,2),1);
for f=1:size(wt,3)
    for q=1:size(teta2,2)
        Pd(q)=Pd(q)+10*log10(1/abs((wt(:,Tmincol,f).')*Aa(1:m,q,f))^2); %Normalized
Directional Spectrum
    end
end
[Max,Maxcol]=max(Pd(1800:5400));
DOA(SigCal)=abs(((Maxcol-2)*0.05)-90);  %DOA from the calculation using DDDA
```

```
%_____________________________________
%ARRAY MANIFOLD ("Steering vector")
%_____________________________________

function a = manifold3(angle,k,d)
global nos
no=nos;
a=zeros();
for N=1:no
    a(N,1)=exp(j.*(N-1).*k.*d.*sin(angle));
end
```

APPENDIX B

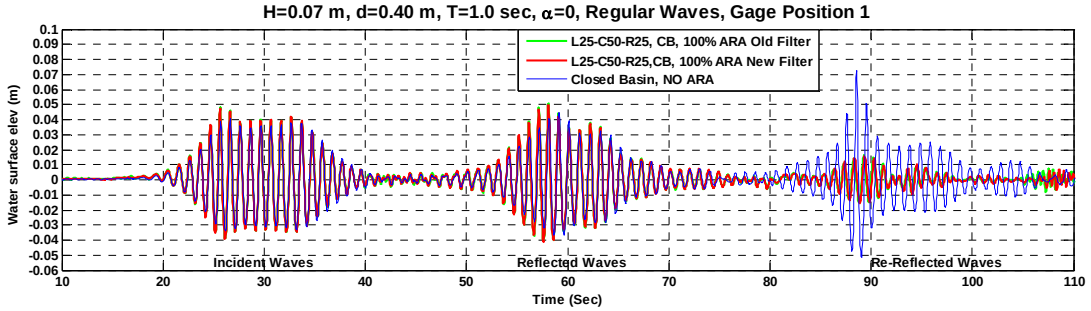
H=0.07 m, d=0.40 m, T=1.0 sec, α=0, Regular Waves, Gage Position 1
L25-C50-R25, CB, 100% ARA Old Filter
L25-C50-R25,CB, 100% ARA New Filter
Closed Basin, NO ARA
Water surface elev (m)
Time (Sec)
Incident Waves
Reflected Waves
Re-Reflected Waves

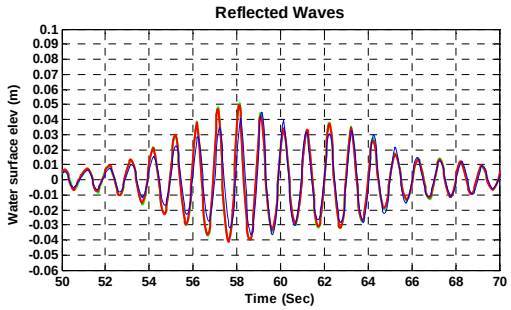
Reflected Waves
Water surface elev (m)
Time (Sec)

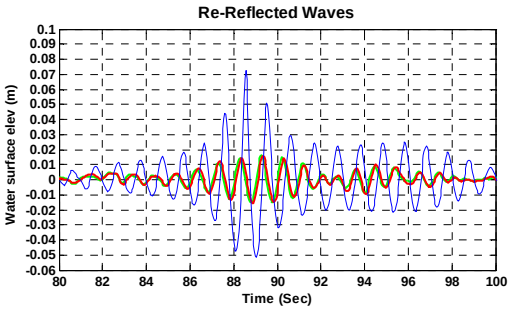
Re-Reflected Waves
Water surface elev (m)
Time (Sec)

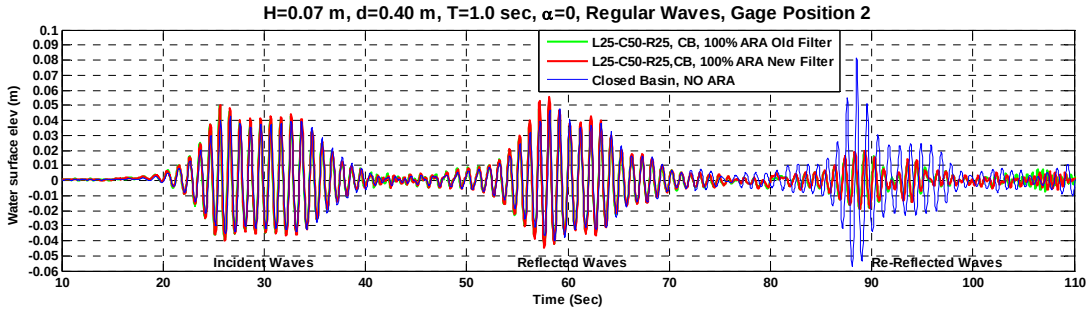
H=0.07 m, d=0.40 m, T=1.0 sec, α=0, Regular Waves, Gage Position 2
L25-C50-R25, CB, 100% ARA Old Filter
L25-C50-R25,CB, 100% ARA New Filter
Closed Basin, NO ARA
Water surface elev (m)
Time (Sec)
Incident Waves
Reflected Waves
Re-Reflected Waves

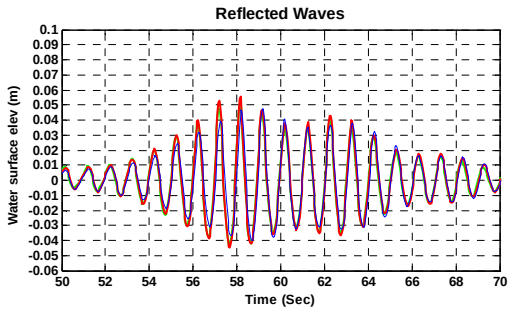
Reflected Waves
Water surface elev (m)
Time (Sec)

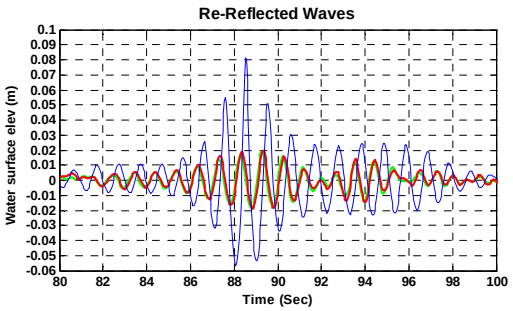
Re-Reflected Waves
Water surface elev (m)
Time (Sec)

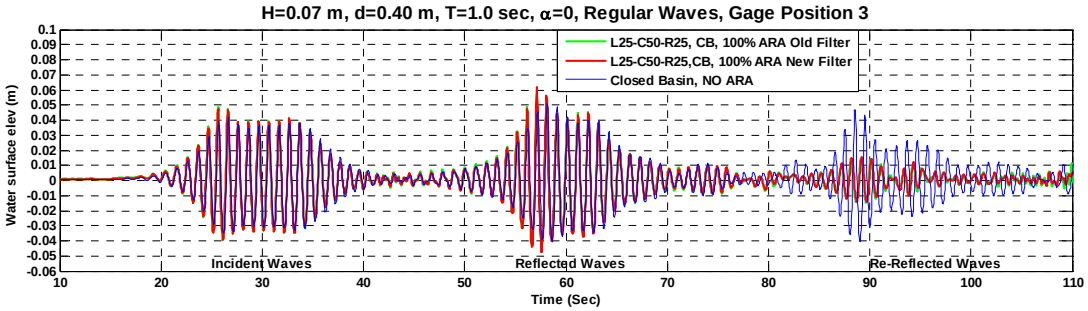
H=0.07 m, d=0.40 m, T=1.0 sec, α=0, Regular Waves, Gage Position 3
L25-C50-R25, CB, 100% ARA Old Filter
L25-C50-R25,CB, 100% ARA New Filter
Closed Basin, NO ARA
Water surface elev (m)
Time (Sec)
Incident Waves
Reflected Waves
Re-Reflected Waves

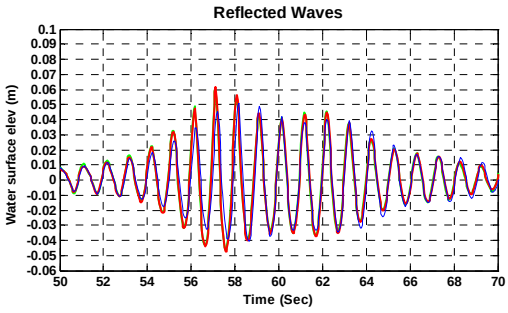
Reflected Waves
Water surface elev (m)
Time (Sec)

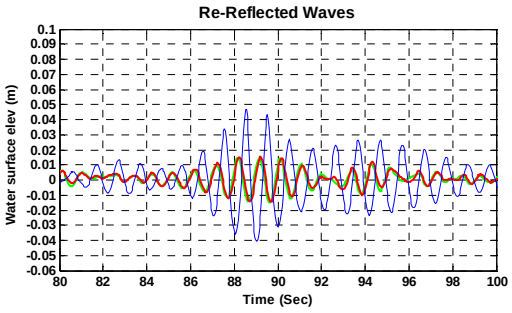
Re-Reflected Waves
Water surface elev (m)
Time (Sec)

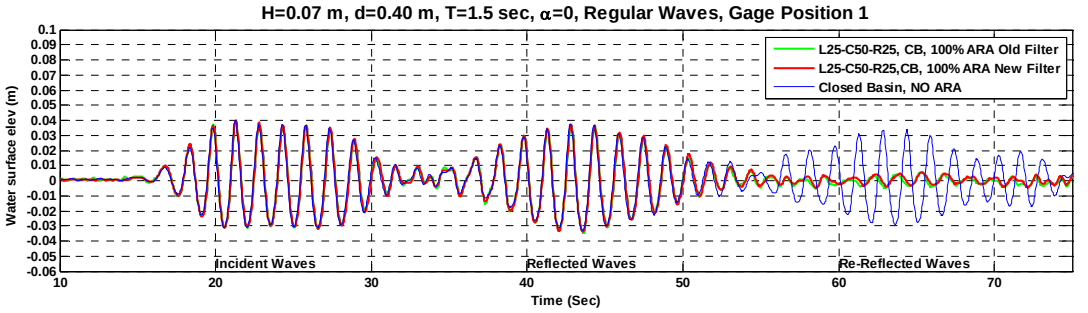
H=0.07 m, d=0.40 m, T=1.5 sec, α=0, Regular Waves, Gage Position 1
L25-C50-R25, CB, 100% ARA Old Filter
L25-C50-R25,CB, 100% ARA New Filter
Closed Basin, NO ARA
Water surface elev (m)
Time (Sec)
Incident Waves
Reflected Waves
Re-Reflected Waves

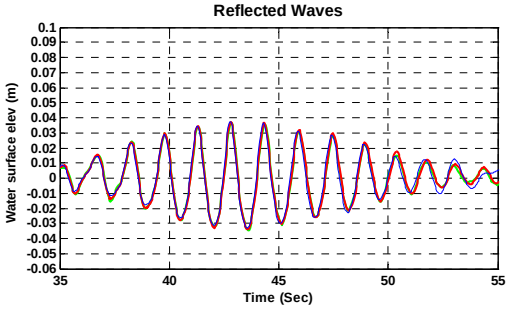
Reflected Waves
Water surface elev (m)
Time (Sec)

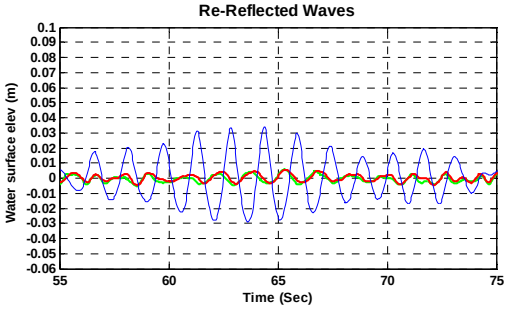
Re-Reflected Waves
Water surface elev (m)
Time (Sec)

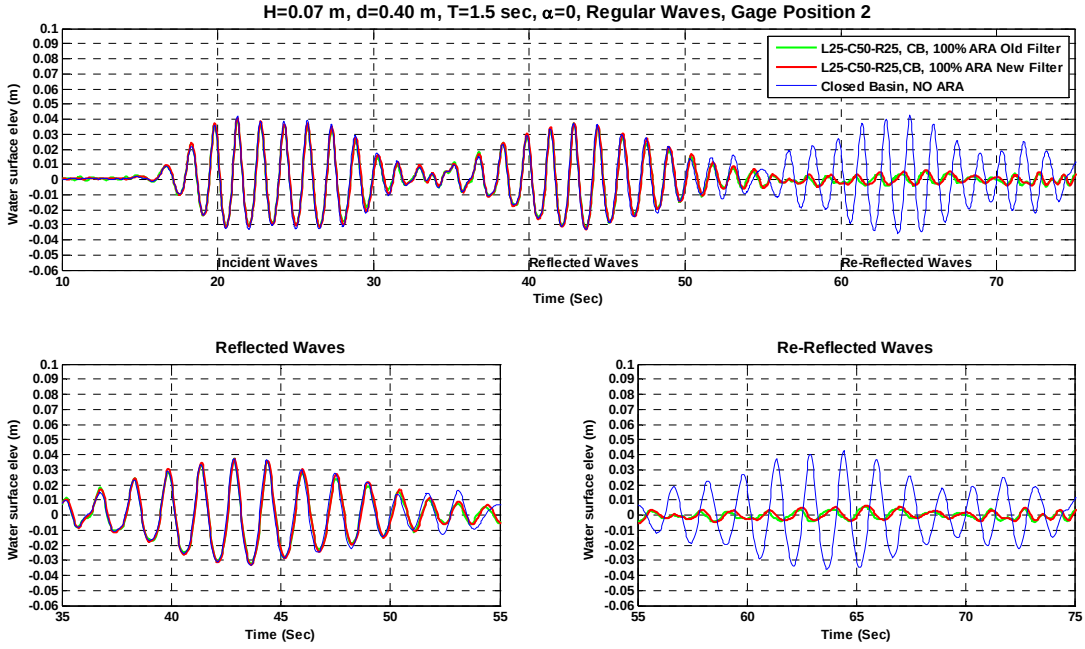
H=0.07 m, d=0.40 m, T=1.5 sec, α=0, Regular Waves, Gage Position 2
L25-C50-R25, CB, 100% ARA Old Filter
L25-C50-R25,CB, 100% ARA New Filter
Closed Basin, NO ARA
Incident Waves
Reflected Waves
Re-Reflected Waves
Water surface elev (m)
Time (Sec)
Reflected Waves
Water surface elev (m)
Time (Sec)
Re-Reflected Waves
Water surface elev (m)
Time (Sec)

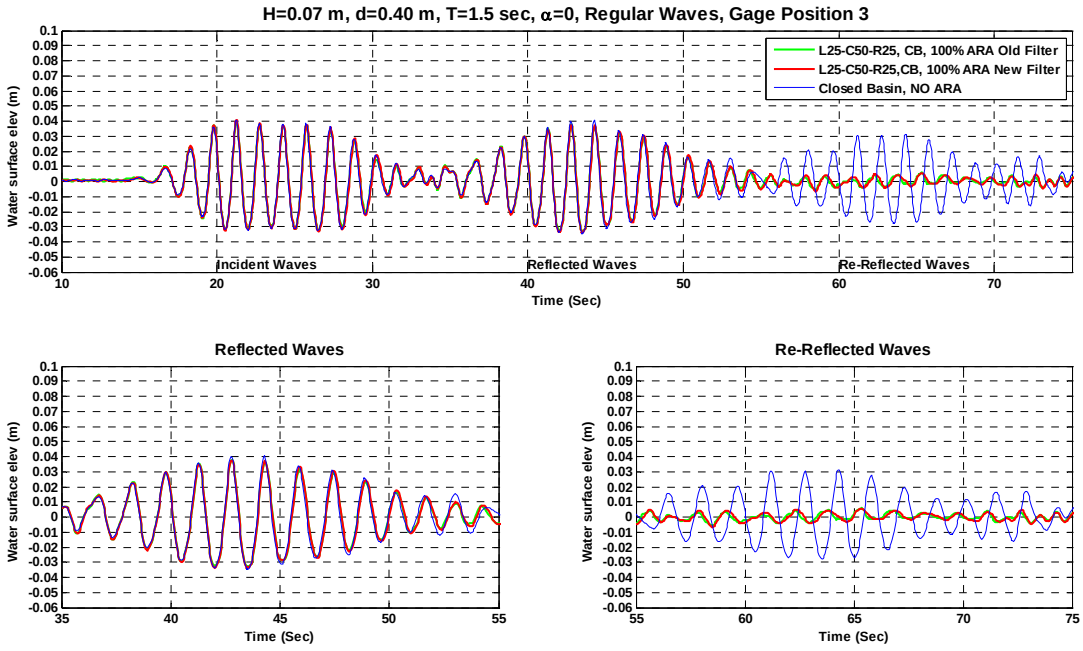
H=0.07 m, d=0.40 m, T=1.5 sec, α=0, Regular Waves, Gage Position 3
L25-C50-R25, CB, 100% ARA Old Filter
L25-C50-R25,CB, 100% ARA New Filter
Closed Basin, NO ARA
Incident Waves
Reflected Waves
Re-Reflected Waves
Water surface elev (m)
Time (Sec)
Reflected Waves
Water surface elev (m)
Time (Sec)
Re-Reflected Waves
Water surface elev (m)
Time (Sec)

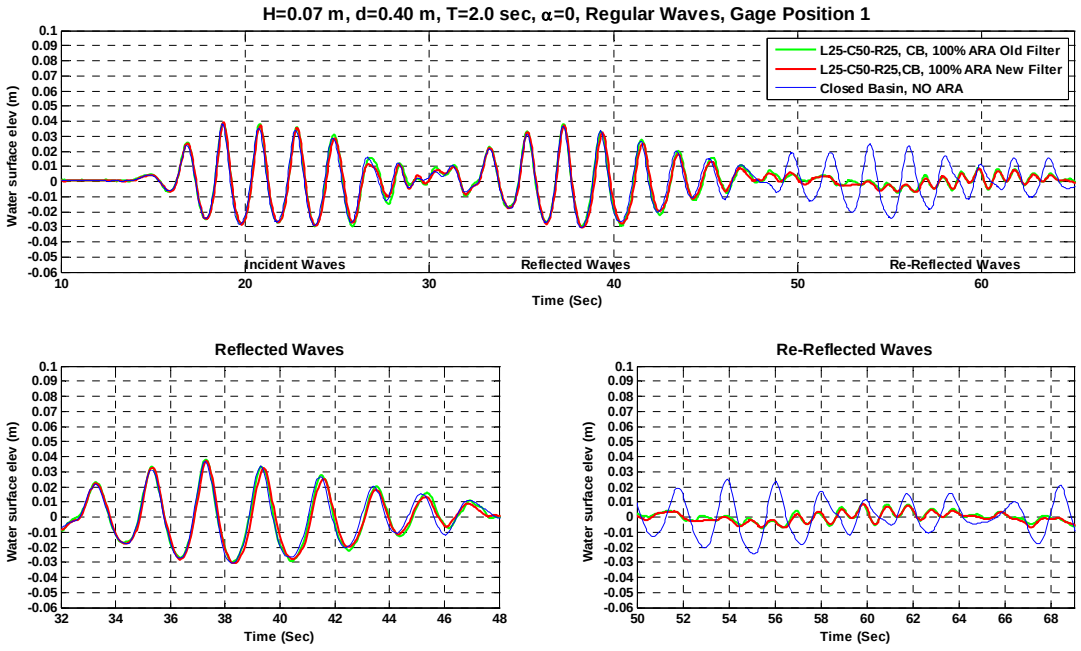
H=0.07 m, d=0.40 m, T=2.0 sec, α=0, Regular Waves, Gage Position 1
L25-C50-R25, CB, 100% ARA Old Filter
L25-C50-R25,CB, 100% ARA New Filter
Closed Basin, NO ARA
Water surface elev (m)
Incident Waves
Reflected Waves
Re-Reflected Waves
Time (Sec)
Reflected Waves
Water surface elev (m)
Time (Sec)
Re-Reflected Waves
Water surface elev (m)
Time (Sec)

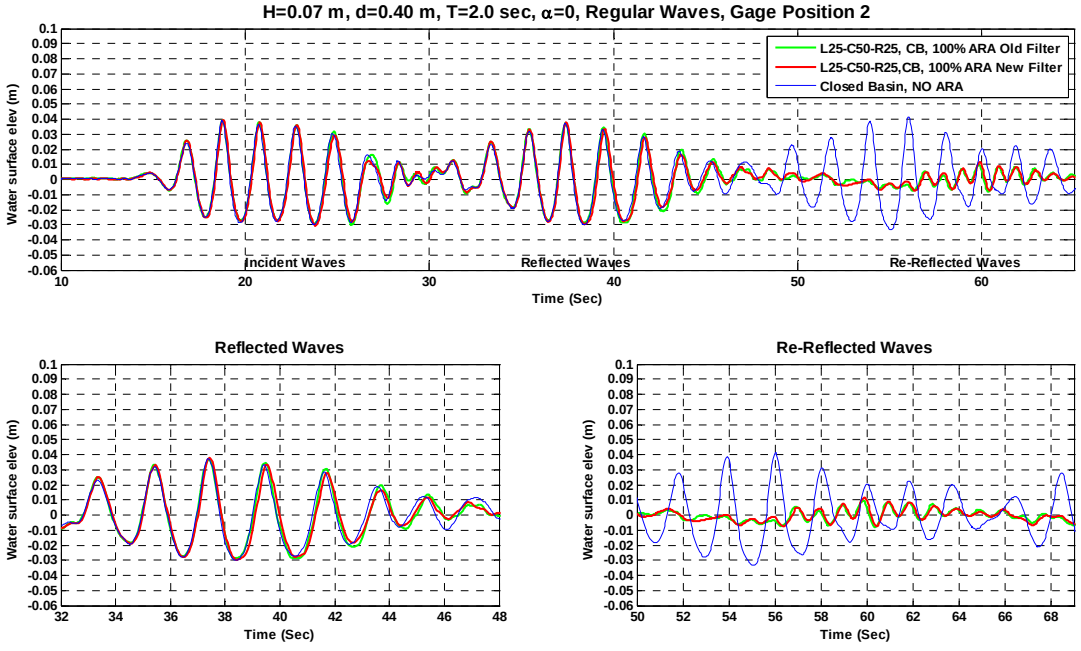
H=0.07 m, d=0.40 m, T=2.0 sec, α=0, Regular Waves, Gage Position 2
L25-C50-R25, CB, 100% ARA Old Filter
L25-C50-R25,CB, 100% ARA New Filter
Closed Basin, NO ARA
Water surface elev (m)
Incident Waves
Reflected Waves
Re-Reflected Waves
Time (Sec)
Reflected Waves
Water surface elev (m)
Time (Sec)
Re-Reflected Waves
Water surface elev (m)
Time (Sec)

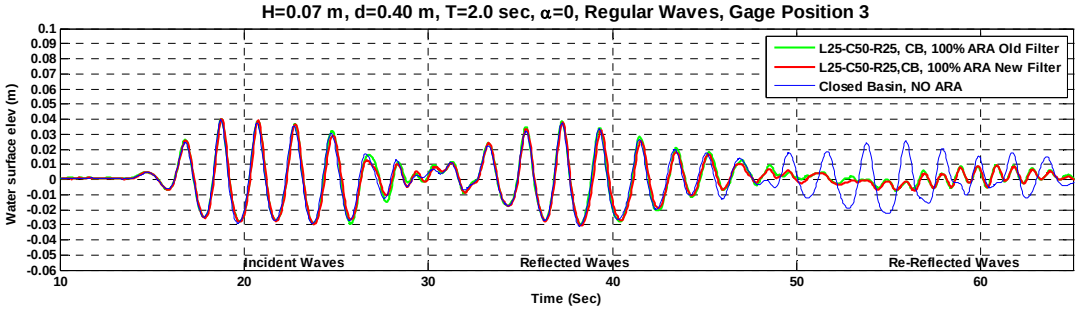
H=0.07 m, d=0.40 m, T=2.0 sec, α=0, Regular Waves, Gage Position 3
L25-C50-R25, CB, 100% ARA Old Filter
L25-C50-R25,CB, 100% ARA New Filter
Closed Basin, NO ARA
Incident Waves
Reflected Waves
Re-Reflected Waves
Water surface elev (m)
Time (Sec)

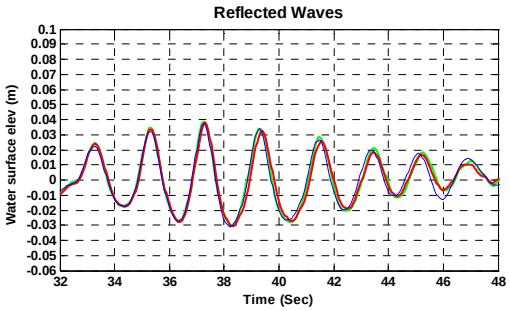
Reflected Waves
Water surface elev (m)
Time (Sec)

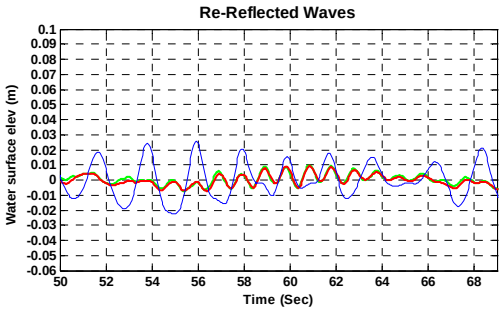
Re-Reflected Waves
Water surface elev (m)
Time (Sec)

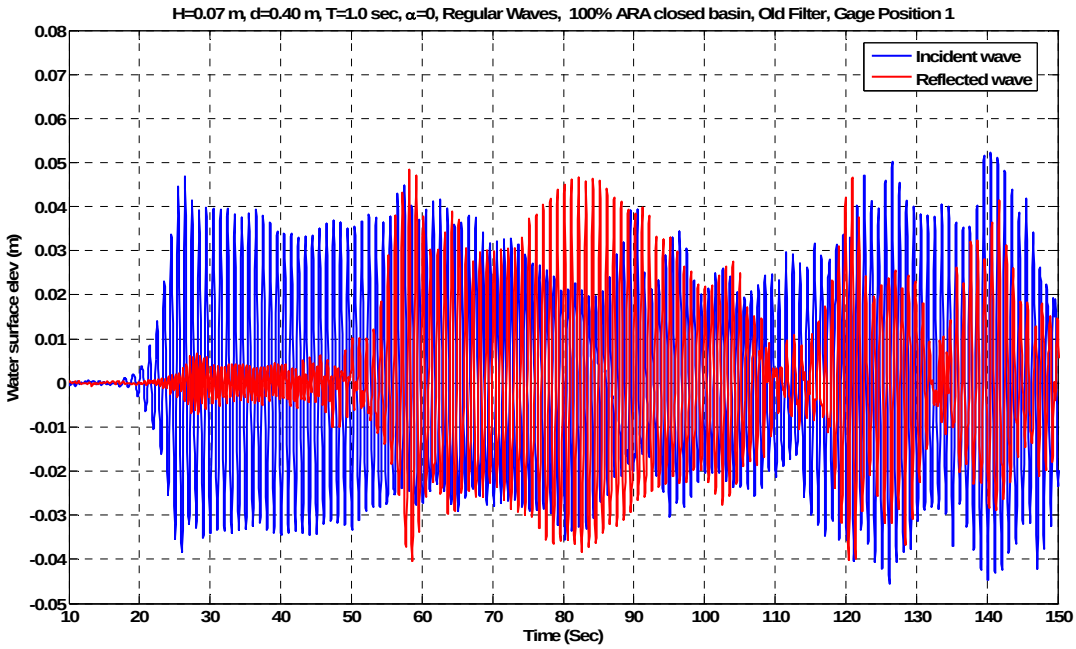
H=0.07 m, d=0.40 m, T=1.0 sec, α=0, Regular Waves, 100% ARA closed basin, Old Filter, Gage Position 1
Incident wave
Reflected wave
Water surface elev (m)
Time (Sec)

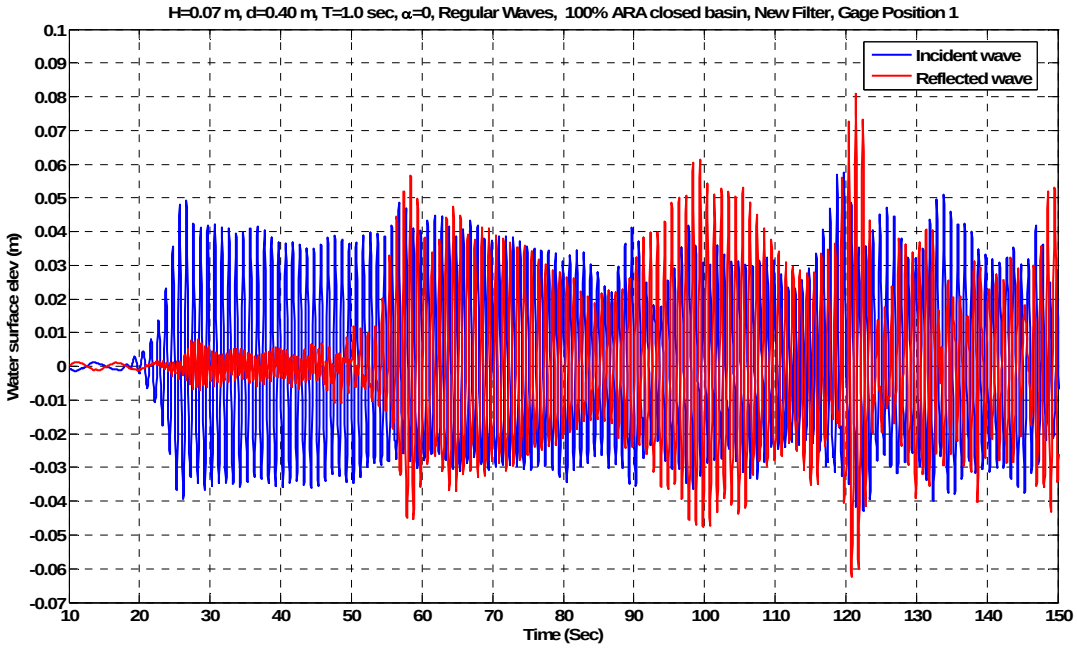
H=0.07 m, d=0.40 m, T=1.0 sec, α=0, Regular Waves, 100% ARA closed basin, New Filter, Gage Position 1
Incident wave
Reflected wave
Water surface elev (m)
Time (Sec)

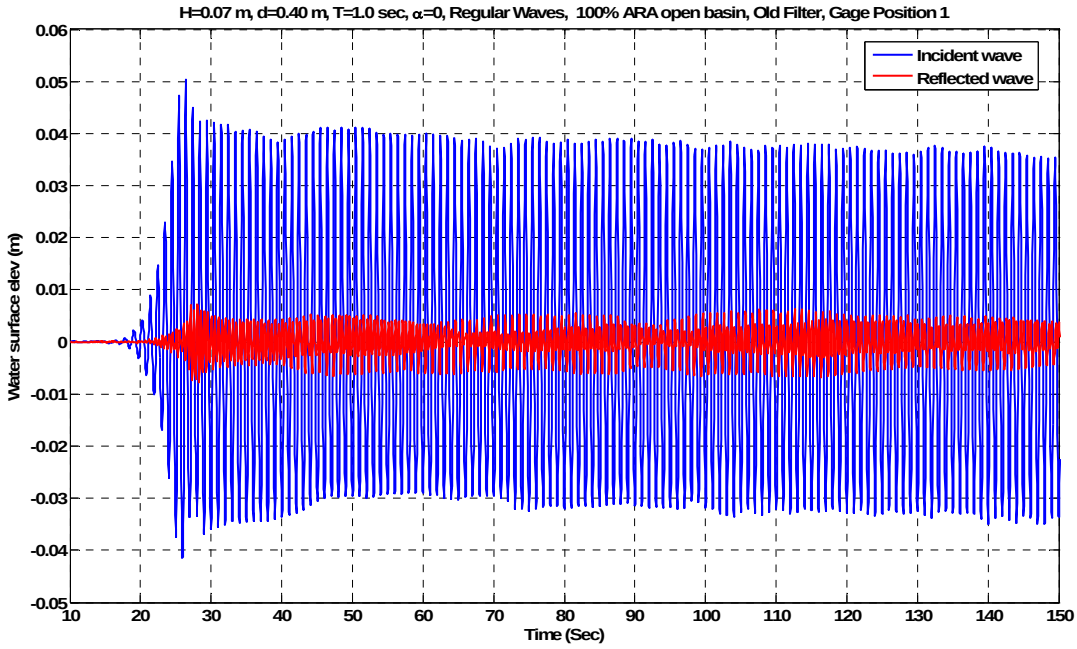
H=0.07 m, d=0.40 m, T=1.0 sec, α=0, Regular Waves, 100% ARA open basin, Old Filter, Gage Position 1
Incident wave
Reflected wave
Water surface elev (m)
Time (Sec)

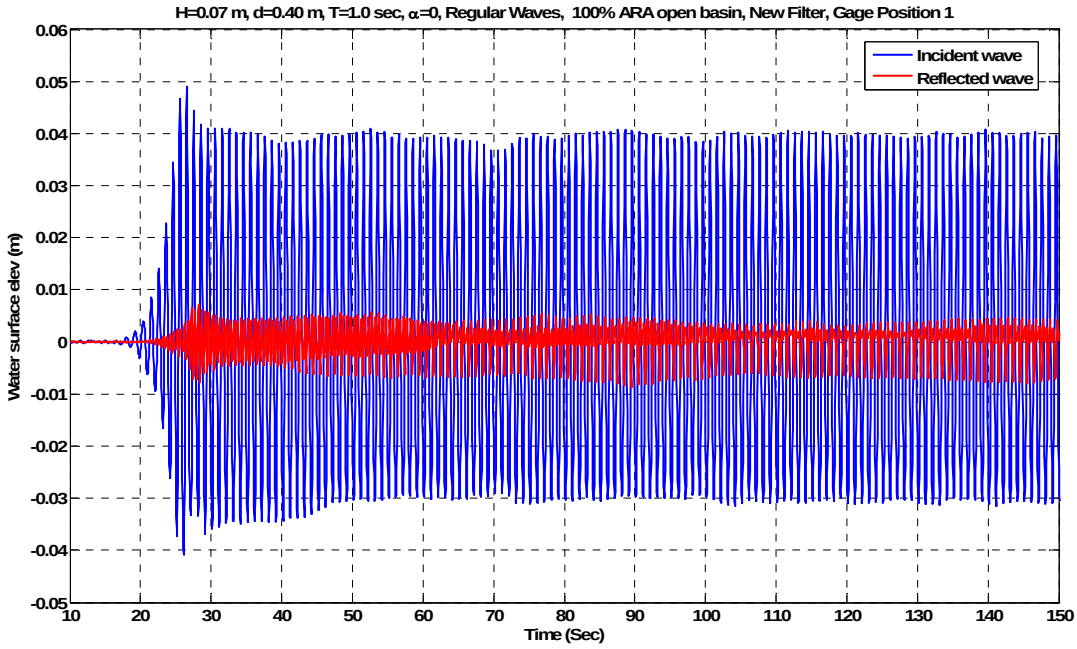
H=0.07 m, d=0.40 m, T=1.0 sec, α=0, Regular Waves, 100% ARA open basin, New Filter, Gage Position 1
Incident wave
Reflected wave
Water surface elev (m)
Time (Sec)
0.06
0.05
0.04
0.03
0.02
0.01
0
-0.01
-0.02
-0.03
-0.04
-0.05
10
20
30
40
50
60
70
80
90
100
110
120
130
140
150

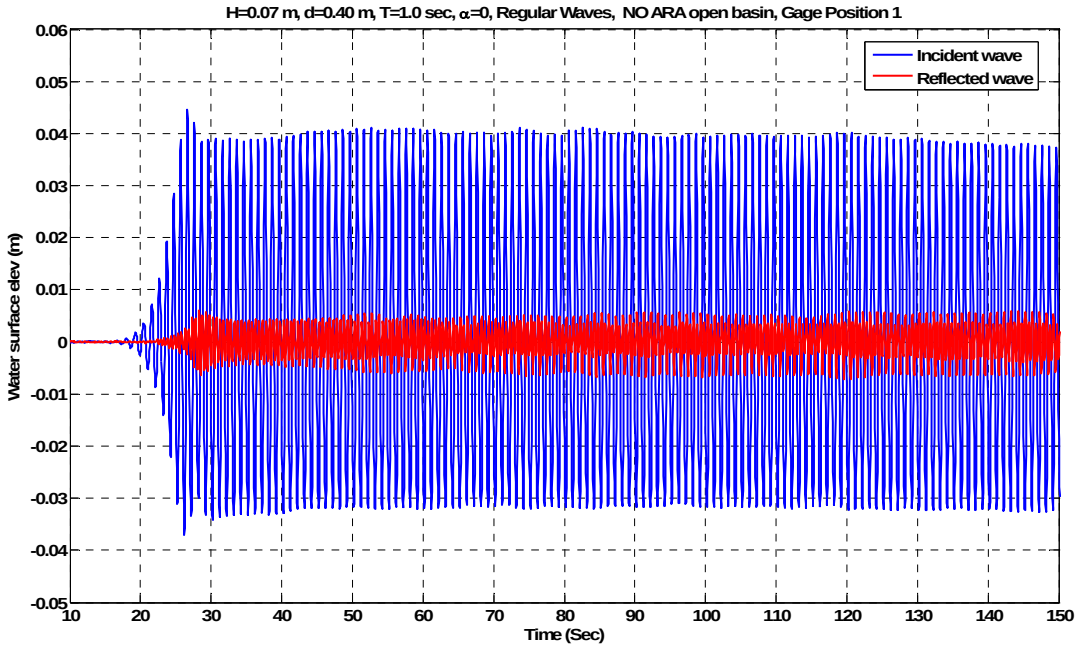
H=0.07 m, d=0.40 m, T=1.0 sec, α=0, Regular Waves, NO ARA open basin, Gage Position 1
Incident wave
Reflected wave
Water surface elev (m)
Time (Sec)
0.06
0.05
0.04
0.03
0.02
0.01
0
-0.01
-0.02
-0.03
-0.04
-0.05
10
20
30
40
50
60
70
80
90
100
110
120
130
140
150

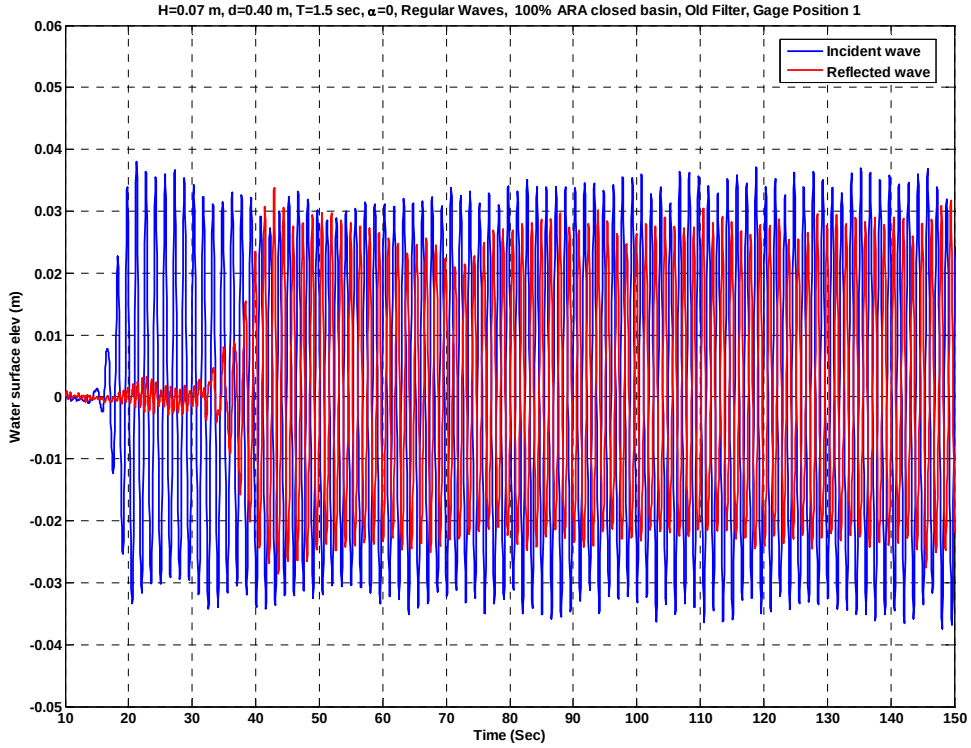
H=0.07 m, d=0.40 m, T=1.5 sec, α=0, Regular Waves, 100% ARA closed basin, Old Filter, Gage Position 1
Incident wave
Reflected wave
Water surface elev (m)
Time (Sec)

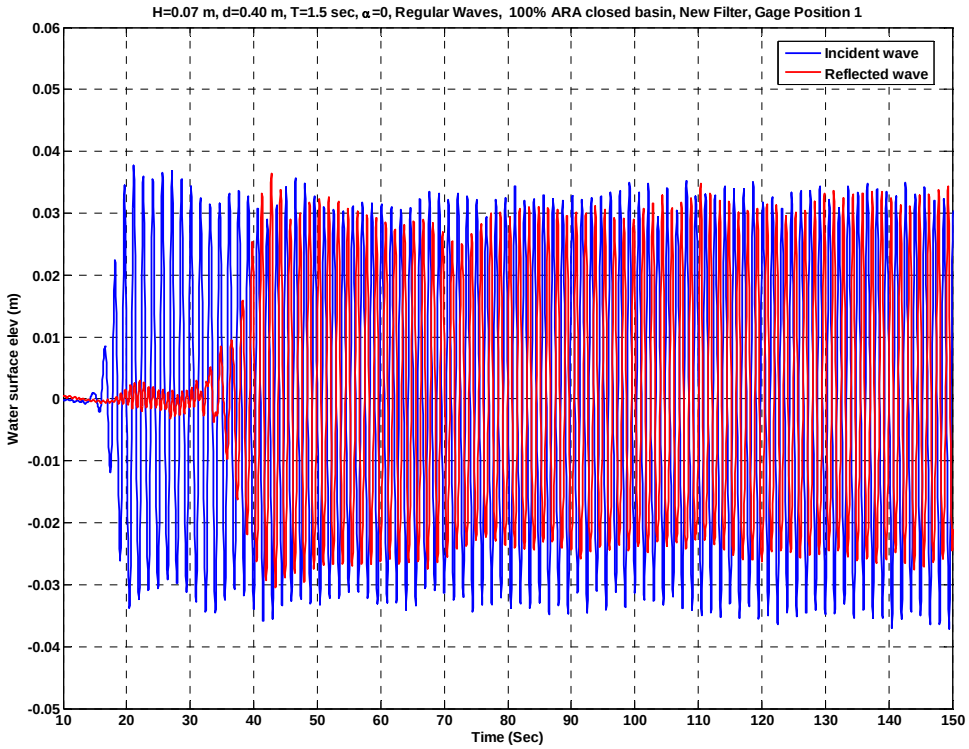
H=0.07 m, d=0.40 m, T=1.5 sec, α=0, Regular Waves, 100% ARA closed basin, New Filter, Gage Position 1
Incident wave
Reflected wave
Water surface elev (m)
Time (Sec)

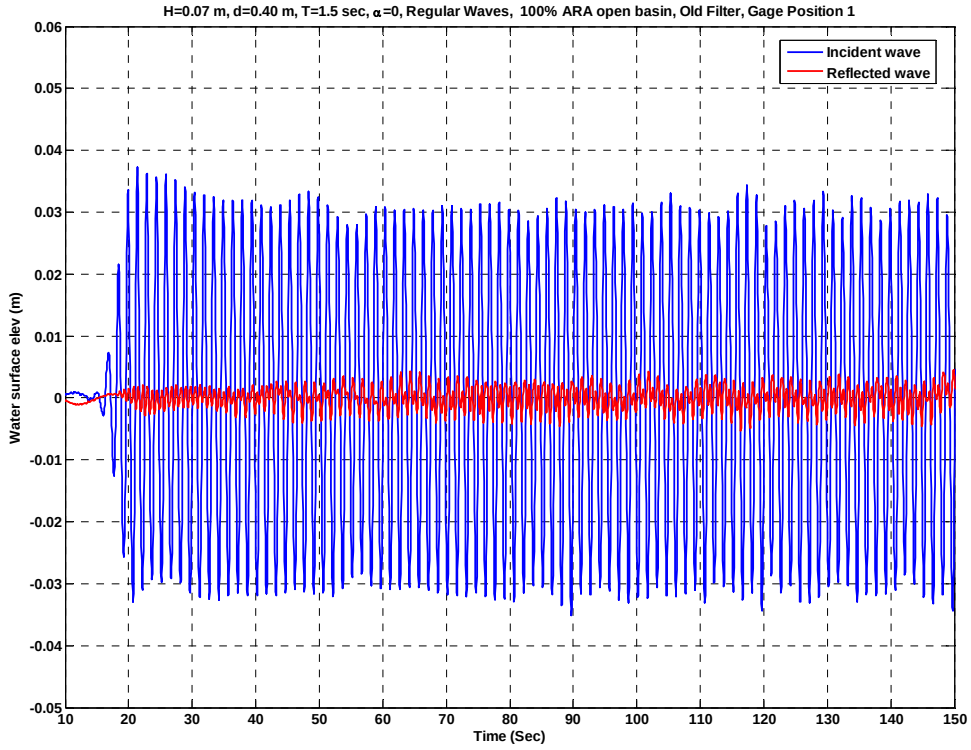
H=0.07 m, d=0.40 m, T=1.5 sec, α=0, Regular Waves, 100% ARA open basin, Old Filter, Gage Position 1
Incident wave
Reflected wave
Water surface elev (m)
Time (Sec)
0.06
0.05
0.04
0.03
0.02
0.01
0
-0.01
-0.02
-0.03
-0.04
-0.05
10
20
30
40
50
60
70
80
90
100
110
120
130
140
150

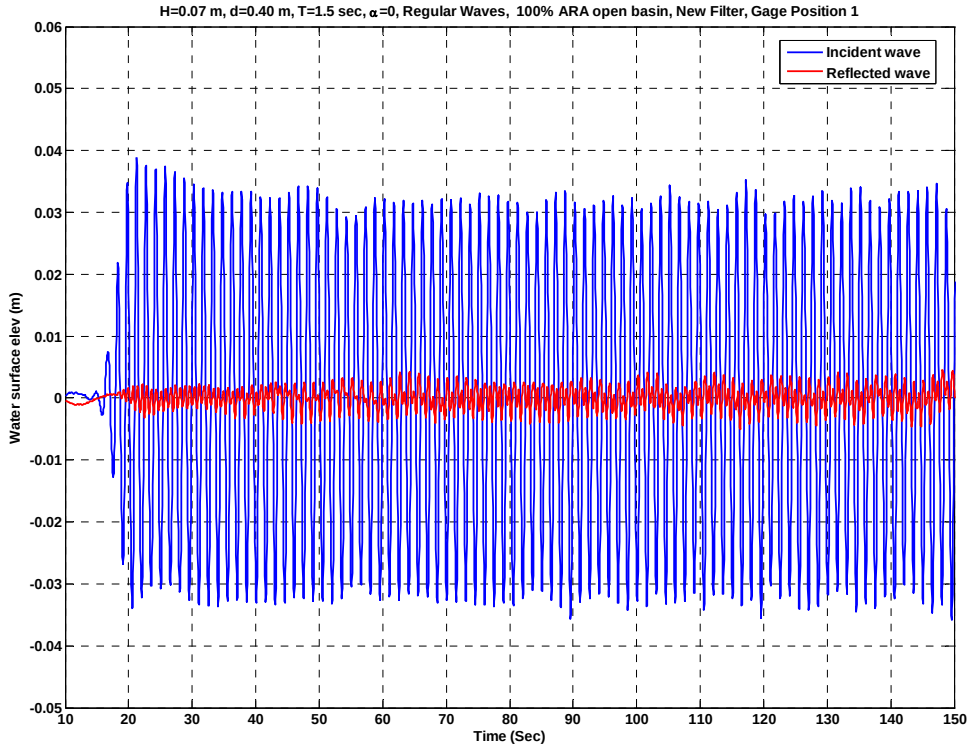
H=0.07 m, d=0.40 m, T=1.5 sec, α=0, Regular Waves, 100% ARA open basin, New Filter, Gage Position 1
Incident wave
Reflected wave
Water surface elev (m)
Time (Sec)
0.06
0.05
0.04
0.03
0.02
0.01
0
-0.01
-0.02
-0.03
-0.04
-0.05
10
20
30
40
50
60
70
80
90
100
110
120
130
140
150

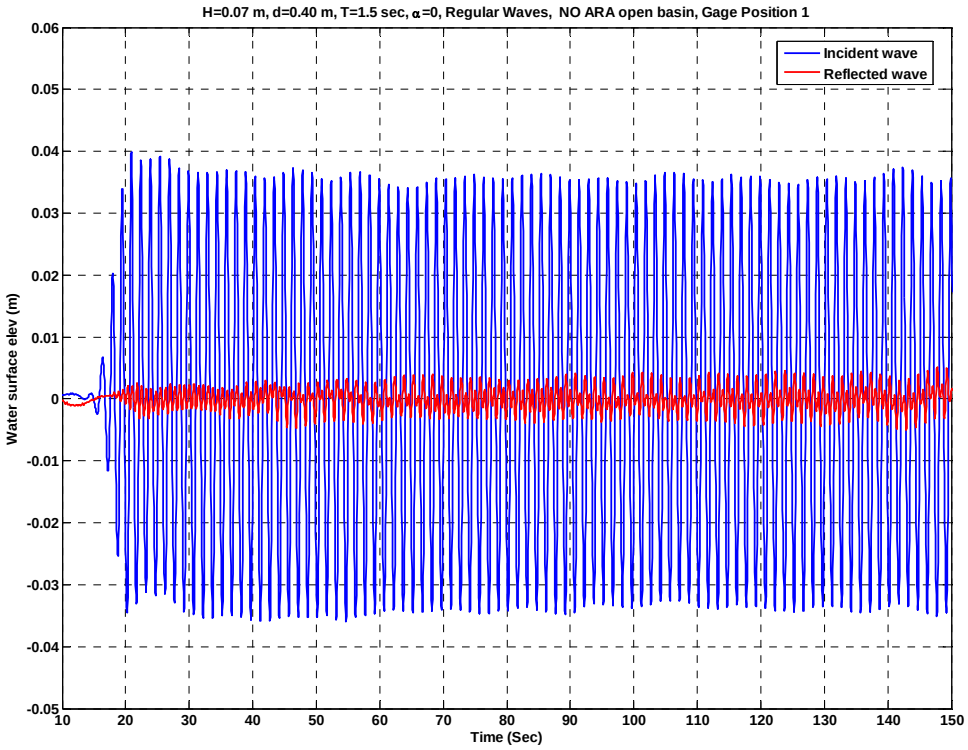
H=0.07 m, d=0.40 m, T=1.5 sec, α=0, Regular Waves, NO ARA open basin, Gage Position 1
Incident wave
Reflected wave
Water surface elev (m)
Time (Sec)

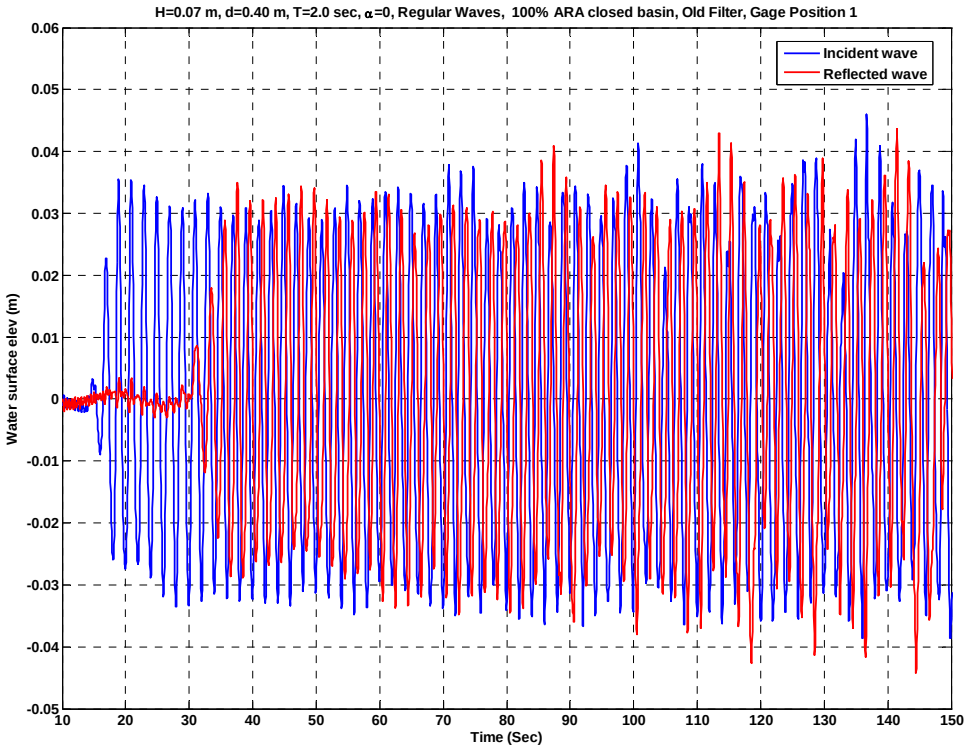
H=0.07 m, d=0.40 m, T=2.0 sec, α=0, Regular Waves, 100% ARA closed basin, Old Filter, Gage Position 1
Incident wave
Reflected wave
Water surface elev (m)
Time (Sec)

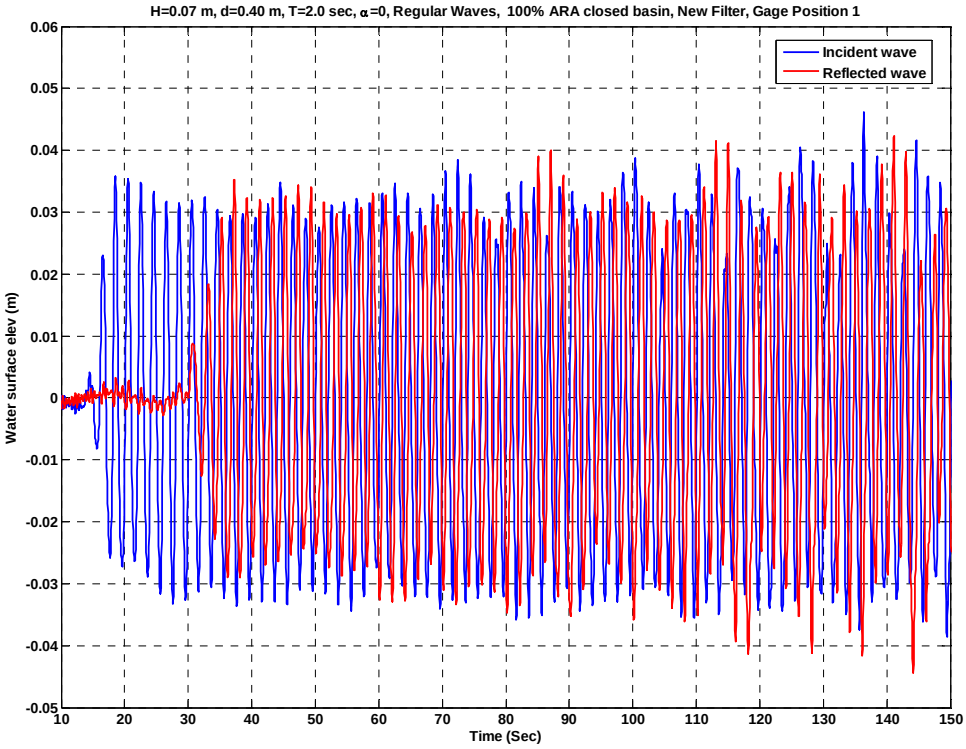
H=0.07 m, d=0.40 m, T=2.0 sec, α=0, Regular Waves, 100% ARA closed basin, New Filter, Gage Position 1
Incident wave
Reflected wave
Water surface elev (m)
Time (Sec)

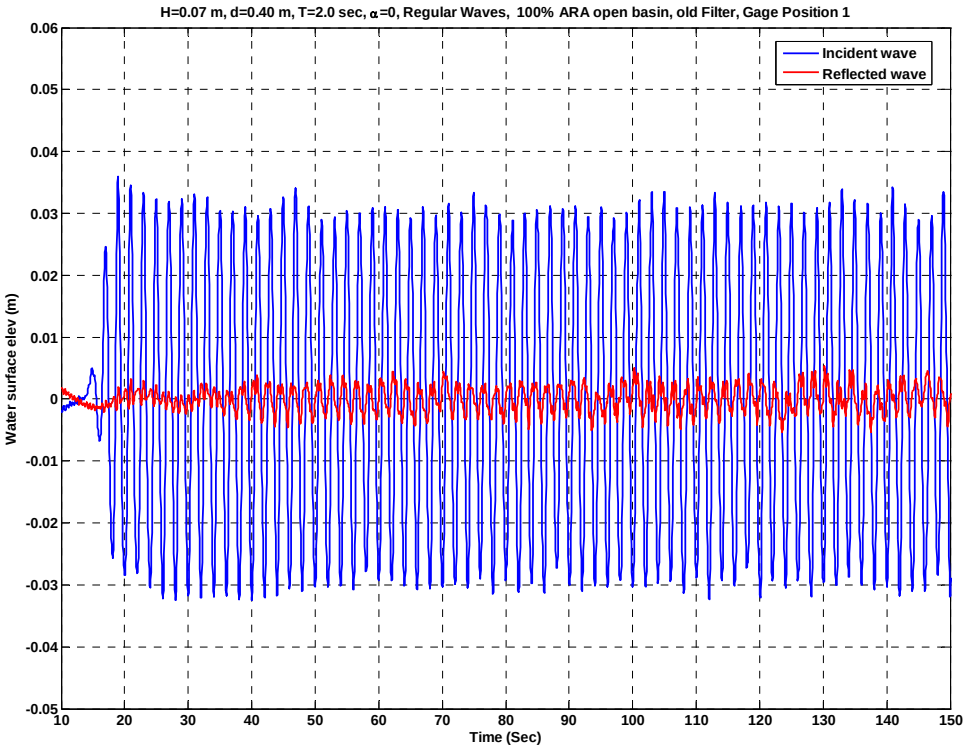
H=0.07 m, d=0.40 m, T=2.0 sec, α=0, Regular Waves, 100% ARA open basin, old Filter, Gage Position 1
Incident wave
Reflected wave
Water surface elev (m)
Time (Sec)

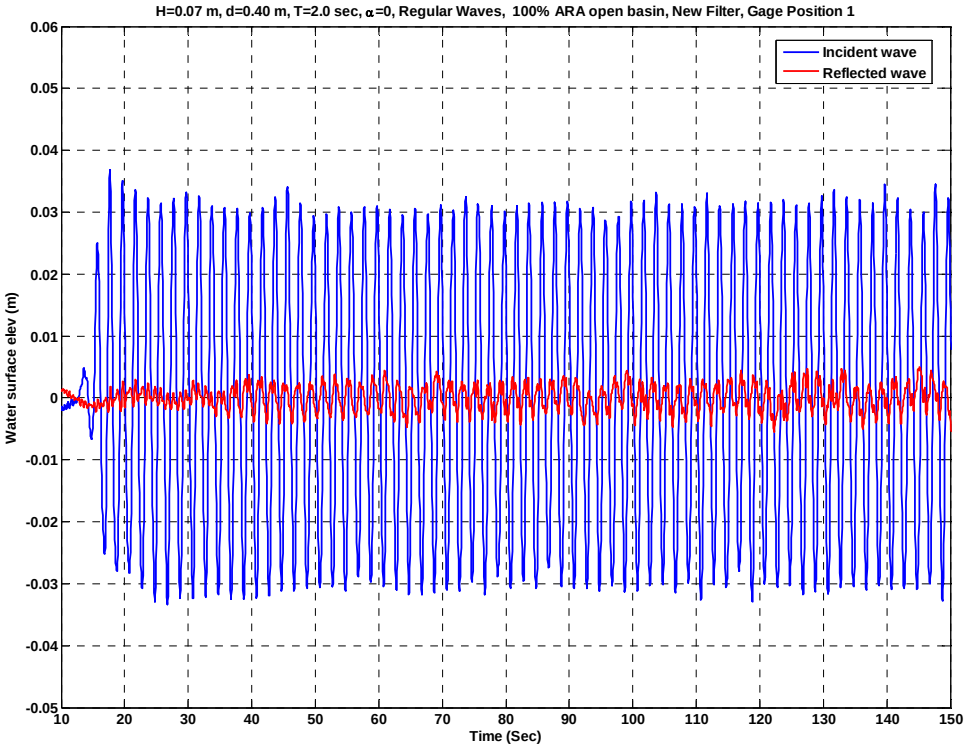
H=0.07 m, d=0.40 m, T=2.0 sec, α=0, Regular Waves, 100% ARA open basin, New Filter, Gage Position 1
Incident wave
Reflected wave
Water surface elev (m)
Time (Sec)

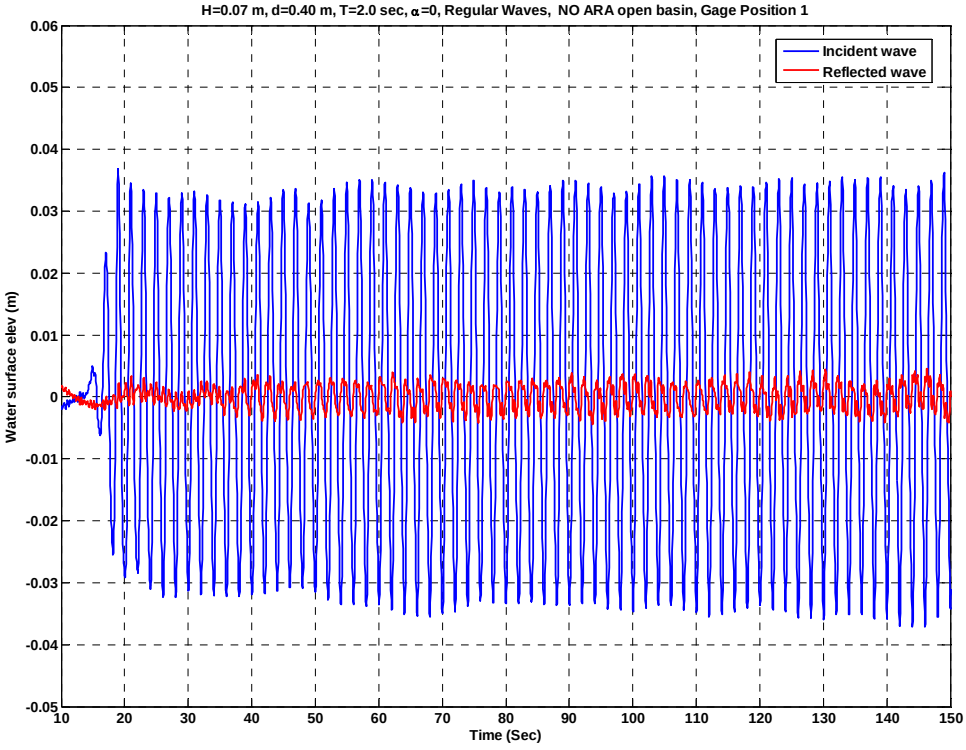
H=0.07 m, d=0.40 m, T=2.0 sec, α=0, Regular Waves, NO ARA open basin, Gage Position 1
Incident wave
Reflected wave
Water surface elev (m)
Time (Sec)

APPENDIX C

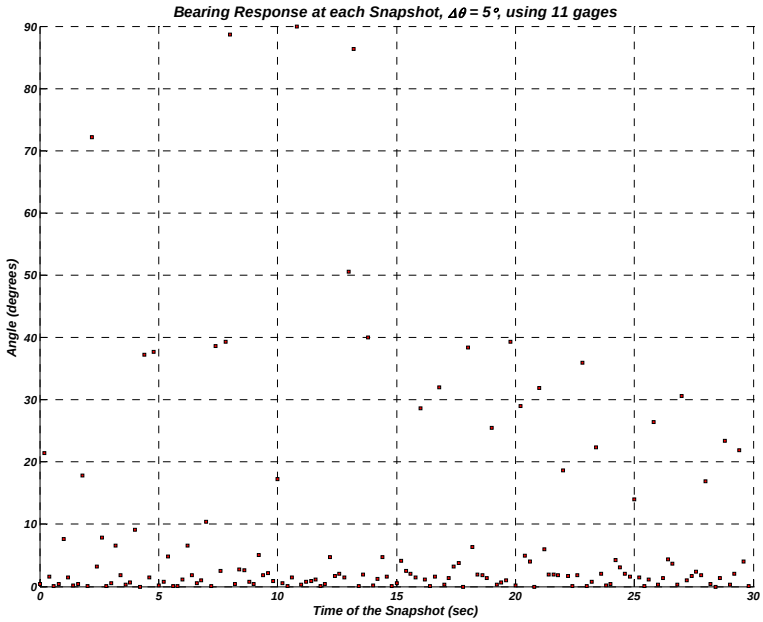

Bearing estimation from wave data: Regular waves, T= 1.50 sec, H= 0.06 m, θ= 0 degrees

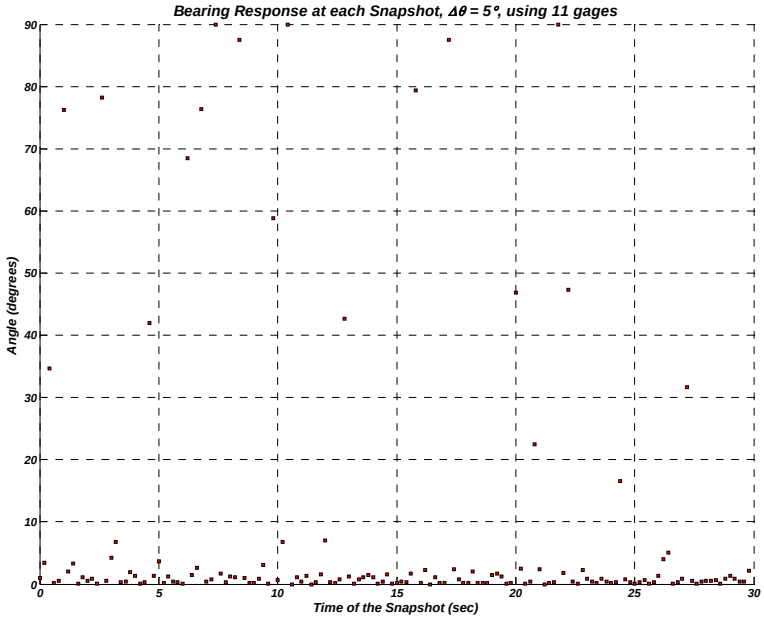

Bearing estimation from wave data: Regular waves, T= 1.80 sec, H= 0.06 m, θ= 0 degrees

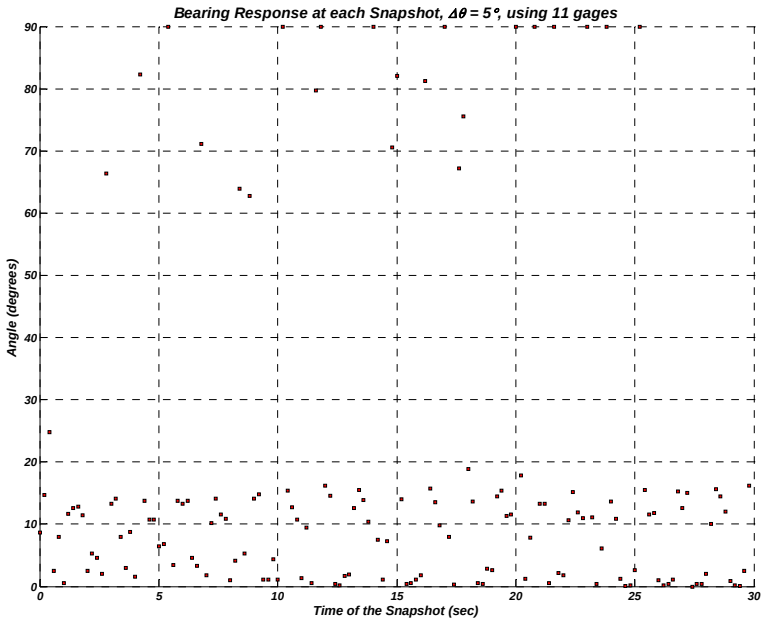

Bearing estimation from wave data: Regular waves, T= 1.50 sec, H= 0.06 m, θ= 10 degrees

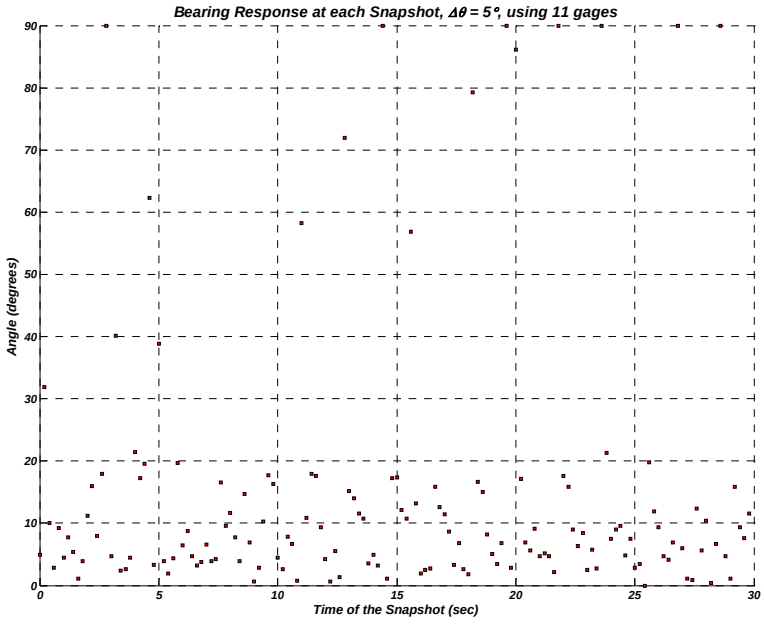

Bearing estimation from wave data: Regular waves, T= 1.80 sec, H= 0.06 m, θ= 10 degrees

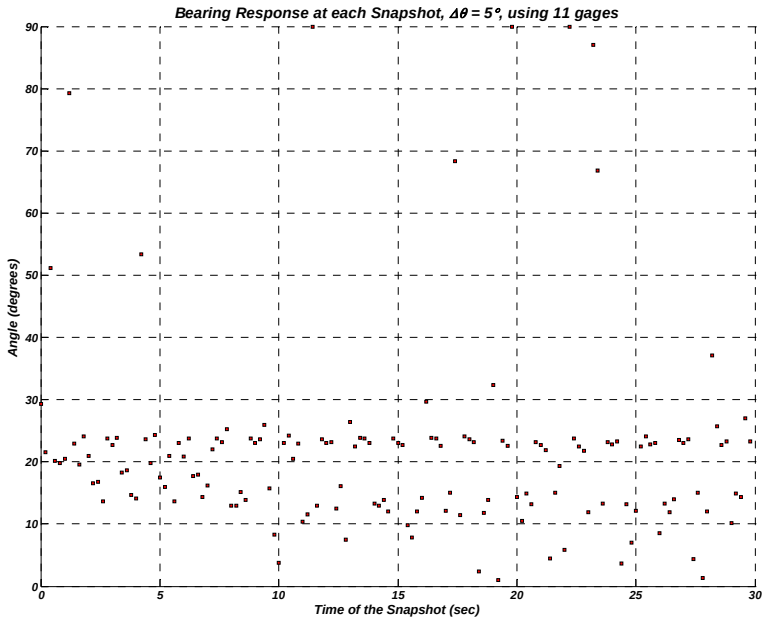

Bearing estimation from wave data: Regular waves, T= 1.50 sec, H= 0.06 m, θ= 20 degrees

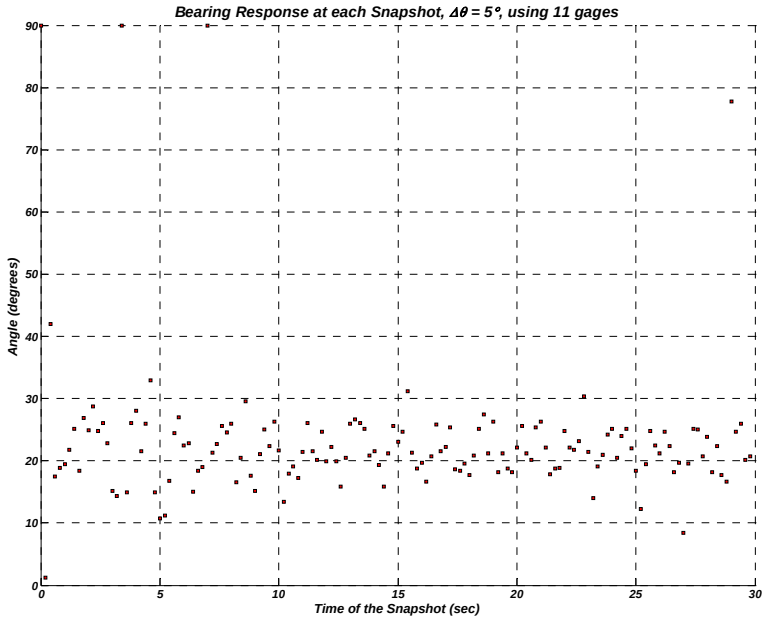

Bearing estimation from wave data: Regular waves, T= 1.80 sec, H= 0.06 m, θ= 20 degrees

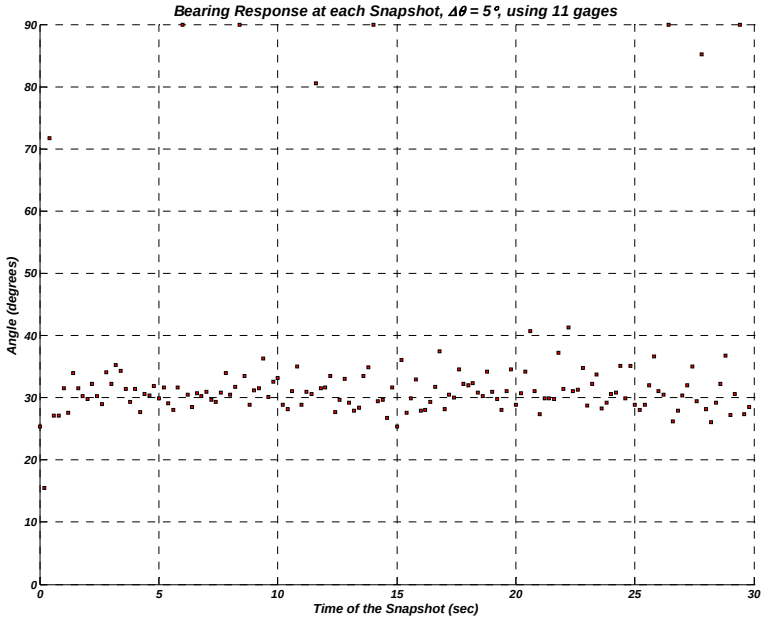

Bearing estimation from wave data: Regular waves, T= 1.50 sec, H= 0.06 m, θ= 30 degrees

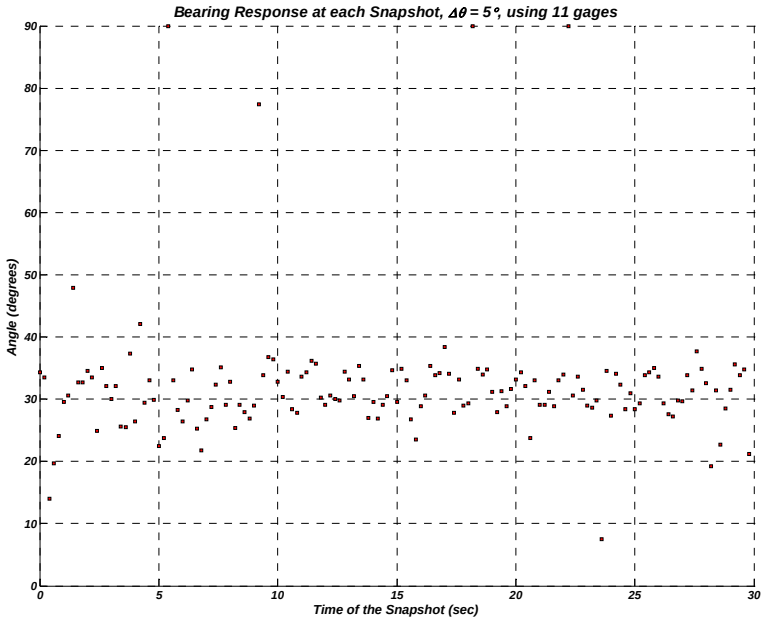

Bearing estimation from wave data: Regular waves, T= 1.80 sec, H= 0.06 m, θ= 30 degrees

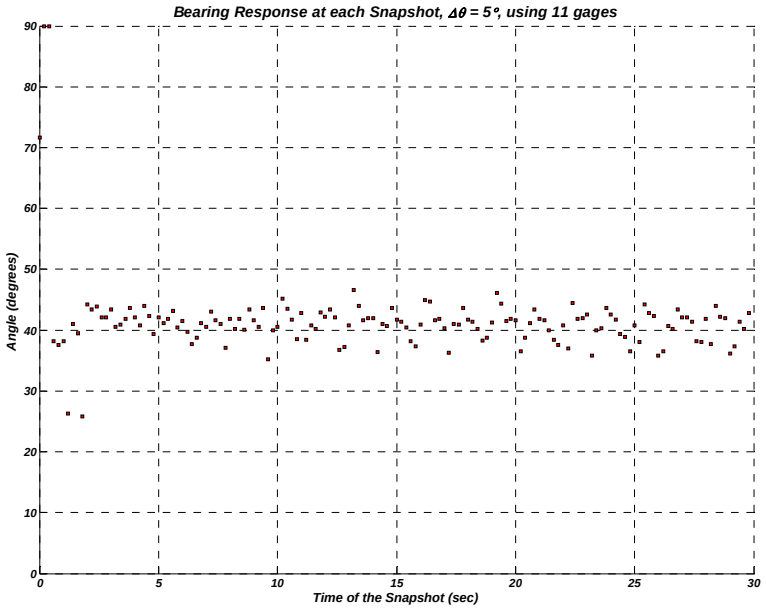

Bearing estimation from wave data: Regular waves, T= 1.50 sec, H= 0.06 m, θ= 40 degrees

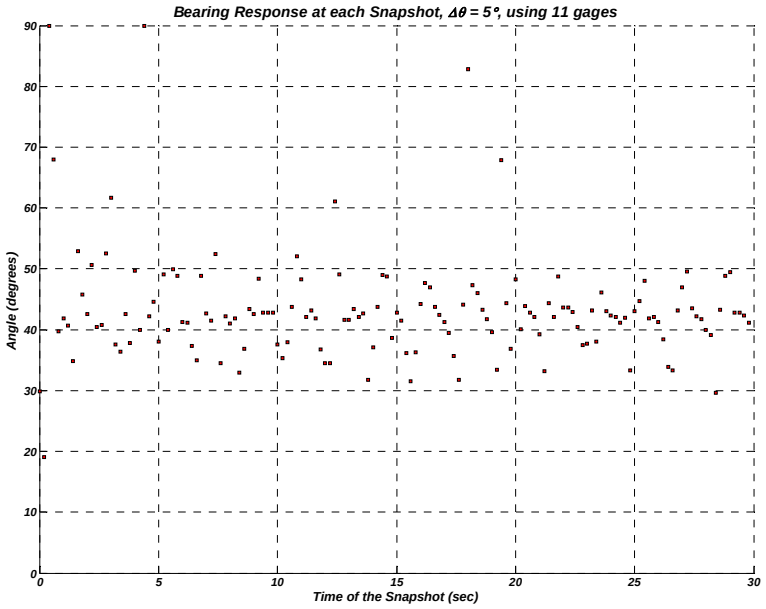

Bearing estimation from wave data: Regular waves, T= 1.80 sec, H= 0.06 m, θ= 40 degrees

APPENDIX D

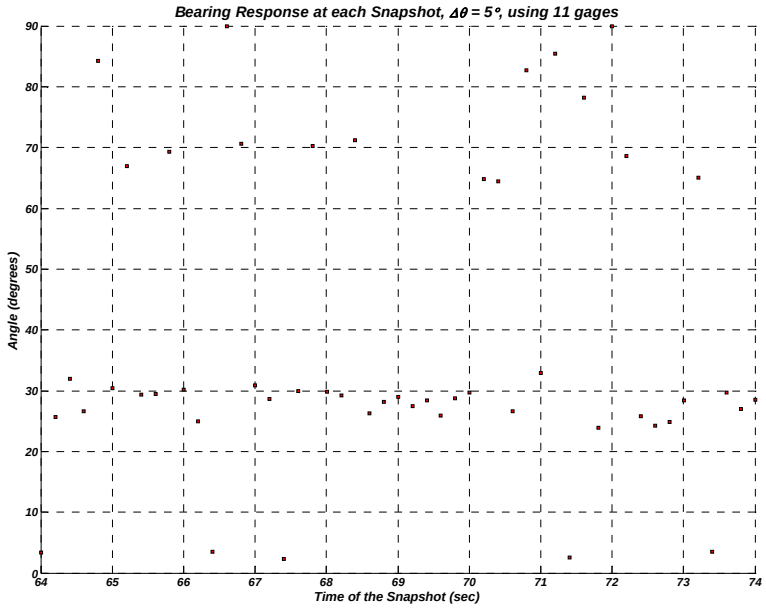

Bearing estimation from wave data: Test 1, burst mode, θ= 30 degrees

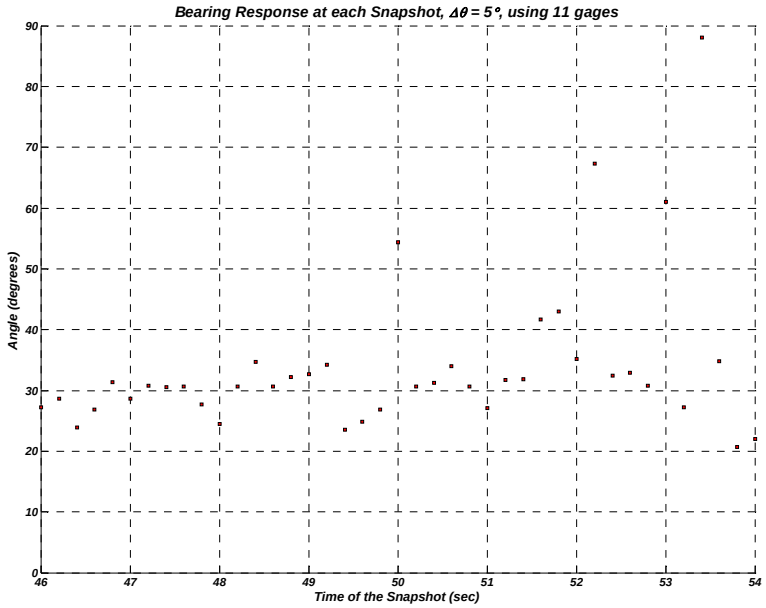

Bearing estimation from wave data: Test 2, burst mode, θ= 30 degrees

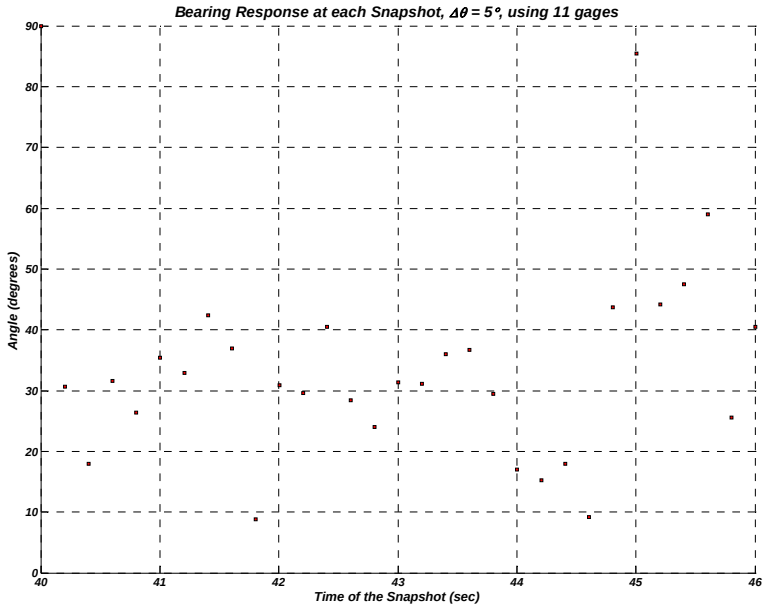

Bearing estimation from wave data: Test 3, burst mode, θ= 30 degrees

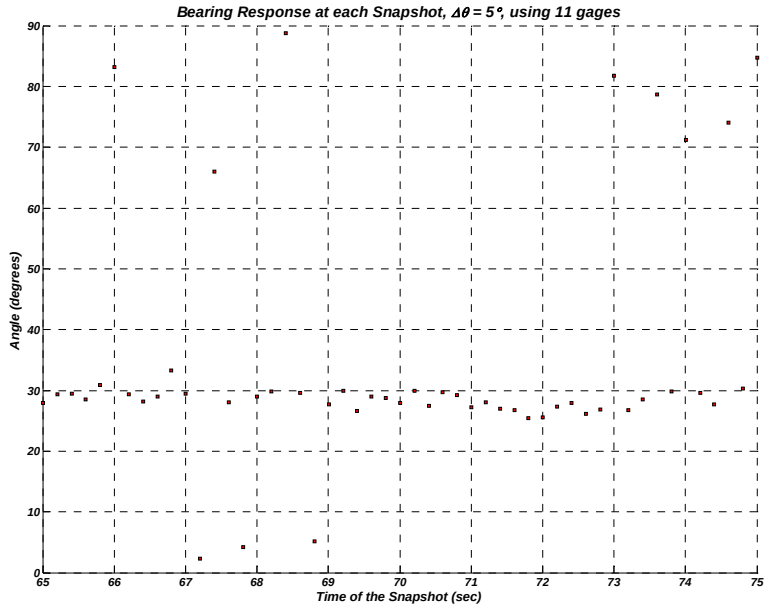

Bearing estimation from wave data: Test 4, burst mode, θ= 30 degrees

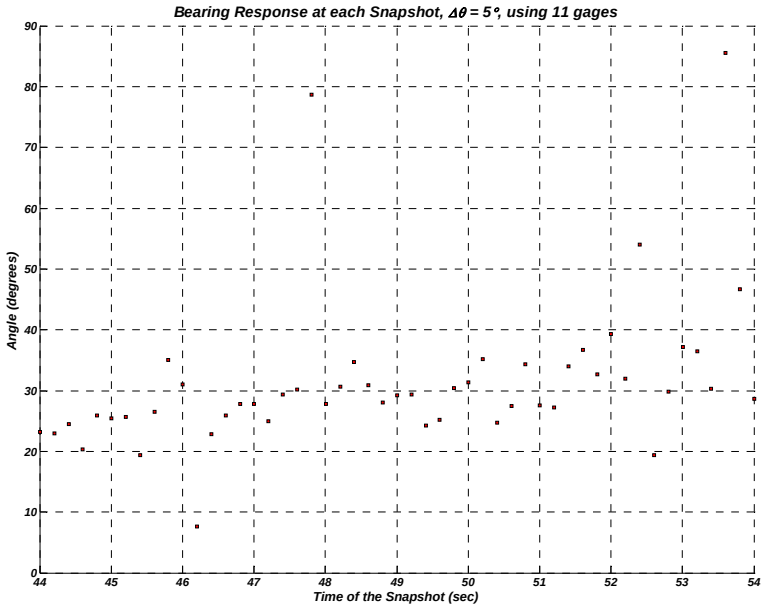

Bearing estimation from wave data: Test 5, burst mode, θ= 30 degrees

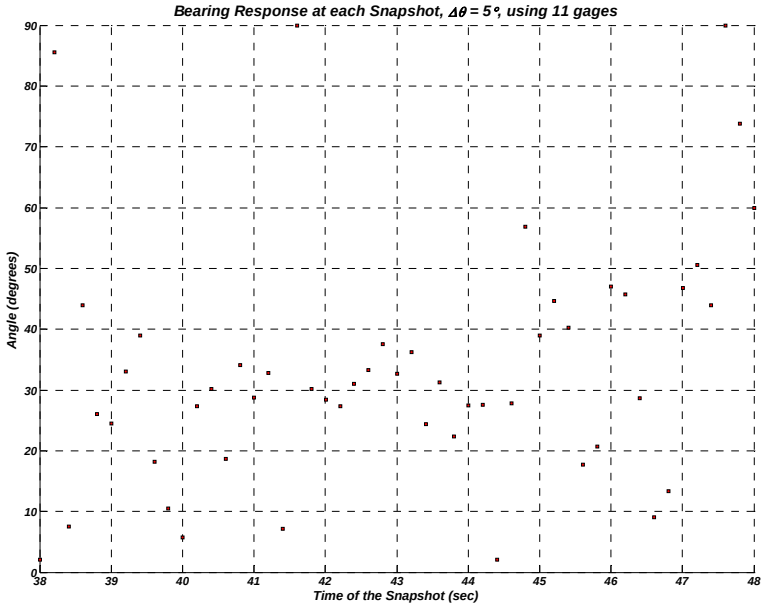

Bearing estimation from wave data: Test 6, burst mode, θ= 30 degrees

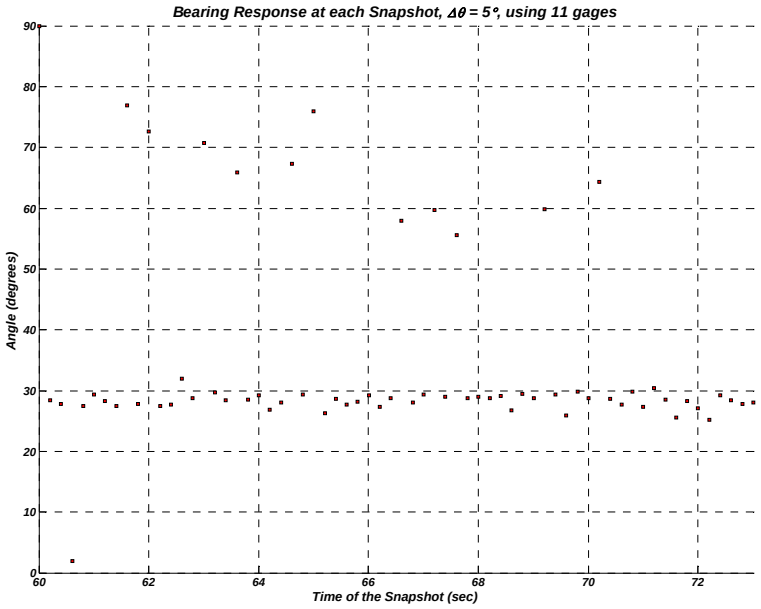

Bearing estimation from wave data: Test 7, continuous mode, θ= 30 degrees

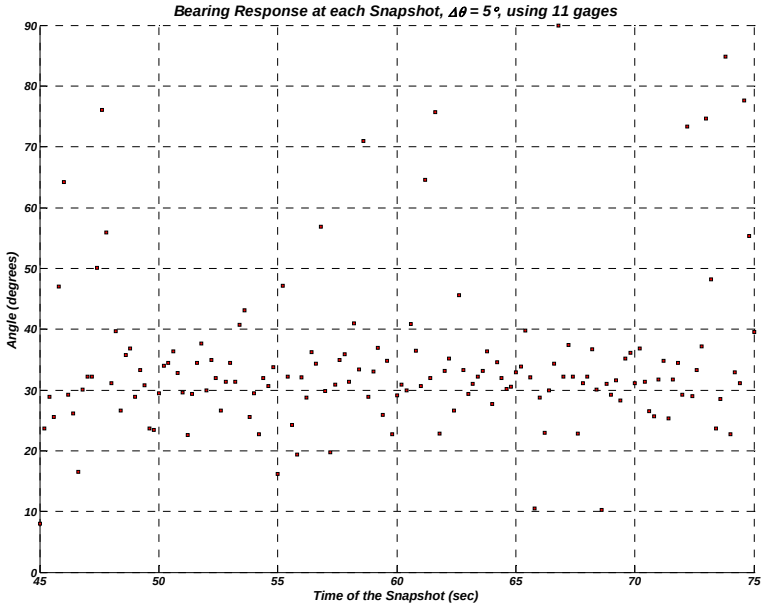

Bearing estimation from wave data: Test 8, continuous mode, θ= 30 degrees

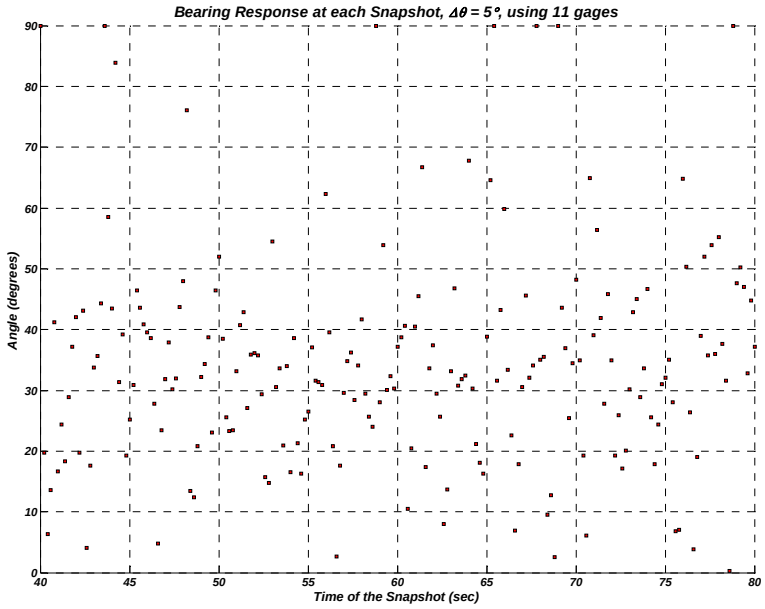

Bearing estimation from wave data: Test 9, continuous mode, θ= 30 degrees

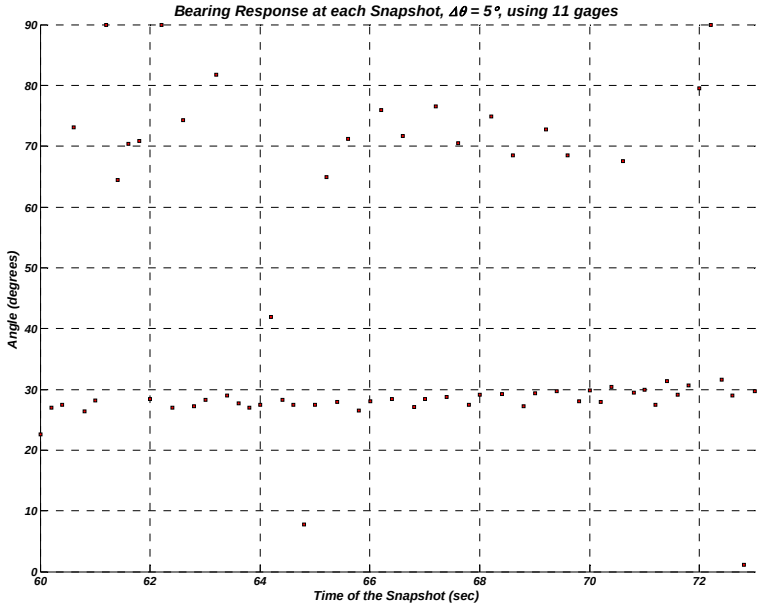

Bearing estimation from wave data: Test 10, continuous mode, θ= 30 degrees

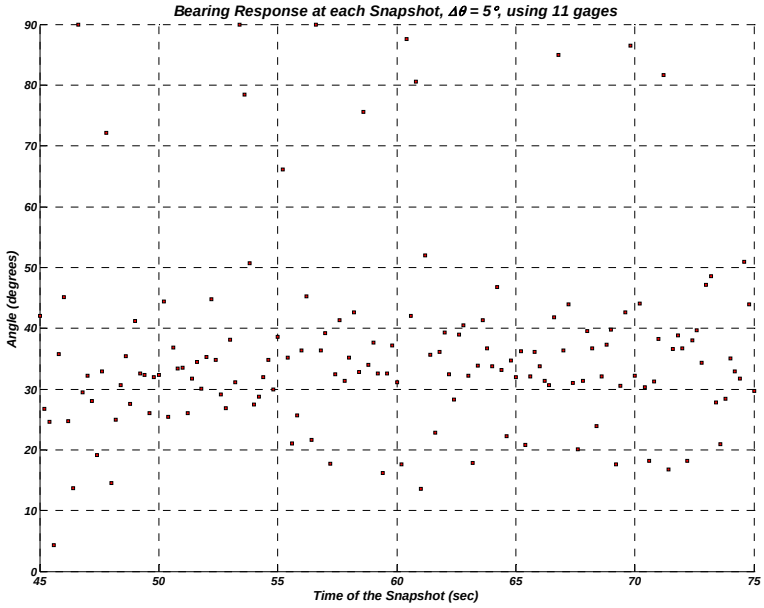

Bearing estimation from wave data: Test 11, continuous mode, θ= 30 degrees

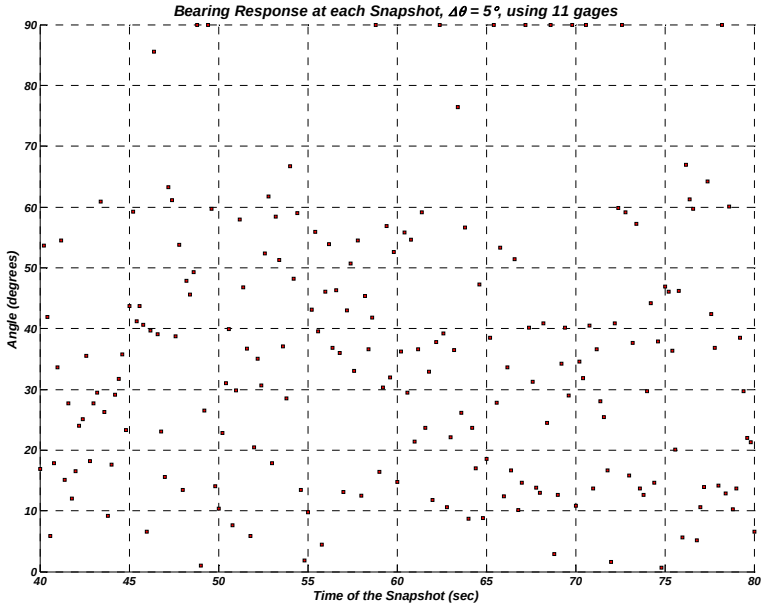

Bearing estimation from wave data: Test 12, continuous mode, θ= 30 degrees

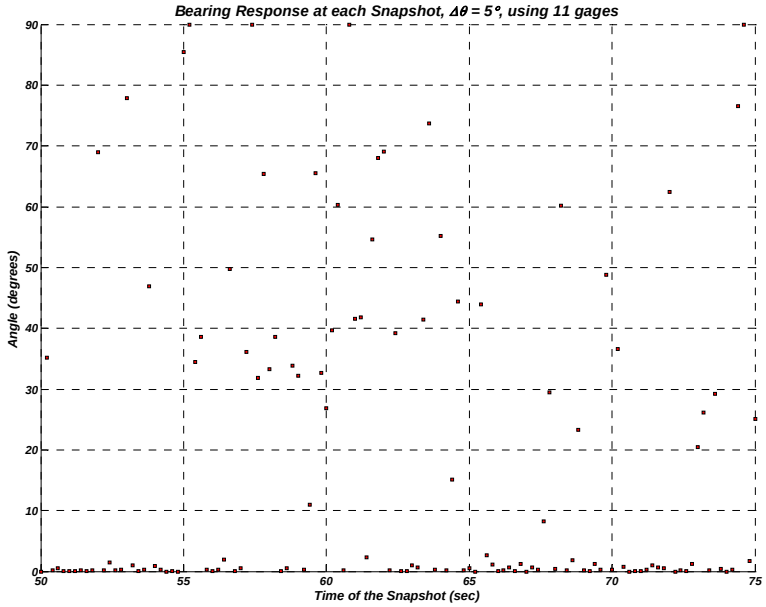

Bearing estimation from wave data: Test 1, burst mode, θ= 0 degrees

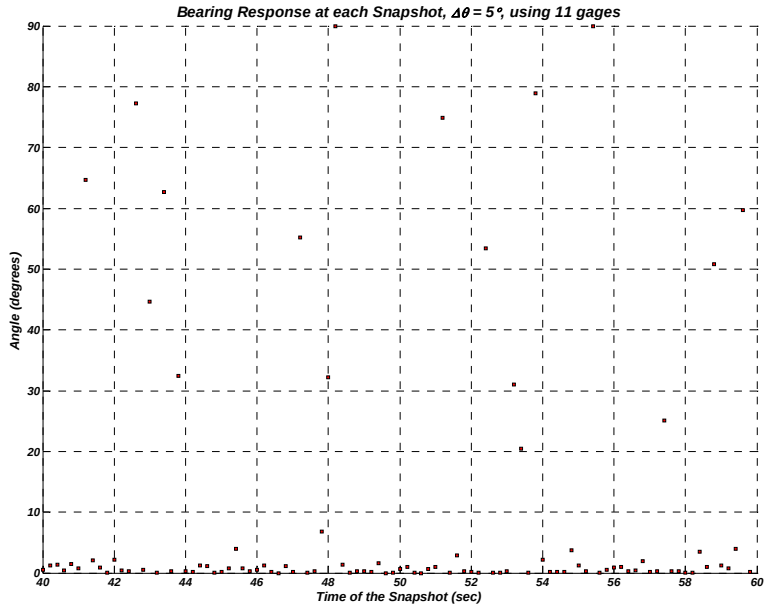

Bearing estimation from wave data: Test2, burst mode, θ= 0 degrees

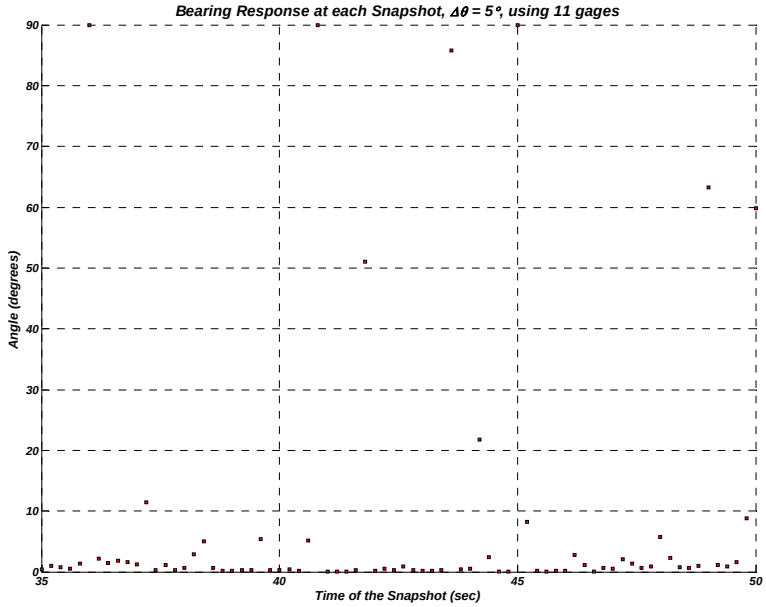

Bearing estimation from wave data: Test 3, burst mode, θ= 0 degrees

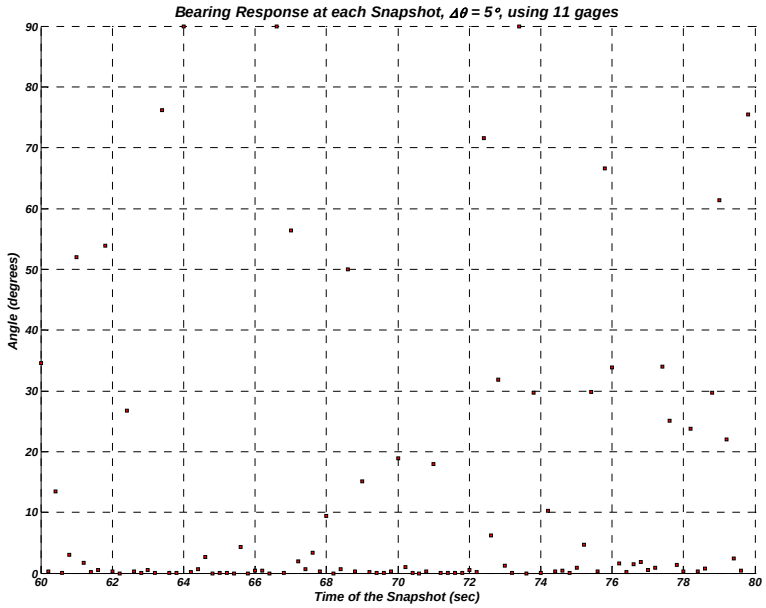

Bearing estimation from wave data: Test 4, burst mode, θ= 0 degrees

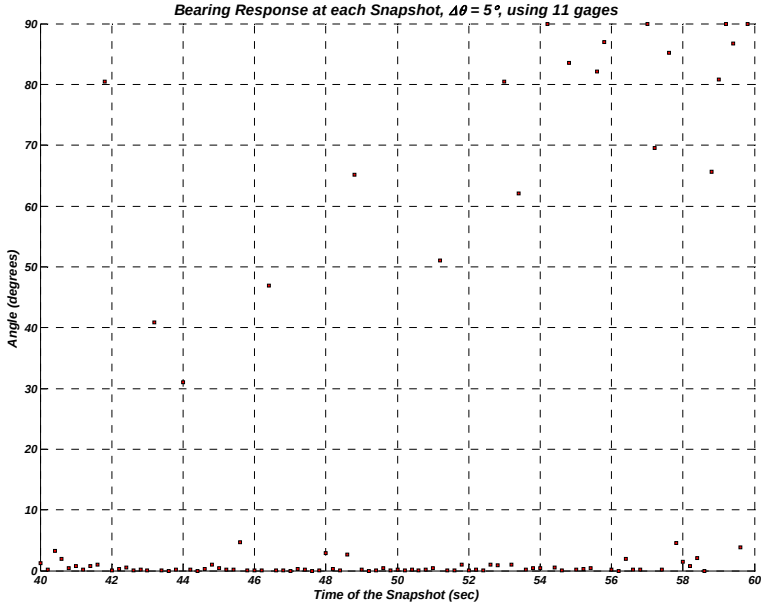

Bearing estimation from wave data: Test 5, burst mode, θ= 0 degrees

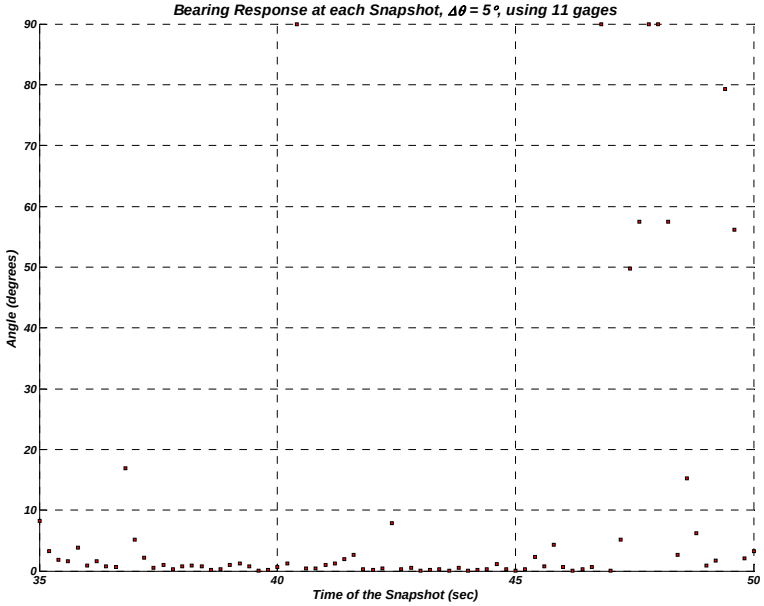

Bearing estimation from wave data: Test 6, burst mode, θ= 0 degrees

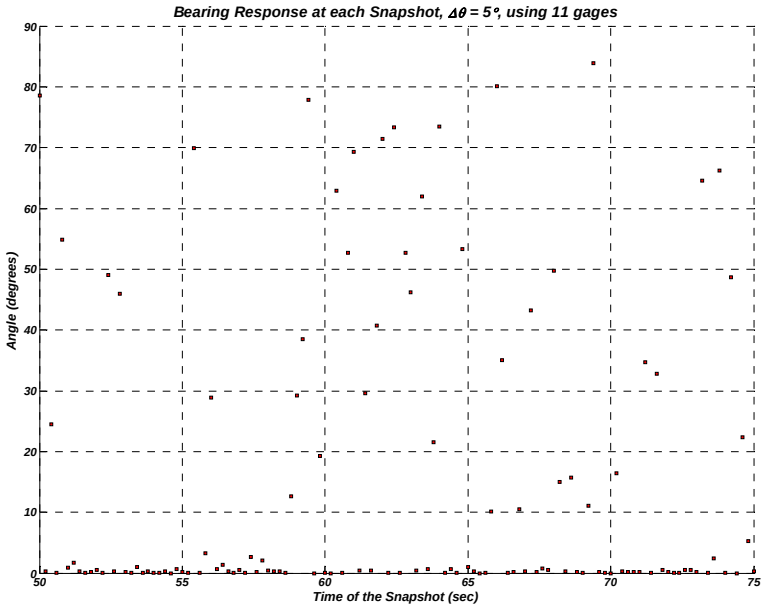

Bearing estimation from wave data: Test 7, continuous mode, θ= 0 degrees

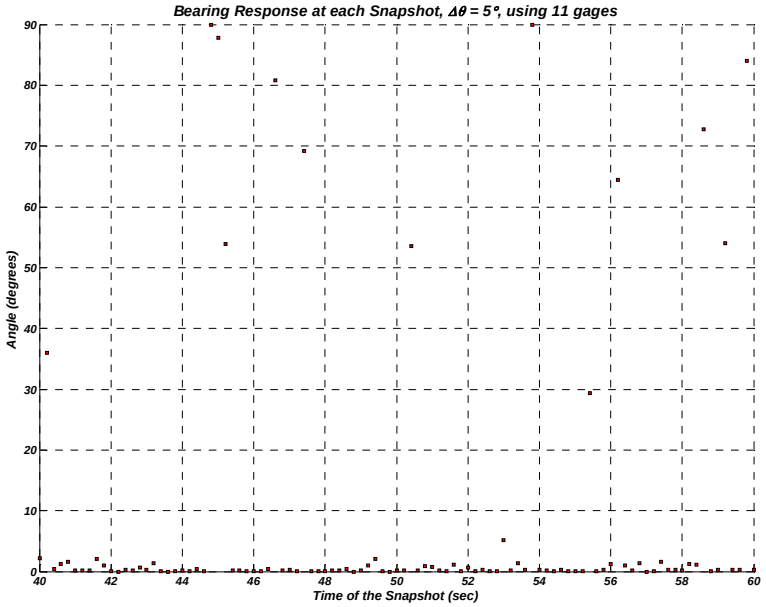

Bearing estimation from wave data: Test 8, continuous mode, θ= 0 degrees

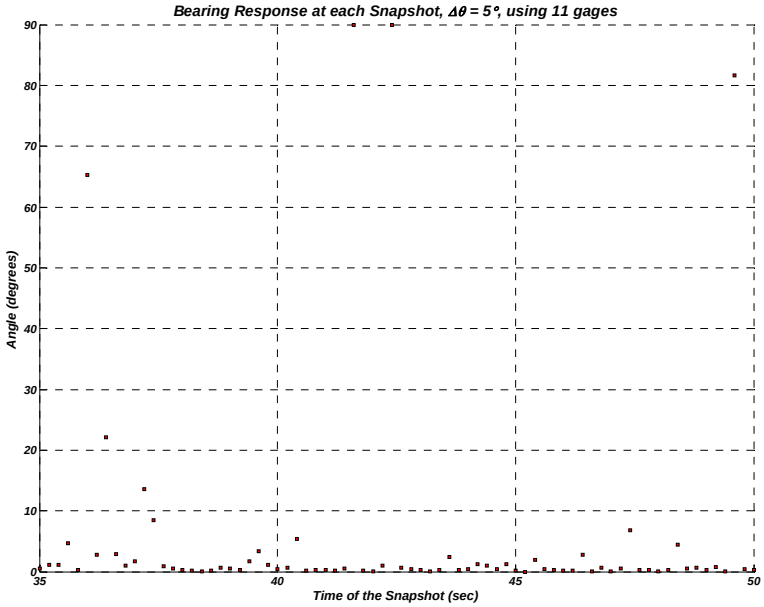

Bearing estimation from wave data: Test 9, continuous mode, θ= 0 degrees

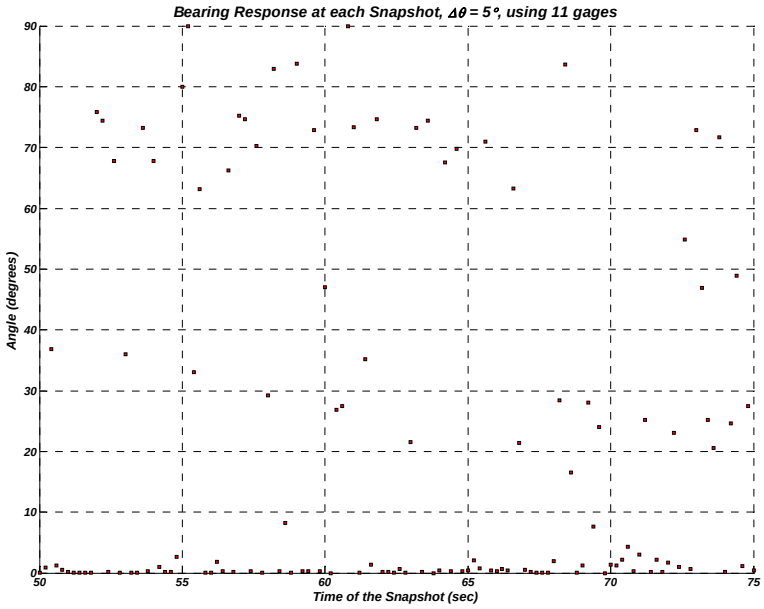

Bearing estimation from wave data: Test 10, continuous mode, θ= 0 degrees

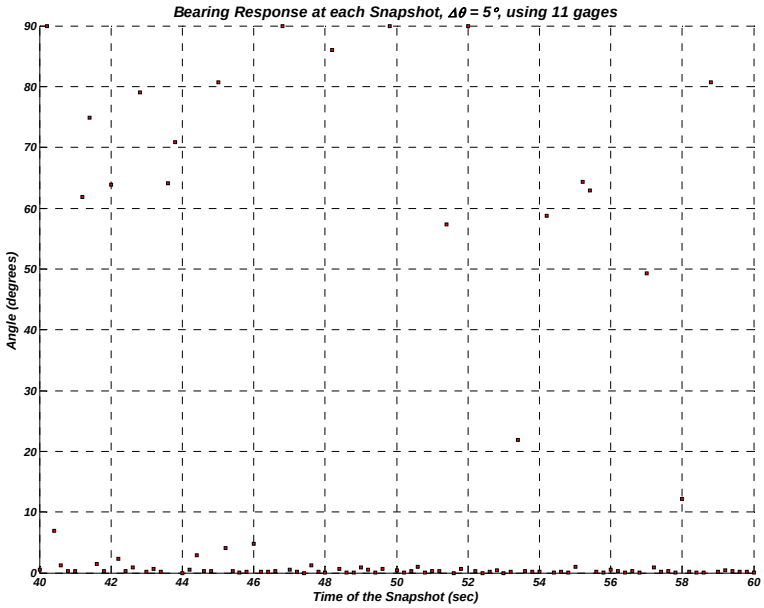

Bearing estimation from wave data: Test 11, continuous mode, θ= 0 degrees

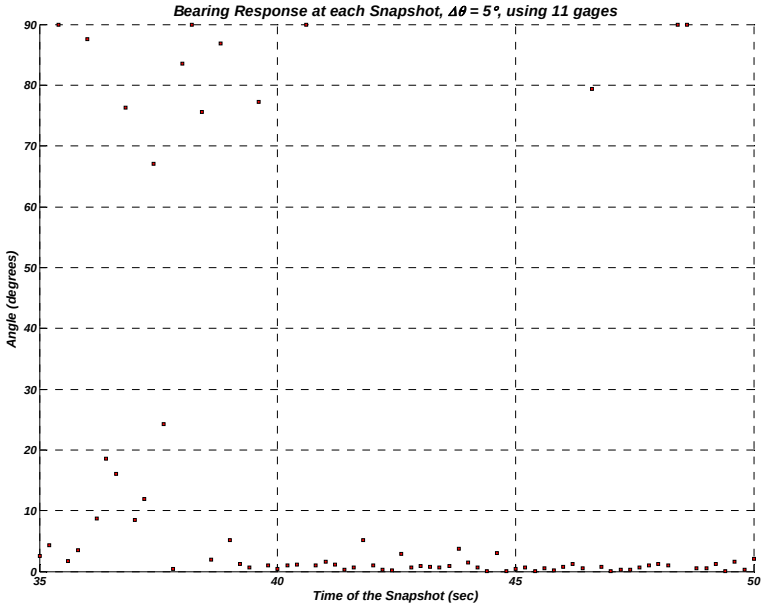

Bearing estimation from wave data: Test 12, continuous mode, θ= 0 degrees

APPENDIX E

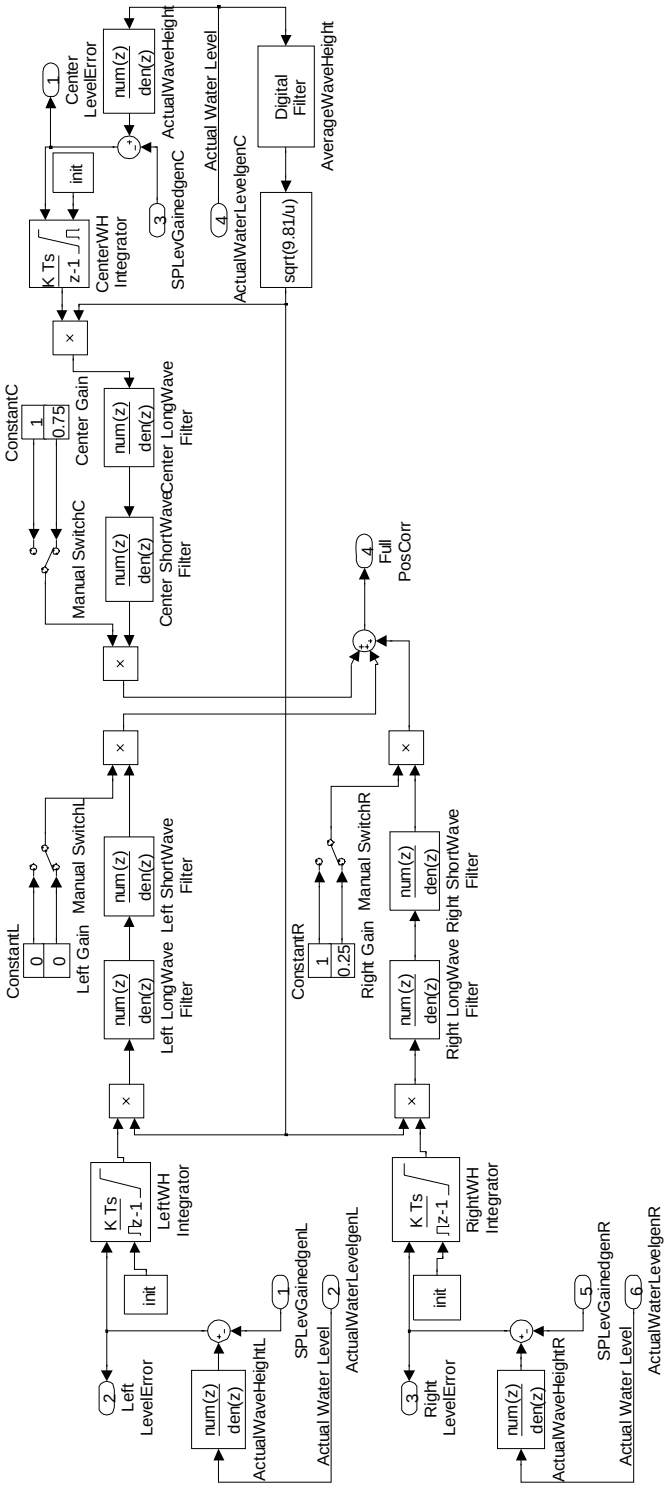

Paddle 1 (Spatial Gain-Mixer, 3D ARA loop)

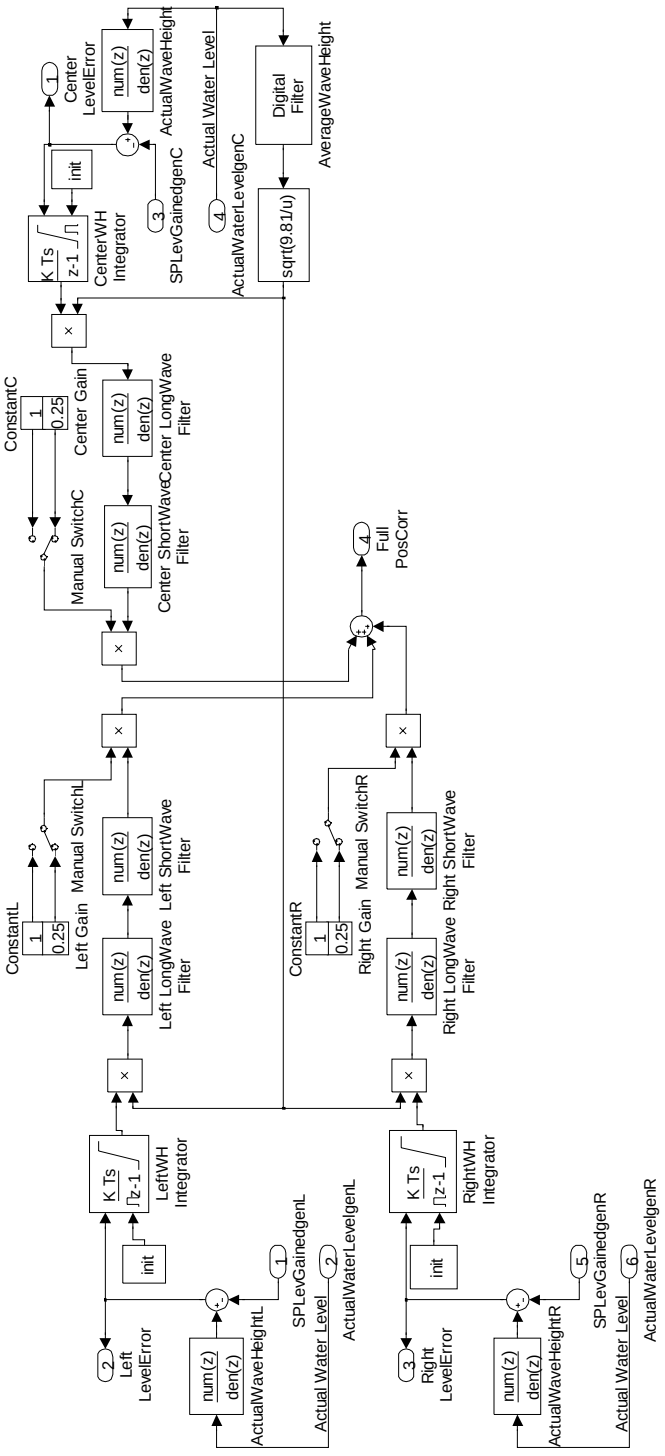

Paddle 2 (Spatial Gain-Mixer, 3D ARA loop)

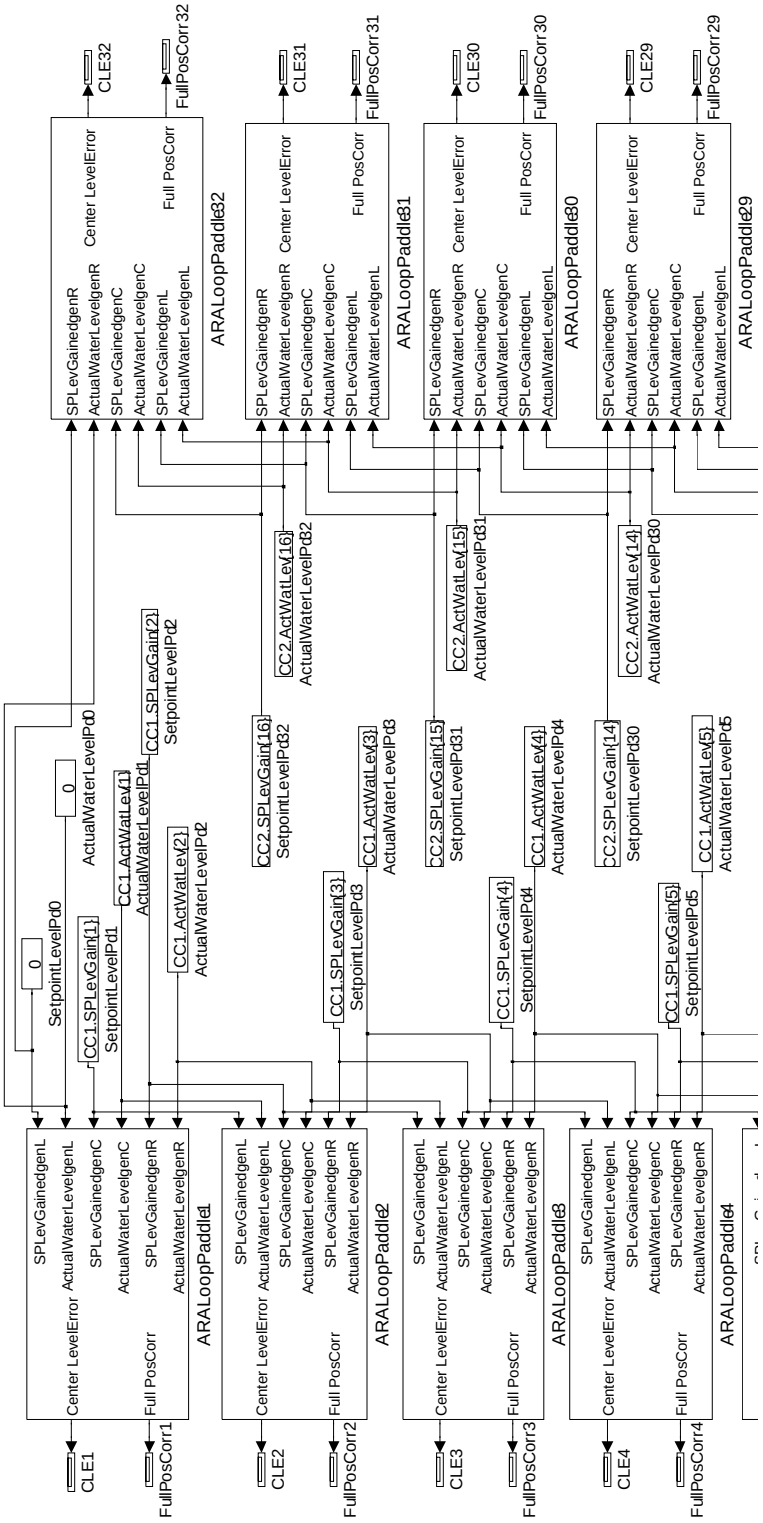

Spatial Gain-Mixer, 3D ARA loop

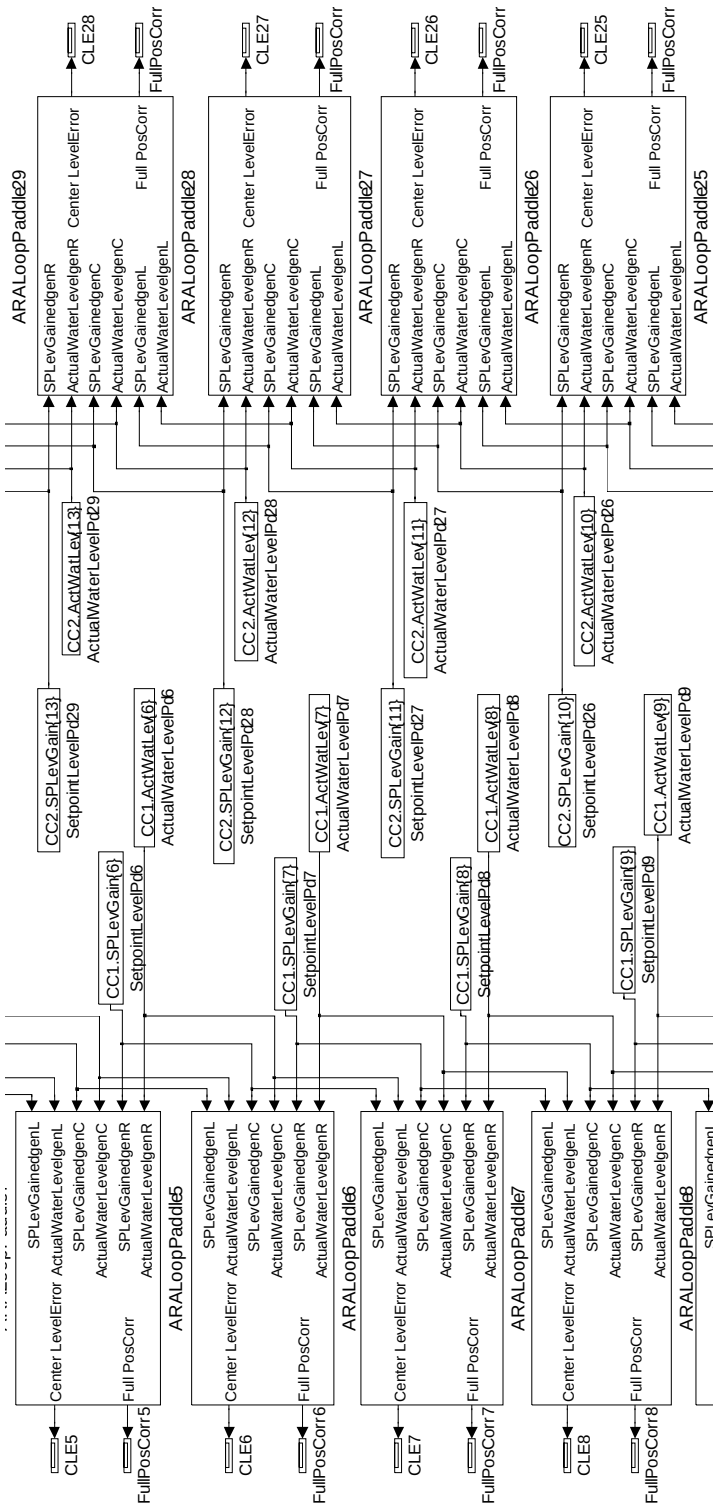

Spatial Gain-Mixer, 3D ARA loop

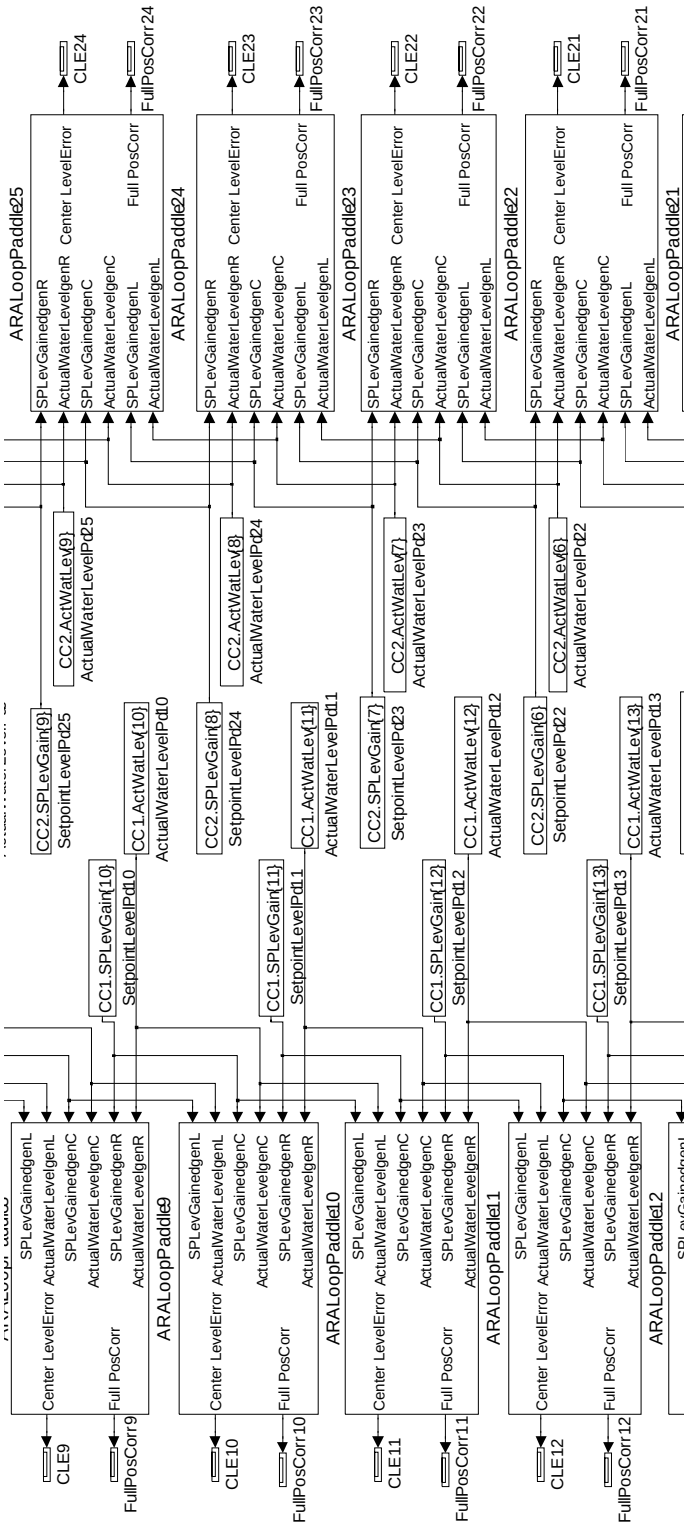

Spatial Gain-Mixer, 3D ARA loop

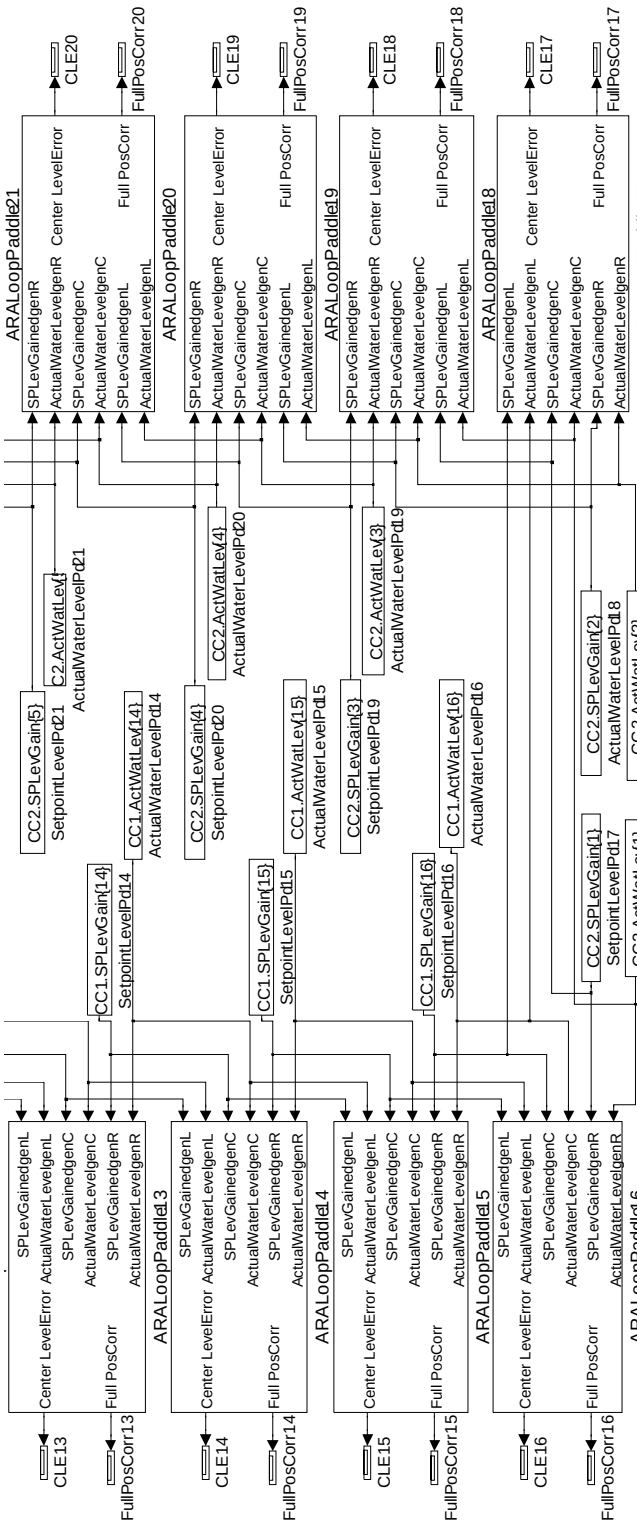

Spatial Gain-Mixer, 3D ARA loop

VITA

Name:	Oscar Cruz Castro
Address:	2RT FFCC Mex-Ver, Edif: A-15, Depto: 509, Col. Tenayuca, Tlalnepantla de Baz, Estado de Mexico, Mexico
Email Address:	oscar.cruz.castro@gmail.com
Education:	B.A., Civil Engineering, Instituto Politecnico Nacional, 1998 M.S., Ocean Engineering, Texas A&M University, 2003 Ph. D., Ocean Engineering, Texas A&M University, 2009